



MATERIAL PERTURBATIONS TO ENHANCE PERFORMANCE OF THE
THIELE HALF-WIDTH LEAKY MODE ANTENNA

DISSERTATION

Jason A. Girard, Major, USAF

AFIT/DEE/ENG/08-04

**DEPARTMENT OF THE AIR FORCE
AIR UNIVERSITY**

AIR FORCE INSTITUTE OF TECHNOLOGY

Wright-Patterson Air Force Base, Ohio

APPROVED FOR PUBLIC RELEASE; DISTRIBUTION UNLIMITED

The views expressed in this thesis are those of the author and do not reflect the official policy or position of the United States Air Force, Department of Defense, or the U.S. Government.

AFIT/DEE/ENG/08-04

MATERIAL PERTURBATIONS TO ENHANCE PERFORMANCE OF THE THIELE
HALF-WIDTH LEAKY MODE ANTENNA

DISSERTATION

Presented to the Faculty

Graduate School of Engineering and Management

Air Force Institute of Technology

Air University

Air Education and Training Command

in Partial Fulfillment of the Requirements for the

Degree of Doctorate of Philosophy

Jason A. Girard, BS, MS

Major, USAF

June 2008

APPROVED FOR PUBLIC RELEASE; DISTRIBUTION UNLIMITED

AFIT/DEE/ENG/08-04

MATERIAL PERTURBATIONS TO ENHANCE PERFORMANCE OF THE THIELE
HALF-WIDTH LEAKY MODE ANTENNA

Jason A. Girard, BS, MS
Major, USAF

Approved:

____// signed ____	_____
Dr. Michael J. Havrilla (Chairman)	Date

____// signed ____	_____
Dr. Richard Deckro (Dean's Representative)	Date

____// signed ____	_____
Dr. Peter Collins (Member)	Date

____// signed ____	_____
Dr. William Baker (Member)	Date

____// signed ____	_____
Dr. Gary A. Thiele (Member)	Date

Accepted:

____// signed ____	_____
M. U. THOMAS	Date
Dean, Graduate School of	
Engineering and Management	

Abstract

Microstrip traveling-wave antennas, often referred to as leaky-wave antennas, have been shown to radiate when the dominant or fundamental mode is suppressed and the first higher-order mode is excited. One such microstrip variation is the Thiele Half-Width (THW) antenna, which operates from 5.9 - 8.2 GHz for this research. Increasing the bandwidth over which the THW antenna radiates is desired, as is a fundamental understanding of the propagation characteristics over this region. This dissertation seeks to vary or perturb the material and physical properties of the THW antenna, including strip-width variations and modifications of the substrate layer, to achieve these results.

Three methods will be used to examine the effects of varying the material and physical properties of the THW antenna and extract the radiation and propagation characteristics. For all three methods, the resultant percentage bandwidth improvement and/or degradation will be computed. The first method to be used is the transverse resonance method which models the cross section of the microstrip structure as a transmission line system to accurately predict the transverse propagation behavior for a microstrip antenna. It will be shown how the analysis can be used to extract the desired bandwidth of the radiation regime.

The second method to be used is the Finite Difference Time Domain (FDTD) method. The propagation characteristics for each antenna configuration can be extracted from the longitudinal field profile under the antenna and compared to the baseline THW antenna.

The last method involves performing a frequency domain full-wave analysis to derive the bandwidth information. Here, the strip and material perturbation are modeled as equivalent surface and volume currents radiating in a grounded-slab background environment. Using vector potentials and the grounded-slab Green's function, a coupled integral equation formulation is developed and subsequently solved via the Method of Moments (MoM). Examination of the natural-mode solution of the MoM matrix leads to the propagation constant information. It is from the propagation constant information that the modes of the antenna, the necessary length of the antenna, and the bandwidth of the antenna can be determined.

Using the propagation constants derived from these methods, a complex plane analysis will be performed to show the migration of pole and branch point singularities from one quadrant in the complex plane to another. By performing this analysis, insight can be gained into what factors drive the propagation and radiation properties of the structure.

The main contributions found within this work come in the ability to easily and quickly modify a microstrip structure's materials for design purposes, efficiently determine the propagation constants that define its operating regimes, and gain physical insight into how these materials influence the radiation and propagation characteristics of the structure.

Another important contribution from this research is gaining an overall better understanding of the different operating regimes of the microstrip antenna.

Lastly, a FDTD code was developed to analyze the modified THW antenna. The Transverse Resonance Code was also modified in order to analyze this same antenna, but it will be shown later in this document that this code does not properly predict the propagation characteristics of the modified structure.

Acknowledgments

I would like to express my sincere appreciation to my faculty advisor, Dr. Michael Havrilla, for his guidance and support throughout the course of this thesis effort. The insight and experience was certainly appreciated. I would, also, like to thank my sponsor, Dr. Gary Thiele, from the Air Force Research Laboratory for both the support and latitude provided to me in this endeavor. Lastly, I would like to thank my wife and my daughters for their love and support during this very rigorous process.

Jason A. Girard

Table of Contents

	Page
Abstract	iv
Acknowledgements	vii
Table of Contents	viii
List of Figures.	x
List of Tables	xiii
 I. Material Perturbations to Enhance the Performance of the THW Antenna	 1
Introduction	1
Problem Statement	2
Potential Impact	3
The Leaky Wave Antenna	3
Propagation Constants	4
Microstrip Antenna	8
Antenna Length	9
Modes of Operation	10
Literature Search of Proposed Methods for Increasing BW	14
Proposed Method for Increasing Bandwidth	17
 II. Transverse Resonance and Finite Difference Time Domain	 20
Introduction	20
Transverse Resonance	20
Transverse Resonance Method	20
Transverse Resonance Code	22
Variations of Microstrip Structure Using TRC	24
TRC Conclusions	27
Finite Difference Time Domain	31
Background	31
FDTD Set-Up	32
Extraction of Propagation Constants from FDTD	35
FDTD Methodology and Results	41
 III. Green's Function Formulation for Full-Wave Analysis	 53
Introduction	53
Full-Wave Solution	53
Spectral Coefficients	55

	Green's Function	67
IV.	Electric Field Integral Equation Formulation and MoM Solution	71
	Introduction	71
	Electric Field Integral Equation Formulation	73
	Eigenmode Current	78
	Insertion of Green's Functions into EFIEs	80
	Method of Moments	84
	MoM Implementation	86
	Interpretation of MoM Matrix Elements	92
	Basis Functions	94
	Integration Path	100
	Newton Root Search	106
V.	Results	108
	Introduction	108
	MoM Solutions for the Baseline Microstrip Antenna	108
	MoM Solutions for the Modified Microstrip Antenna	112
	Physical Insight from Radiation Regime Results	118
	Complex Plane Analysis of Poles and Branch Points	120
	Constraint Equation Analysis	125
	Conclusions from Complex Plane Analysis	128
VI.	Conclusions	146
	Introduction	146
	Overview of Research Effort	146
	Recommendations for Future Research	150
	Conclusions	151
	Appendix A. Transverse Resonance Method	153
	Appendix B. Microstrip Antenna Characteristics Using TRC	159
	Appendix C. MoM Matrix Element Extraction from EFIEs	165
	Appendix D. Matlab Code Implementation	168
	Bibliography	171

List of Figures

Figure	Page
1. Menzel's leaky-wave antenna design	10
2. Thiele Half-Width antenna design	10
3. Electric field distribution of dominant mode, EH_0	11
4. Electric field distribution of first higher-order mode, EH_1	11
5. Microstrip propagation regimes	13
6. Two methods used to modify the original step discontinuities	16
7. Leaky-wave microstrip antenna loaded by capacitors	17
8. Microstrip with varied ϵ_3 and μ_3 under top conductor	18
9. Representative transverse t-line system for the baseline THW antenna	21
10. TRC approximation of leaky-wave prop const for baseline THW antenna	23
11. Representative transverse t-line system for the modified THW antenna	24
12. Propagation constants for rad regime using TRC for $\epsilon_1=1.33$ and $\epsilon_3=2.33$	28
13. Propagation constants for rad regime using TRC for $\epsilon_1=1.03$ and $\epsilon_3=2.33$	29
14. Propagation constants for rad regime using TRC for $\epsilon_1=3.33$ and $\epsilon_3=2.33$	30
15. Modified THW antenna with PML layers and source location	33
16. Modified THW antenna with PML layers and source location	34
17. Modified THW antenna with increased slab with PML and source location	34
18. Modified TFW antenna with PML layers and source location	34
19. FDTD y-directed electric field data for THW antenna taken longitudinally	37
20. Natural log of FDTD y-directed electric field data for THW antenna	38
21. Natural log of FDTD y-directed electric field data and best-fit α and β curve	39

22. Normalized FDTD y-directed electric field data and best-fit α and β curve	40
23. TRC and FDTD propagation constants for baseline THW antenna . . .	43
24. FDTD prediction of propagation constants for modified THW antenna	44
25. FDTD prediction of propagation constants for microstrip with $\epsilon_3 = 1.33$	45
26. FDTD y-directed electric field data near cut-off for radiation regime (6 GHz)	50
27. Natural log of FDTD y-directed electric field data near cut-off (6 GHz)	51
28. Natural log of FDTD y-directed electric field data and best-fit α and β curve	52
29. Cross-section of microstrip background environment	56
30. Source (y') and observation (y) points and paths of interaction	68
31. Cross-sectional view of the modified full-width leaky microstrip antenna	73
32. The four regions of interaction between source and observer locations .	92
33. FDTD y-directed electric fields within the cross-section of THW antenna	95
34. Riemann sheets in the complex p_2 and p_2^2 planes	102
35. Typical pole and branch point locations for Bound Regime (lossy case) .	103
36. Migration path for the pole and branch points for Bound Regime	104
37. Typical pole and branch point locations for Radiation Regime (lossless case)	105
38. Propagation constants for the Baseline THW Antenna over Radiation Regime	110
39. Propagation constants for radiation regime using MoM $\epsilon_1=1.33$ and $\epsilon_3=2.33$	114
40. Propagation constants for radiation regime using MoM $\epsilon_1=1.03$ and $\epsilon_3=2.33$	115
41. Propagation constants for radiation regime using MoM $\epsilon_1=3.33$ and $\epsilon_3=2.33$	116
42. Propagation constants for radiation regime using MoM for $\epsilon_3=1.33$	117
43. ξ plane poles and branch points for baseline THW antenna over four regimes	129

44. ξ plane poles and branch points for baseline THW antenna over two regimes	130
45. ξ plane poles and branch points for baseline THW antenna using $\epsilon_3=2.33$	131
46. ξ plane poles and branch points for modified THW antenna using MoM	132
47. Close-up view of ξ plane poles and branch points for modified THW MoM	133
48. Close-up view of ξ plane poles and branch points for modified THW FDTD	134
49. ξ plane poles and branch points for modified THW antenna using TRC	135
50. ξ plane poles and branch points for modified THW antenna using MoM	136
51. Close-up view of ξ plane poles and branch points for modified THW MoM	137
52. Close-up view of ξ plane poles and branch points for modified THW FDTD	138
53. ξ plane poles and branch points for modified THW antenna using TRC	139
54. Complex p_2 -plane values over ξ integration path for baseline THW antenna	140
55. Complex ξ_p , ξ_b , ζ_z , and p_2 values for baseline THW antenna for four regimes	141
56. Complex ξ_p , ξ_b , ζ_z , and p_2 values for baseline THW antenna for four regimes	142
57. Complex ξ_p , ξ_b , ζ_z , and p_2 values for baseline THW antenna for four regimes	143
58. Complex ξ_p , ξ_b , ζ_z , and p_2 values for baseline THW antenna for four regimes	144
59. Complex ξ_p , ξ_b , ζ_z , and p_2 values for baseline THW antenna for four regimes	145
60. Representative transverse t-line system for the baseline THW antenna . . .	154
61. TRC leaky-wave propagation constants for baseline THW antenna	160
62. Multiple leaky-wave microstrip antennas	161
63. Leaky-wave antennas with varying conductor widths	162
64. Matlab Method of Moments code implementation flowchart	170

List of Tables

Table	Page
1. Test Matrix for Varied Permittivity Under Top Conductor for TRC Predictions	25
2. TRC Predicted Bandwidth for Varied Permittivity Under Top Conductor	26
3. Test Matrix for Varied Permittivity Under Top Conductor Using FDTD	44
4. FDTD Predicted Bandwidth for Varied Permittivity Under Top Conductor	46
5. Basis Functions Used To Represent Unknown Currents And Electric Fields	99
6. BW of Baseline THW Antenna Using TRC, FDTD, and Method of Moments	110
7. Test Matrix for Modified THW Antennas Using Method of Moments . . .	113
8. Radiation Regime Bandwidth of Modified THW Antennas Using Methods	117
9. Microstrip Antenna Widths and Permittivities	161

Chapter 1

MATERIAL PERTURBATIONS TO ENHANCE PERFORMANCE OF THE THIELE HALF-WIDTH LEAKY MODE ANTENNA

1.1 Introduction

Ever since Heinrich Hertz's generation and detection of the first meter-wavelength radio waves in 1888 and Guglielmo Marconi's sending radio waves across the Atlantic Ocean in 1901, the antenna has been a critical component in the ability to efficiently and predictably transfer data from one device to another. This is true whether it be low-frequency voice communication between radios or ultra high-frequency data transfer from a ground station to a satellite orbiting the Earth.

Modern aircraft rely heavily on being able to retrieve data from GPS satellites, communicate with air traffic controllers on the ground, as well as detect near-by aircraft through the use of antennas positioned on the aircraft's surface. Typically, these antennas are bulky, heavy, and costly due to their complexity. They must be able to operate in the required frequency regime, have a gain and antenna pattern that meets their required use (omni-directional, narrowbeam, broadband, etc.), and efficiently radiate and receive EM energy. In addition to all of these, with the advent of stealth aircraft, the need for these antennas to be low observable becomes increasingly more important. One such antenna that meets most of these requirements is the microstrip antenna.

1.2 Problem Statement

The ability of a microstrip structure to radiate as a leaky wave antenna has been widely investigated ever since Ermer first documented the existence of a radiation region near the cutoff of the higher-order modes back in the 1970s [1]. Since this discovery, microstrip antennas have evolved to the point where they are used for many military applications. Due to their relatively small size, ability to conform to a surface, lower radar cross section, and low cost; microstrip antennas have many benefits for being used on aircraft surfaces. However, with these benefits comes one significant deficiency: narrow bandwidth.

The traveling wave microstrip antenna has been extensively analyzed by the electromagnetic community over the past 28 years by Oliner *et al.* [27, 42, 84, 89], Menzel [3], Nyquist *et al.* [13, 14, 16-18, 20-22, 31-33, 53, 57, 60], and Jackson *et al.* [24, 26, 27, 37, 84, 89]. Its baseline performance is well known and documented. Over this time, researchers have tried numerous methods to tackle the challenge of improving its performance (bandwidth, gain, VSWR, etc.) [61-90]. Some of these methods include using an array of microstrip antennas (both in-plane and stacked), tapering the width of the top conductor longitudinally, and placing capacitors periodically along the edges of the top conductor. However, all of these ideas have been met with limited results. Why is this? What is the dominating factor that prevents the microstrip from achieving greater bandwidth? What other potential methods can be employed to improve bandwidth? This research effort looks to investigate and answer these questions.

The purpose of this chapter is to provide the background necessary to understand the problem at hand and to give insight into why certain methods were chosen to investigate this problem. A short history of leaky-wave antennas will be given, including the traveling wave theory behind their existence. Several variations to the baseline microstrip antenna will be discussed, including their advantages and disadvantages.

1.2.1 Potential Impact

Although technology advancements over the last 50 years have allowed for the development of lighter-weight materials, guidance and navigation systems that can fit onto a microchip, and smaller, more efficient engines; as the available space to place antennas or any other device on modern aircraft has become more and more limited. It has therefore become increasingly more important to look to reduce the size and weight of all of the aircraft's components. If the microstrip antenna performance can be improved, a single microstrip antenna may be able to replace two older antennas, thus freeing up space for other mission essential equipment. Additionally, fewer antennas on an aircraft can also lead to less impact on the radar cross section of that platform. Finally, improved bandwidth performance will lead to enhanced radar imaging and target detection capability.

1.3 The Leaky-Wave Antenna

A microstrip antenna does not inherently radiate as a traveling-wave antenna. The fields produced by the dominant EH_0 mode do not decouple from the structure. It is

only until the dominant mode is blocked or restricted within the antenna that it can operate in a higher-order mode. It is in these higher-order modes that the fields are able to decouple from the surface and, thus, radiate from the structure. When this happens, the antenna is said to be operating as a leaky-wave antenna.

1.3.1 Propagation Constants

Before the leaky-wave antenna can be analyzed, an understanding of the electromagnetic theory behind the propagation characteristics of the antenna is required. From the propagation characteristics, the specific modes of operation for the microstrip traveling-wave antenna can be derived and subsequently identified.

As electromagnetic waves propagate, they must satisfy Maxwell's curl equations for time-varying harmonic fields

$$\nabla \times \vec{H} = \vec{J} + j\omega\vec{D} \quad (1.1)$$

$$\nabla \times \vec{E} = -\vec{m} - j\omega\vec{B} \quad (1.2)$$

where \vec{J} is the electric current density and \vec{m} is the fictitious/equivalent magnetic current density. The first equation is commonly called *Ampère's law* and the second *Faraday's law*. For simple media (linear, homogeneous, isotropic), the magnetic and electric fields satisfy the relations

$$\vec{B} = \mu\vec{H} \quad (1.3)$$

$$\vec{D} = \epsilon\vec{E} \quad (1.4)$$

$$\vec{m} = \vec{m}^i + \vec{m}^c \quad \vec{m}^c = \sigma_m \vec{H} \quad (1.5) \quad (1.6)$$

$$\vec{J} = \vec{J}^i + \vec{J}^c \quad \vec{J}^c = \sigma \vec{E} \quad (1.7) (1.8)$$

with the i and c superscripts meaning *impressed* and *conduction*, respectively.

Substituting (1.3), (1.5), and (1.6) into (1.2) leads to

$$\nabla \times \vec{E} = -\vec{m}^i - \sigma_m \vec{H} - j\omega\mu \vec{H} \quad (1.9)$$

$$\nabla \times \vec{E} = -\vec{m}^i - j\omega(\mu + \frac{\sigma_m}{j\omega}) \vec{H} \quad (1.10)$$

$$\nabla \times \vec{E} = -\vec{m}^i - j\omega\mu_c \vec{H} \quad (1.11)$$

where μ_c is the effective complex permeability. Similarly, substitution of (1.4), (1.7), and (1.8) into (1.1) gives

$$\nabla \times \vec{H} = \vec{J}^i + \sigma \vec{E} + j\omega\varepsilon \vec{E} \quad (1.12)$$

$$\nabla \times \vec{H} = \vec{J}^i + j\omega(\varepsilon + \frac{\sigma}{j\omega}) \vec{E} \quad (1.13)$$

$$\nabla \times \vec{H} = \vec{J}^i + j\omega\varepsilon_c \vec{E} \quad (1.14)$$

where ε_c is the effective complex permittivity. Taking the divergence of equation (1.11) produces

$$\nabla \cdot (\nabla \times \vec{E} = -\vec{m}^i - j\omega\mu_c \vec{H}) \quad (1.15)$$

$$0 = -\nabla \cdot \vec{m}^i - j\omega\mu_c \nabla \cdot \vec{H} \quad (1.16)$$

The divergence of the curl (on the left hand side) is mathematically zero. Using the continuity relation

$$\nabla \cdot \vec{m}^i = -j\omega q_{mv}^i \quad (1.17)$$

in (1.16) leads to the following divergence relation for the magnetic field \vec{H} , namely

$$\nabla \cdot \vec{H} = \frac{q_{mv}^i}{\mu_c} \quad (1.18)$$

Similarly, taking the divergence of (1.14) and using the second continuity relation

$$\nabla \cdot \vec{J}^i = -j\omega q_{ev}^i \quad (1.19)$$

produces the following divergence relation for the electric field \vec{E} , that is

$$\nabla \cdot \vec{E} = \frac{q_{ev}^i}{\epsilon_c} \quad (1.20)$$

Next, taking the curl of equation (1.11) gives

$$\nabla \times \nabla \times \vec{E} = -\nabla \times \vec{m}^i - j\omega\mu_c \nabla \times \vec{H} \quad (1.21)$$

and substitution into equation (1.14) with the aid of the vector identity

$$\nabla \times \nabla \times \vec{E} = \nabla(\nabla \cdot \vec{E}) - \nabla^2 \vec{E} \quad (1.22)$$

leads to

$$\nabla(\nabla \cdot \vec{E}) - \nabla^2 \vec{E} = -\nabla \times \vec{m}^i - j\omega\mu_c(\vec{J}^i + j\omega\epsilon_c \vec{E}) \quad (1.23)$$

Using equation (1.20) and defining $k^2 = \omega^2 \mu_c \epsilon_c$ gives

$$\nabla\left(\frac{q_{ev}^i}{\epsilon_c}\right) - \nabla^2 \vec{E} = -\nabla \times \vec{m}^i - j\omega\mu_c \vec{J}^i + k^2 \vec{E} \quad (1.24)$$

Rearranging and using equation (1.19) produces the wave equation for \vec{E}

$$\nabla^2 \vec{E} + k^2 \vec{E} = j\omega\mu_c \vec{J}^i - \frac{\nabla(\nabla \cdot \vec{J}^i)}{j\omega\epsilon_c} + \nabla \times \vec{m}^i \quad (1.25)$$

Similarly, the wave equation for the magnetic field, \vec{H} , can be derived as

$$\nabla^2 \vec{H} + k^2 \vec{H} = j\omega\epsilon_c \vec{m}^i - \frac{\nabla(\nabla \cdot \vec{m}^i)}{j\omega\mu_c} - \nabla \times \vec{J}^i \quad (1.26)$$

For both wave equations, the source terms on the right-hand-side are very involved and complicated. Because of this, one method to solve for the fields is to use the Hertzian potential method, which will be described later in this dissertation.

The natural response of a system is examined by setting the impressed currents in (1.25) and (1.26) equal to zero. It will be shown later in this dissertation how the natural response solution leads to the desired propagation constants of leaky wave microstrip antennas.

If there are no impressed currents, this results in

$$\vec{J}^i, \vec{m}^i = 0 \Rightarrow \nabla^2 \vec{E} + k^2 \vec{E} = 0 \quad (1.27)$$

with similar results for the magnetic field \vec{H} .

In order to gain a better understanding of what is happening to the fields as they propagate throughout an antenna and the space surrounding it, it is suitable to use separation of variables to write the *wavenumber*, k , in terms of the three separate constants, k_x , k_y , and k_z . Doing so will show the influence in the x -, y -, and z - directions on the overall wavenumber as it is applied to (1.25) and (1.26). The wavenumber can then be found using the well-known *constraint equation*

$$k = \sqrt{k_x^2 + k_y^2 + k_z^2} \quad (1.28)$$

where, in general, each constant takes the form of a *complex propagation factor*

$$k_\eta = \beta_\eta - j\alpha_\eta \quad \eta = x, y, z \quad (1.29)$$

with β being the *phase constant*, and α being the *attenuation constant* along the η direction. How these wave numbers interrelate in order to define and physically

understand the four regions of operation of the microstrip traveling-wave antenna will be described later in this dissertation.

1.3.2 Microstrip Antenna

Typically, a narrowband antenna will have currents that propagate down the length of the antenna, hit the end of the structure, and reflect back in the opposite direction. These currents then constructively and destructively add to produce standing waves along the length of the antenna. The currents at the ends of the antenna are driven to zero, thus limiting how many wavelengths of a certain frequency can fit along the length of the antenna. This limiting factor drives these standing wave antennas to be narrow in bandwidth. If the antenna could be infinite in length (in theory), designed to shed energy before reaching the end, or "matched" at the ends so as to eliminate any current from being reflected and standing waves from forming along their length, this would increase the bandwidth of the antenna. This type of radiating structure is referred to as a traveling wave antenna.

The microstrip antenna is a simple, cost-effective structure for radiating energy as a traveling wave [2]. However, three main problems exist: (1) the antenna must be finite in length for practical applications; (2) the antenna will only radiate energy when it is operating in the first higher-order mode, called the EH_1 mode, or higher and not in the dominant mode; and (3) though the bandwidth is greater than that for a standing wave antenna, the bandwidth for the microstrip antenna is still very limited [2]. The following subsections address these limitations and how they can be mitigated.

1.3.3 Antenna Length

For obvious reasons, an antenna that must be extremely long in length in order to avoid standing waves from forming is neither realistic nor practical. Given this, the antenna will be finite in length and, thus, some current will be reflected when it hits the physical end of the antenna. As stated before, any current that is reflected back down the length of the antenna will constructively and destructively combine with the forward traveling current to cause a standing wave. If this is the case, how can the microstrip antenna operate as a traveling wave antenna? The answer lies in the attenuation constant, α_z , which is a measure of how much energy escapes at a certain frequency as the wave propagates along the guiding axis (i.e., the z -axis). As the energy propagates down the length (l) of the antenna, it is attenuated at a rate of $e^{-\alpha_z l}$ due to energy leaking from the structure. As this energy is being "shed-off", less and less is being propagated down the length, to the point where very little energy actually reaches the end of the antenna. If greater than 90% of the energy has been attenuated before it reaches the end of the antenna, the microstrip will support a traveling wave [5]. For the baseline THW antenna used in this research, the length required is 20cm.

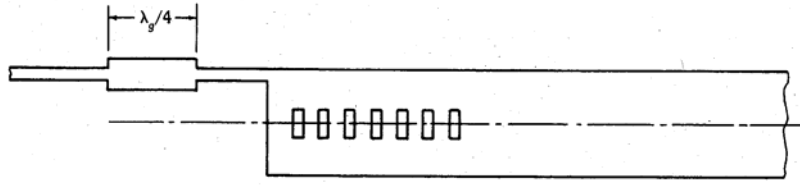


Figure 1: Menzel's leaky-wave antenna design [4]

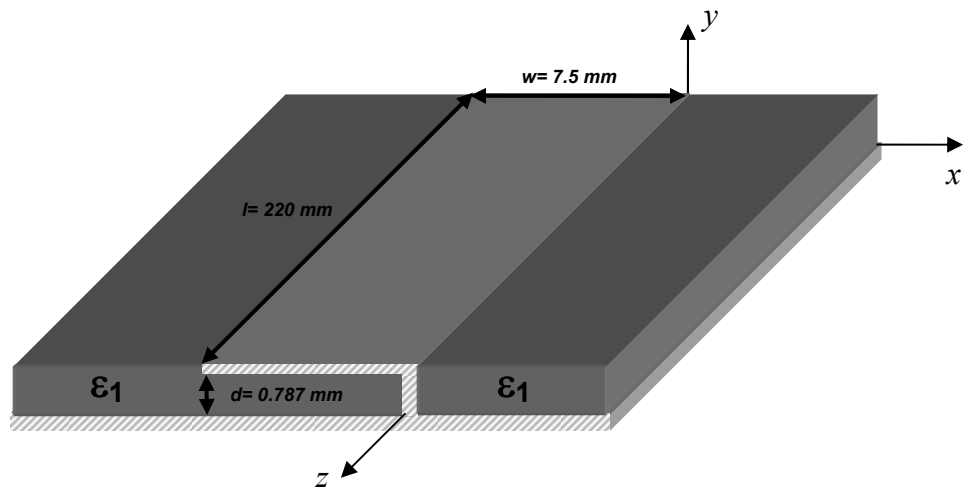


Figure 2: Thiele Half-Width antenna design

1.3.4 Modes of Operation

The idea of using a microstrip antenna to radiate EM energy has not been around as long as one might think. It was not until the 1970s that Ermentrout documented the existence of a radiation region near the cutoff of the higher-order modes. Later in the same decade, Menzel presented a paper that looked into this phenomenon further by purposely suppressing the dominant mode in his antenna design by cutting seven transverse slots in the top conductor (see Figure 1) [3]. Recently, Dr Gary Thiele of Analytic Designs, Inc. proposed a new microstrip antenna that effectively blocked the

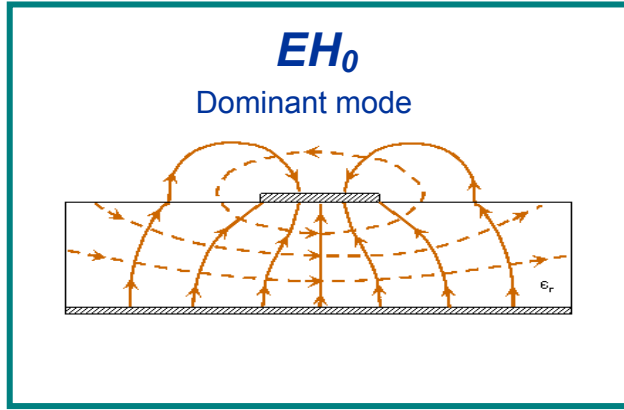


Figure 3: Electric field distribution of dominant mode, EH_0 [4]

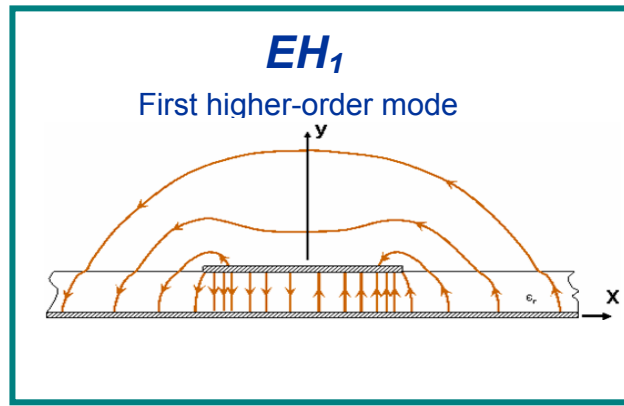


Figure 4: Electric field distribution of first higher-order mode, EH_1 [4]

dominant mode. Instead of using transverse slots, the Thiele Half-Width Antenna (THW) uses a longitudinal wall down the center of the top conductor (see Figure 2). By blocking the dominant mode, both antennas are forced to operate in the first higher-order leaky mode. Choosing frequencies properly, these antennas will radiate as traveling wave antennas. If the frequencies are too low, all fields will evanesce at the input of the antenna. If they are too high, the fields will be bound to the structure and not radiate. By

looking at the relationship of the phase constant, β_z , to the attenuation constant, α_z , over these frequencies, the operating regions of the antenna can be defined.

The dominant mode of the microstrip, EH_0 , will not radiate due to the nature of the fields that it supports. Since the electric field lines up in the same direction under the top conductor (see Figure 3), these fields will not be allowed to de-couple from the structure and, thus, do not radiate.

The higher-order modes of the microstrip (specifically, the odd numbered higher-order modes) will not be bound to the structure as with the dominant mode and will actually decouple due to the phase reversal at the longitudinal center of the top conductor (see Figure 4).

Higher-order modes will propagate in three identifiable regions or regimes: radiation, surface, and bound regimes. Below the cutoff frequency of the radiation regime, the attenuation constant, α_z , will dominate, thus the microstrip will appear to be a reactive load at the end of the input line. This non-propagating region is called the *reactive* regime.

As stated earlier, the constraint equation (1.28) dictates the propagation behavior along the x -, y -, and z -directions, respectively with each complex wave number being defined as (1.29).

Focusing on the direction of propagation (the z -direction), a plot of the phase constant, β_z , and the attenuation constant, α_z , versus frequency will reveal the three propagation regimes: radiation, surface, and bound.

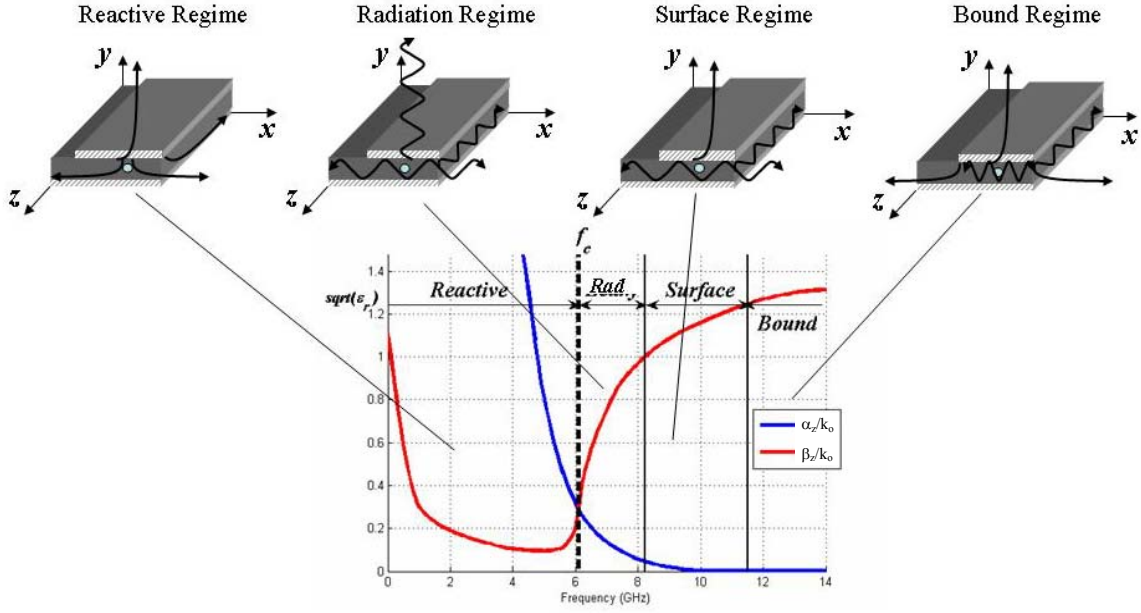


Figure 5: Microstrip propagation regimes [5]

Figure 5 shows the plot of normalized (with respect to k_0) β_z and α_z versus frequency. As stated before, from 0 GHz up to the cutoff frequency, f_c , this region is called the *reactive* regime. It is characterized by a very large α_z component, causing the microstrip to appear as a reactive load at the input of the microstrip. At the cutoff frequency, the phase and attenuation constants are equal ($\beta_z = \alpha_z$). This is the start of the *radiation* regime. In this regime, propagation is occurring in all directions.

The radiation regime continues until the phase constant grows larger than k_0 . At this point, there is no attenuation in the direction of propagation ($\alpha_z = 0$) and large attenuation in the radiated direction (α_y). Because of this, fields will no longer radiate. However, they will continue to propagate in the longitudinal and transverse directions. This is called the *surface* regime. This regime continues until $\beta_z > k$. At this point, there

is a large attenuation in the transverse direction (α_x) causing all fields to be bound under the top conductor and only propagate in the longitudinal direction. This is called the *bound* regime. It is thus recognized that the computation of the various propagation constants is crucial to understanding the operational regimes of the microstrip leaky-wave antenna. Consequently, a major thrust of this dissertation is the calculation of these propagation constants.

1.3.5 Literature Search of Proposed Methods for Increasing Bandwidth

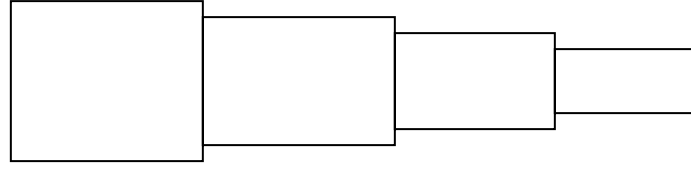
In order to tackle the challenge of increasing the bandwidth of the microstrip antenna, researchers have tried numerous methods over the past 28 years [61 – 90]. These ideas have been met with limited results and have drawbacks that would hinder their use on stealthy aircraft and missiles (size and radar signature.). This section will highlight a few of the ideas developed by the antenna community, as well as talk to each one's applicability to stealth vehicle design.

Given that the leaky-wave microstrip antenna operates with limited bandwidth (typically under 20%) [2,6], the first inclination would be to align several of these antennas (each of varied widths) in parallel with each other in order to achieve the desired frequency coverage. The drawbacks of this include the need for numerous antennas versus a single antenna, the increased costs associated with having to purchase numerous antennas, and increased space required to place these additional antennas on the aircraft.

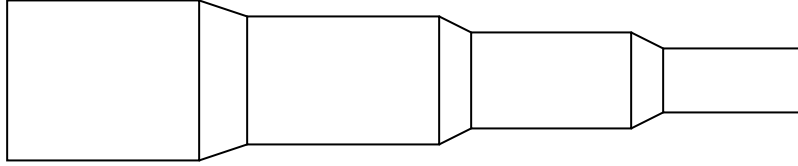
Nalbandian's and Lee's work shows that microstrip antennas placed in an array of roughly the same top-down cross-section as the THW antenna have the potential to increase the bandwidth of the radiation region [7]. However, the drawback of this work was that the thickness of the microstrip antenna went up from 0.787mm up to 1.25cm. This increase in thickness could cause the antenna to have a higher Radar Cross Section (RCS), and thus make it impractical for use on stealth aircraft. Further analysis is needed on this potential area of research to show the true impact on signature, as well as bandwidth improvement over the radiation regime.

Another approach to increasing the bandwidth of the leaky wave microstrip antenna is to modify the shape of the top conductor. By breaking-up the top conductor into sections of decreasing widths (Figure 6(a)), each section can be "tuned" to operate over a specific frequency region. However, with the introduction of multiple widths in the same top conductor comes the introduction of impedance mismatch and discontinuities that reduce the operating bandwidth and create spurious sidelobes [6]. In order to match these sections and reduce the discontinuity effects, the sections are separated by tapered transition sections (Figure 6(b)) or by tapering the top conductor linearly (Figure 6(c)). Modest bandwidth improvement is claimed by the authors by using these techniques, although the results are not clearly shown. Further analysis of this method is required in order to show the impact over the radiation regime.

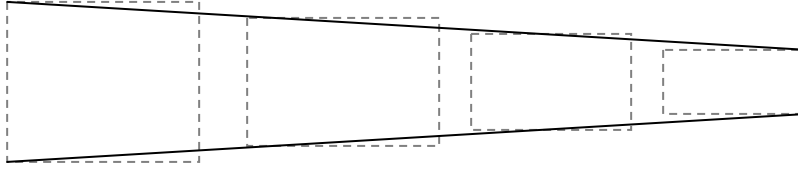
The last method that has potential to increase the bandwidth of the leaky wave antenna is to periodically place capacitors down the length of the top conductor (Figure 7). This method was shown by Luxey and Laheurte to act as either a capacitive or an



(a) Original multi-section microstrip leaky-wave antenna



(b) Insert a tapered transition section



(c) Taper the steps linearly

Figure 6: Two methods used to modify the original step discontinuities. (a) The original multisectional microstrip leaky-wave antenna. (b) Inserts additional tapered sections between each two adjacent original sections. (c) Tapered linearly and the original sections are shown in solid lines. [6]

inductive load (depending on the separation of the capacitors) that will move the $\beta k_0 = 1$ point to the right (increase f_{high}) [8]. Although bandwidth improvement was not specifically claimed in the paper, the phase constant, β , was shown to shift as the distance between capacitors was varied. No plots were given showing the affects on the attenuation constant, α , and, thus, no conclusions can be drawn from the paper regarding how much bandwidth improvement can be gained from this technique. However, the manipulation of the propagation constants is the key towards obtaining bandwidth improvement over the radiation regime. Because of this, the use of capacitors along the

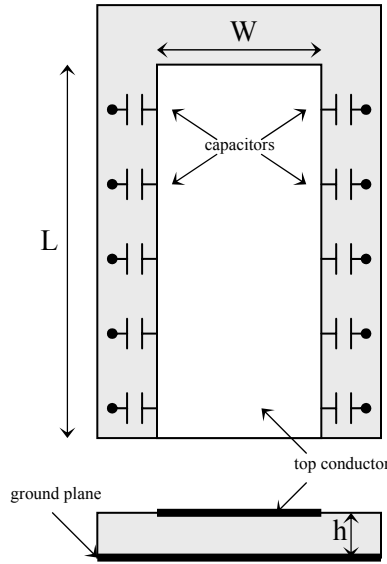


Figure 7: Leaky-wave microstrip antenna loaded by capacitors [8]

length of the top conductor should be considered as a means for potential bandwidth improvement. Future investigation is required.

All of these methods mentioned offer, or claim to offer, some improvements to the bandwidth of the leaky-wave antenna. However, they are either incomplete or unclear as to what level of bandwidth improvement they can achieve within the radiation regime. Additionally, they do not give any insight as to how these new structures promote radiation or how the changes in the structure influence the propagation and attenuation characteristics.

1.3.6 Proposed Method for Increasing Bandwidth

This research looks at a novel approach to bandwidth improvement of the THW antenna – modification to the material underneath the top conducting strip (see Figure 8).

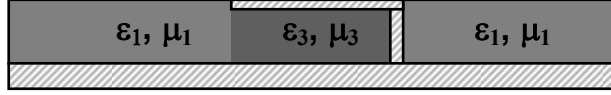


Figure 8: Microstrip with varied ϵ_3 and μ_3 under top conductor

The thought process for choosing this approach stems from the operating regimes themselves. When the traveling-wave antenna transitions from a surface mode to a bound mode, some physical phenomenology is causing the fields to become trapped underneath the strip conductor. Why is this? Why is this transition point located in the material under the strip conductor at its edge? When the antenna transitions from a surface mode to a radiation mode, why is it that energy is now allowed to radiate normal to the surface versus being trapped in the dielectric sheet? This research effort seeks to answer these questions.

Intuitively, the reason for choosing the antenna design seen in Figure 8 stems from the phenomenology causing energy to be physically “trapped” under the strip conductor in the bound regime. This is similar to energy being reflected at the junction of two different mediums. If the material under the strip conductor were varied, it might allow for more energy to leak out into the dielectric sheet, thus promoting surface wave leakage. If more energy were allowed to enter the surface regime, then the thought is that this would lead to more energy being able to propagate away from the surface in the radiation regime. More energy radiating would translate to greater bandwidth due to increased attenuation.

As shown in Figure 8, the baseline THW antenna will be modified slightly. Only the substrate that lies directly under the top conductor will be modified to have a different permittivity (ϵ_3) than the permittivity of the rest of the dielectric slab (ϵ_1). Both permittivity values (ϵ_1 and ϵ_3) will be raised and lowered and compared to the baseline THW performance. In all cases, the attenuation constant, α_z , and the phase constant, β_z , will be computed. All three regions are assumed to be non-magnetic ($\mu_1 = \mu_3 = \mu_0$).

The following chapters will analyze the baseline antenna, as well as the modified microstrip structure of Figure 8, using both computational as well as analytical methods. Insight into what causes the transitions between the operating regimes, as well as the ability to increase the bandwidth using the novel approach described previously is desired and will be investigated in this dissertation.

Chapter 2

TRANSVERSE RESONANCE AND FINITE DIFFERENCE TIME DOMAIN

2.1 Introduction

The simplistic nature of the microstrip structure (strip conductor on a grounded dielectric slab) lends itself to being able to be analyzed using multiple methods. For example, it can be represented as a transmission line to be studied analytically or easily modeled in numerous computer codes to be studied computationally. Each method has different advantages for analyzing the microstrip antenna, as well as limitations.

This chapter will investigate the traveling-wave microstrip antenna analytically, as well as computationally and compare both sets of data to known results. The antenna structure will also be modified as described in the previous chapter and analyzed again using the same analytical and computational methods to determine the ability to improve/degrade the bandwidth of the radiation regime.

2.2 Transverse Resonance

2.2.1 Transverse Resonance Method

The simplistic nature of the traveling-wave microstrip structure lends itself to being analyzed analytically. The antenna can be investigated in the x-y plane to find the transverse propagation characteristics using the Transverse Resonance Method [91].

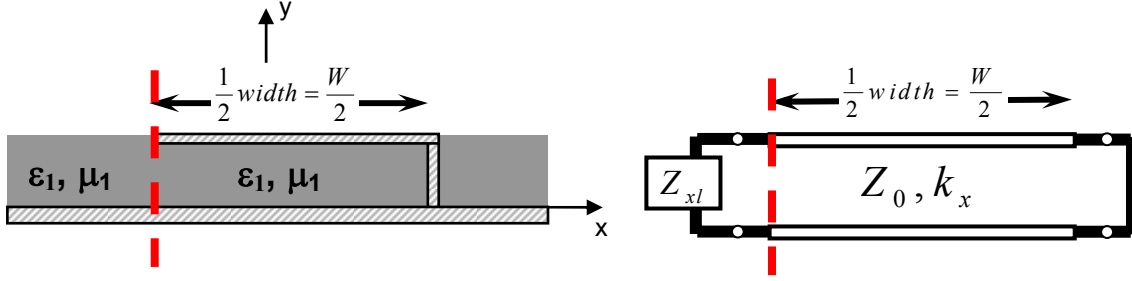


Figure 9: Representative transverse transmission line system for the baseline THW antenna

From these, the longitudinal propagation characteristics can be easily calculated using the constraint equation. Looking at the microstrip structure in the x-y plane, the cross section of the structure can be represented as a simple transmission line. Figure 9 shows the representative transmission line system.

For the transmission line representation, the dielectric sheet (of permittivity ϵ_l and permeability μ_l) becomes a load of impedance Z_{xl} at the left side of the transmission line. This impedance is an approximation derived by Chang and Kuester for a parallel-plate waveguide in conjunction with a grounded dielectric sheet [10].

At the other end of the transmission line is a short circuit load that represents the shunt in the THW antenna model. By using transmission line theory, the short can be transformed to the load location Z_{xl} through distance $w/2$. By equating these impedances, the following relationship can be derived

$$X(\zeta) - k_x W = \pm n\pi \quad n = 1, 3, 5, \dots \quad (2.1)$$

where n represents the mode number, W is the width of the strip, and X is an expression that defines the reflection coefficient at the edge of the strip [10]. See Appendix A for more details on how (2.1) is derived.

By setting $n = 1$, (2.1) represents a transcendental equation for the wave number k_x of the first higher-order mode of the structure. Numerical solution of this equation gives the corresponding transverse propagation constant (k_x). From this, the desired longitudinal propagation constant for the microstrip structure ($k_z = \sqrt{\epsilon_{r1} \cdot k_0^2 - k_x^2}$) can easily be computed, where ϵ_{r1} is the relative permittivity of Region 1. For the transmission line representation of the Transverse Resonance Method, there is assumed to be no contribution from the y -direction, thus $k_y=0$.

Equation (2.1) will be the basis for the Transverse Resonance Code (TRC) used to investigate the microstrip structures in this effort.

2.2.2 Transverse Resonance Code (TRC)

A working copy of the TRC was obtained from its author, Dr Gary Thiele. The TRC is able to compute the propagation characteristics of a microstrip structure, given the width, permittivity, and permeability of the antenna. The first step in applying the TRC to the modified microstrip structure is to validate the code for a known case. From there, the code can be altered to assess its ability to accurately compute the propagation characteristics of the modified microstrip structure.

In order to validate the TR code, the baseline THW antenna in Figure 9 was used ($d = .787\text{mm}$, $W/2=7.5\text{mm}$, $\epsilon_l = 2.33$) and the results were compared with the known frequency range of the radiation regime (from 5.95 to 8.2 GHz) [5]. Figure 10 shows the results of checking the TRC for validity. The TRC results match the frequency range of

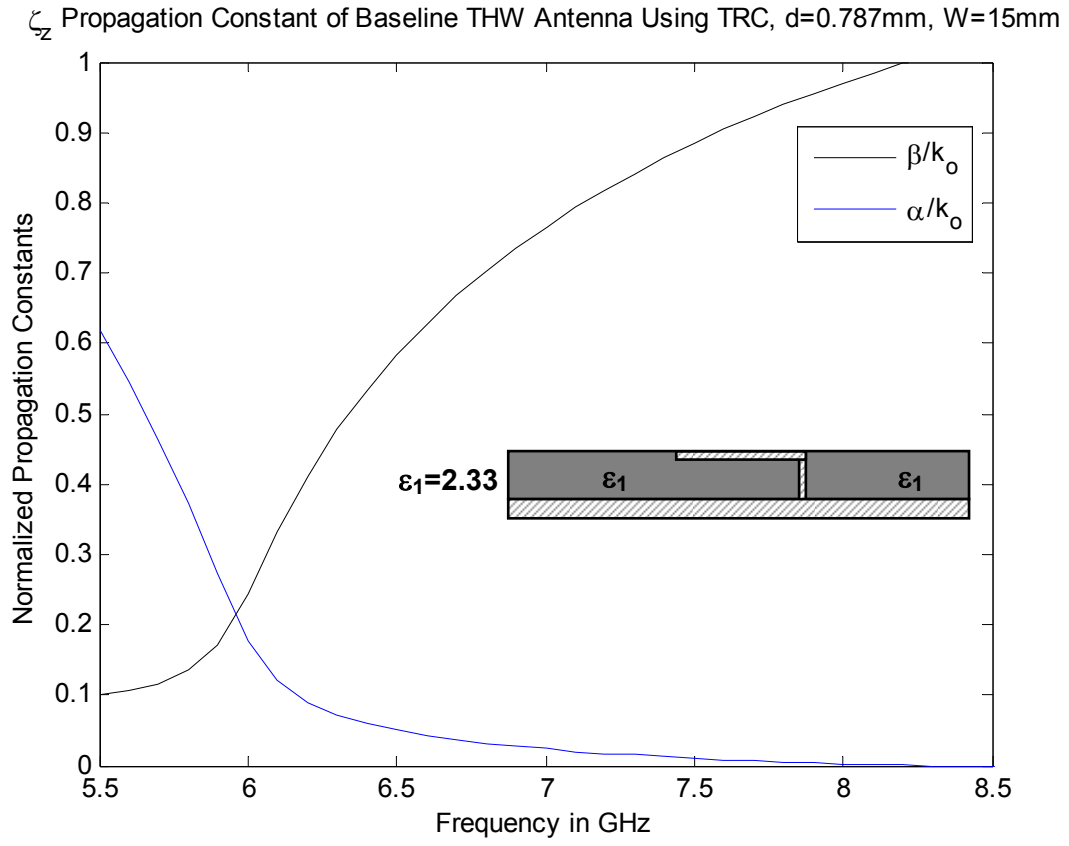


Figure 10: TRC approximation of leaky-wave propagation constants for baseline THW antenna.

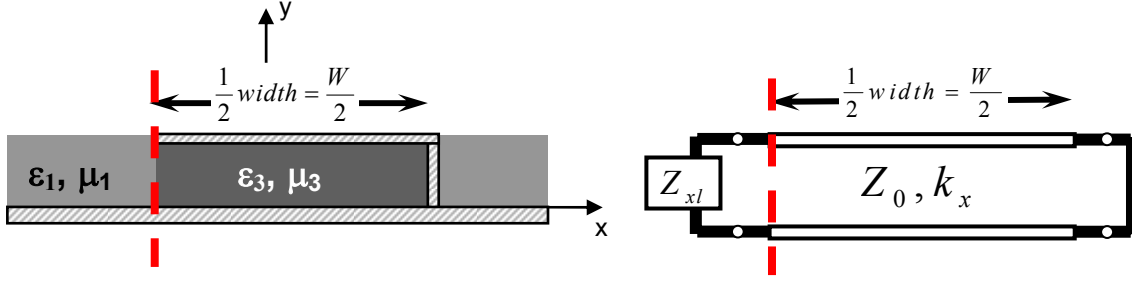


Figure 11: Representative transverse transmission line system for the modified THW antenna

the radiation regime for this particular microstrip structure (permittivity, height, width). The values in Figure 10 are identical to those found by Zelinski [5], who also compared his values to those validated by Lee [91].

Appendix B further investigates the microstrip traveling-wave antenna, primarily over the radiation regime, to show the impact of varying the width of the strip conductor and varying the permittivity of the dielectric sheet.

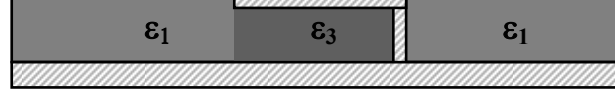
2.2.3 Variations of Microstrip Structure Using TRC

The TRC has shown excellent agreement with the known operating regimes of the baseline microstrip antenna. The next step in using the TRC is to look at the proposed modified microstrip structure (Figure 11) and determine how well TRC predicts the propagation constants.

The first step in modifying the TRC to handle varied materials under the strip conductor was to split the code into three steps: treat the microstrip as a baseline (non-modified) antenna and compute the admittance (or impedance) of the dielectric sheet using the standard method; use the modified permittivity ϵ_3 to compute the new

Table 1: Test Matrix for Varied Permittivity Under Top Conductor for TRC Predictions.

Top Conductor Width (in mm)	ϵ_1	ϵ_3
7.5	1.03	2.33
7.5	1.33	2.33
7.5	2.33	2.33
7.5	3.33	2.33



transverse propagation constant (k_x) of the transmission line; and combine the two results into (2.1) and drive this equation to zero to give the new transverse propagation constant (k_x). From this, the longitudinal propagation constant (k_z) can be computed using the relation $k_z = \sqrt{\epsilon_{r1} \cdot k_0^2 - k_x^2}$.

In order to compare results to the previous data, the physical dimensions of the modified antenna were the same as the baseline THW antenna ($d = .787\text{mm}$, $W=7.5\text{mm}$). For the permittivities, the values listed in Table 1 were used. Starting from the baseline permittivity ($\epsilon_l = 2.33$) a representative lower permittivity ($\epsilon_l = 1.33$) and higher permittivity ($\epsilon_l = 3.33$) were chosen to show the affect of these changes to the sheet. The last permittivity selected ($\epsilon_l = 1.03$) showed the affect of making the sheet essentially made of air. As before, all permeabilities were assumed non-magnetic ($\mu_0=\mu_1=\mu_2=\mu_3$).

It can be seen in Figures 12-14 that the changes to the microstrip structure caused dramatic changes to the radiation regime. Figure 12 shows the case where the dielectric sheet has a permittivity of $\epsilon_l = 1.33$ and the volume under the top conductor has a permittivity of $\epsilon_3 = 2.33$. For this case, TRC predicts the bandwidth of the radiation regime to increase from 2.25 GHz (for the baseline case) up to 6.55 GHz. Figure 13

Table 2: TRC Predicted Bandwidth for Varied Permittivity Under Top Conductor.

ϵ_1	ϵ_3	BW in GHz	BW%
1.03	2.33	24.05	133.8%
1.33	2.33	6.55	71%
2.33	2.33	2.25	32.6%
3.33	2.33	1.41	21.2%



shows the case where $\epsilon_1 = 1.03$ and $\epsilon_3 = 2.33$. From this, the new bandwidth can be computed to be 24.05 GHz. Conversely, Figure 14 shows a decrease in the bandwidth down to 1.41 GHz for the case where $\epsilon_1 = 3.33$ and $\epsilon_3 = 2.33$.

Physically, these results make sense although it is unknown at this point as to the validity of the amount of increase or decrease in bandwidth. This is due to the uncertainty of whether the modified TRC is accurate. For the cases where the bandwidth increases, the permittivity ϵ_1 of the dielectric sheet decreased. With the decrease in permittivity of the sheet, the fields around the antenna structure are less tightly bound to the substrate, thus more leakage can occur. The opposite holds true for the case where the bandwidth decreases (where the permittivity ϵ_1 of the dielectric sheet increased). With the increase in permittivity of the sheet, the fields around the antenna structure are more tightly bound to the substrate, thus less leakage.

All three of these cases are compared with the baseline case ($\epsilon_1 = 2.33$ and $\epsilon_3 = 2.33$) in Table 2. Here, the percentage bandwidth is also computed. In order to "normalize" the bandwidth measurements, the percentage bandwidth is used instead of absolute bandwidth. Resultant bandwidth is given as: $BW\% = (f_{high} - f_{low}) / f_c$, where f_{high} is the frequency at which $\beta/k_0 = 1$, f_{low} is the frequency at which $\alpha = \beta$ and is also called

the cutoff frequency for the leaky regime, and f_c is the center frequency of the leaky regime.

The first two cases show significant increase in BW% - with one doubling the baseline value and the other quadrupling it. The last case cuts the BW% by almost a third. These results will be compared later in this dissertation with the results derived from two other prediction methods in order to assess their validity.

2.2.4 TRC Conclusions

Overall, the TRC gives very good insight into the operating frequencies of the radiation and propagation regimes of a traveling-wave microstrip antenna. These frequencies are derived directly from the propagation constants computed by the TRC for a given set of parameters. However, TRC does not give much insight as to what is driving the phenomenology within the structure or solve for the currents/fields within the structure.

When computing the propagation characteristics of the modified THW antenna, TRC gives results that show significant levels of increase/reduction in bandwidth for the radiation regime. Without any “known” data to compare to, further analysis must be performed to validate these results. This will be done in the following section using the FDTD method, as well as the following chapters using a frequency domain full-wave analysis.

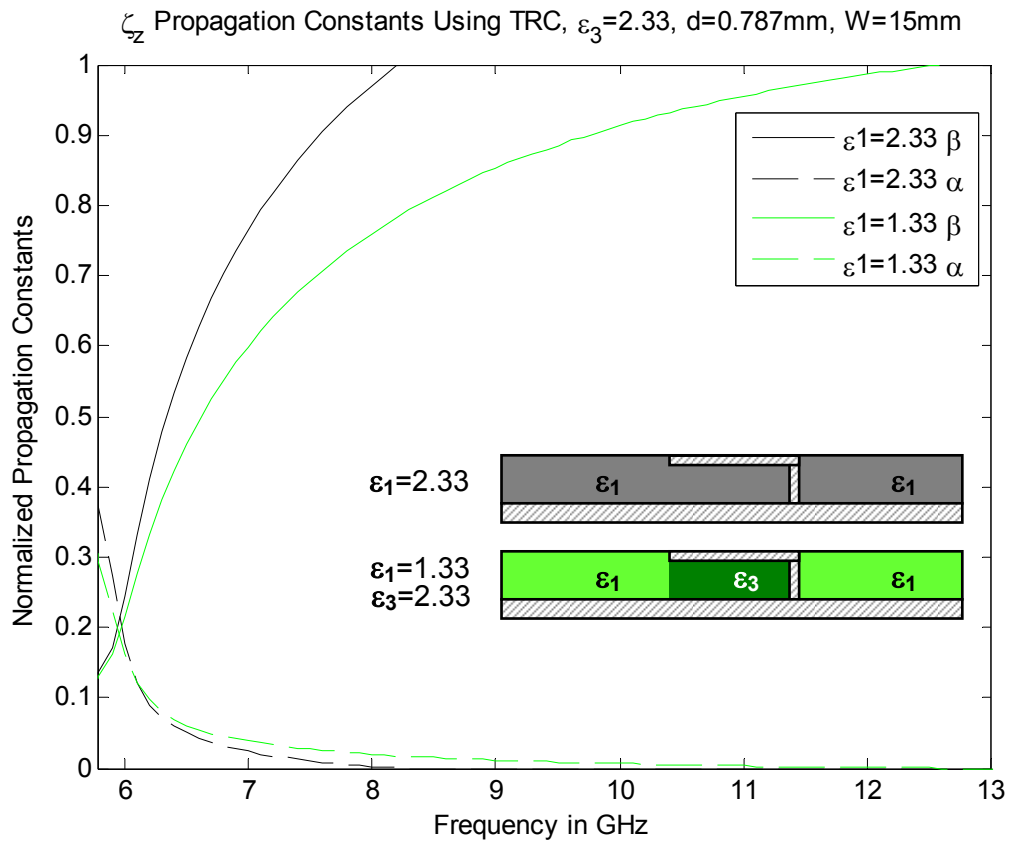


Figure 12: Propagation constants for radiation regime using TRC for $\epsilon_1=1.33$ and $\epsilon_3=2.33$.

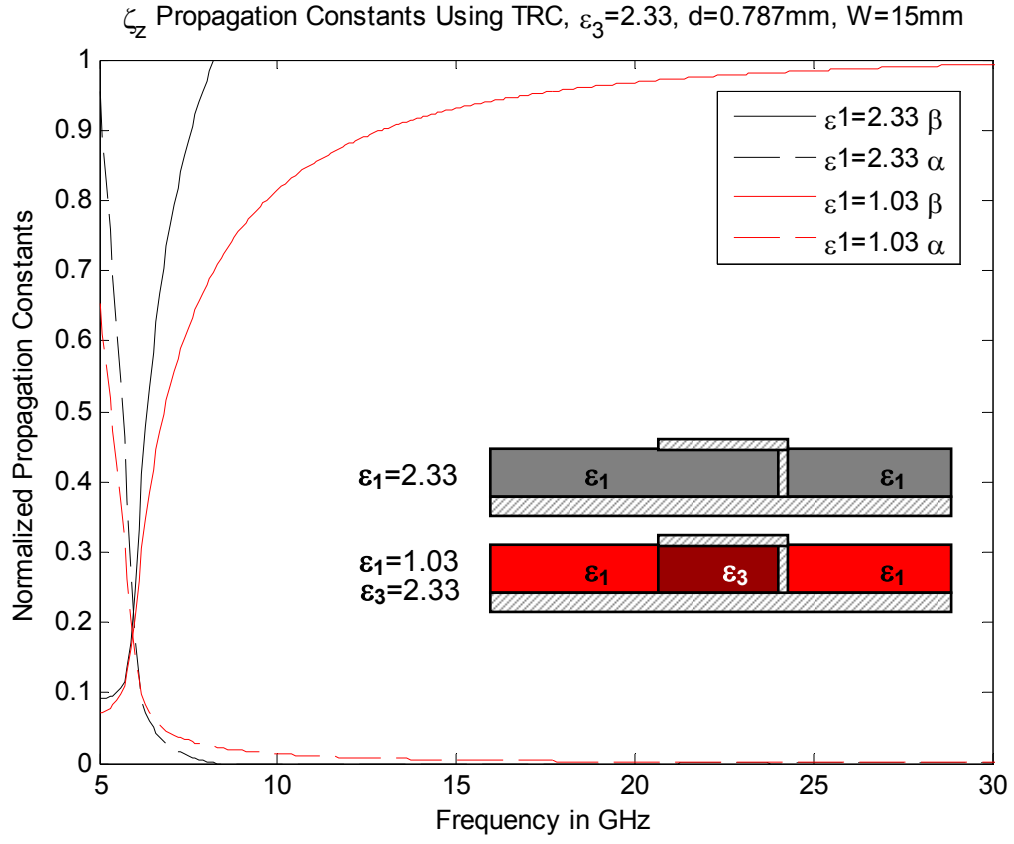


Figure 13: Propagation constants for radiation regime using TRC for $\epsilon_1=1.03$ and $\epsilon_3=2.33$

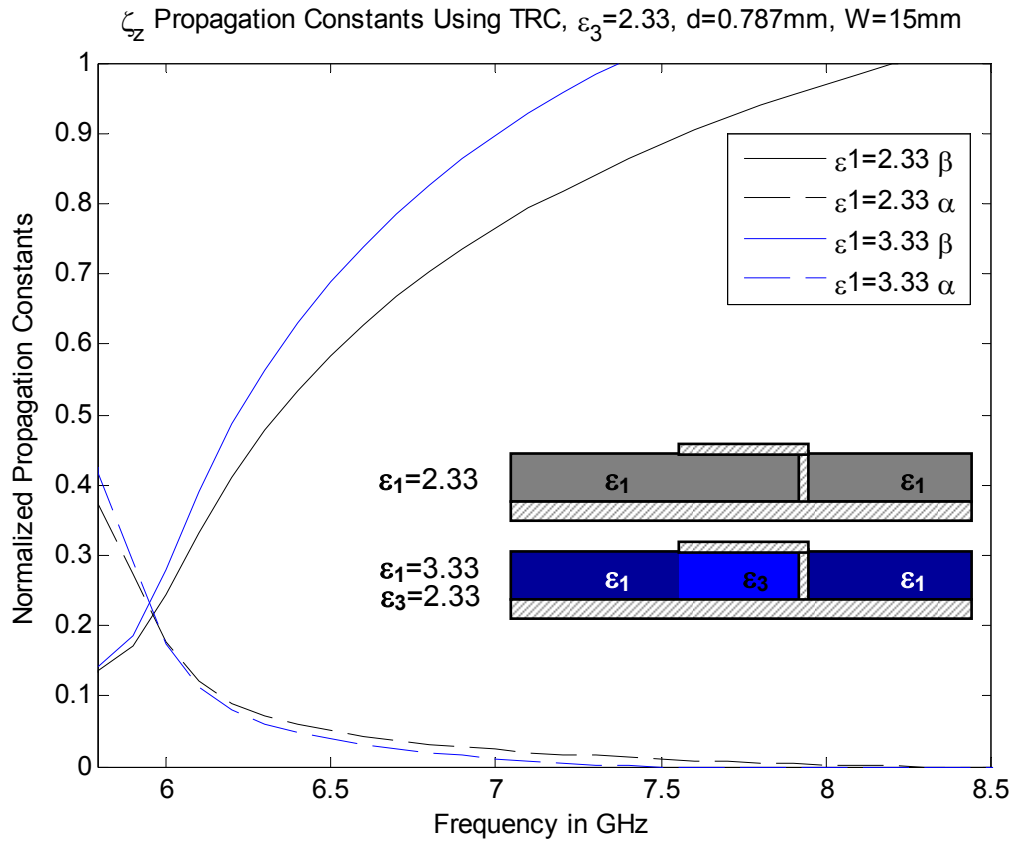


Figure 14: Propagation constants for radiation regime using TRC for $\epsilon_1=3.33$ and $\epsilon_3=2.33$

2.3 Finite Difference Time Domain

2.3.1 Background

The TRC provides a quick and fairly simple way to predict the propagation constants for a microstrip structure. However, it does not compute the fields and currents in the structure, nor does it accurately predict the constants when there are changes in the permittivity of region 3. A method that computes the fields within the structure, accommodates for changes in the materials, and computes the desired propagation constants is the Finite Difference Time Domain (FDTD) technique [92].

FDTD is a computational method for solving the time-domain differential form of Maxwell's equations directly and discretely using a space-time grid. By placing the microstrip structure into a rectilinear grid-space, discretizing it into a set number of finite elements that account for material and dielectric properties, and defining the location of the source or input; the electric and magnetic fields for each element can be computed for a single time step. The electric and magnetic fields are actually spaced $\frac{1}{2}$ of a cell apart from each other in order to accommodate for the interactions between them. The FDTD code actually computes \vec{E} at one time step, then computes \vec{H} one half of a time step later. By alternating between computing \vec{E} , then \vec{H} , then \vec{E} , etc.; the resultant fields "propagate" in time [11].

In order to investigate the fields in the microstrip structure studied here a grid-space of infinite extent is required. Given that this is not computationally feasible, the grid-space will be truncated by using a Perfectly Matched Layer (PML) as the outer layer of the FDTD grid [93]. PMLs essentially make the grid-space look infinite in extent by

absorbing any incident fields and not allowing for any fields to be reflected back to the microstrip structure. The PML is matched perfectly to the other layers it comes in contact with (thus, $\Gamma = 0$), but has absorbing properties that cause the fields to be attenuated.

2.3.2 FDTD Set-Up

A copy of an FDTD code previously used to analyze the THW antenna was obtained. The code was loosely based on the 3-D Hagness-Willis FDTD code, but modified in order to optimally handle the THW structure and to compute the propagation constants from the electric field data [5].

Before the process by which the propagation constants are extracted is explained, it is necessary to understand how the FDTD simulation was set-up. In order to save time, the same PML thicknesses, substrate thickness, air gap thickness, and location of the source performed by Zelinski [5] in his efforts to measure the baseline THW antenna were used in this research. His efforts optimized the parameters to measure the baseline antenna. Figure 15 shows the orientation of the THW antenna and the location of the PML layers, PECs, and air gap (ϵ_0). The location of the source is indicated with a red dot in the figure.

The PMLs varied from six to twelve cells thick (frequency dependent) in order to adequately absorb energy incident onto them. Plus, only two cells of ϵ_f substrate or air were required before entering either PML. This left a minimum of eight cells that were

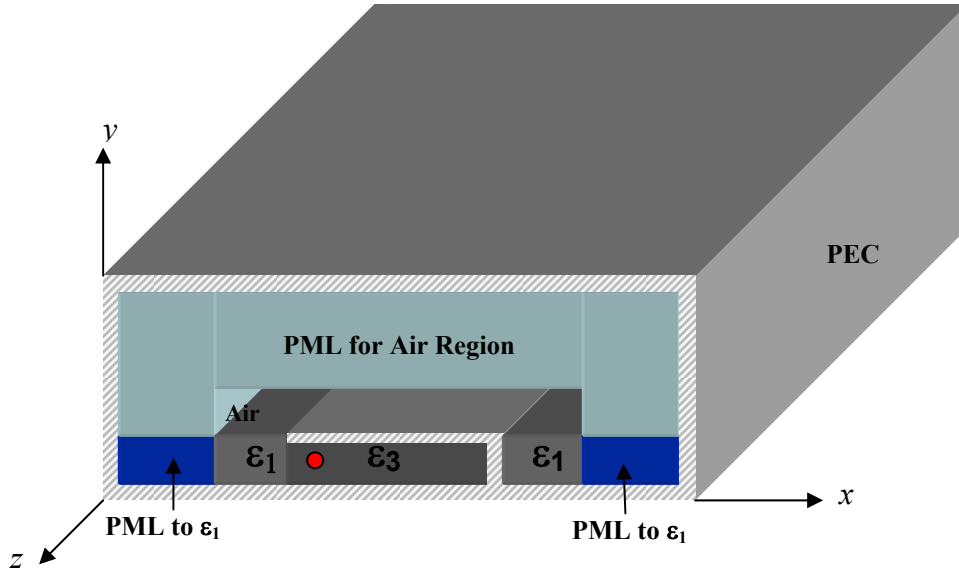


Figure 15: Modified THW antenna with PML layers and source location (in red)

required to be around the microstrip structure in order to not introduce any artifacts into the simulation.

The baseline THW antenna is 66.9mm long x 7.5mm wide x 0.787mm tall. This translates to 142 x 47 x 5 cells at 6.7GHz (the longitudinal direction is scaled by a factor of 3). Combined with the dimensions of the gaps and PMLs, this comes to 158,790 cells required to properly represent the microstrip structure.

Two other structures were also investigated in order to gain confidence in the FDTD results. The first was to increase the amount of ϵ_l dielectric sheet on the other side of the shunt (Figure 17). The second was to make the microstrip a full-width antenna with varied ϵ_3 substrate under the strip, but to still include the shunt (Figure 18). The shunt is required in order to block the dominant mode and force the antenna to operate as a leaky wave antenna. The resultant propagation constants for each were determined and

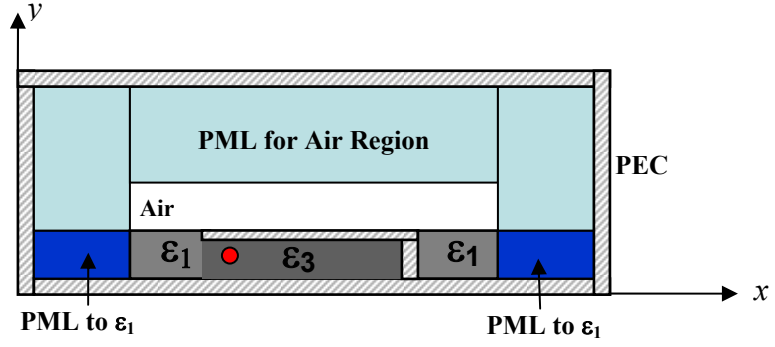


Figure 16: Modified THW antenna with PML layers and source location (in red)

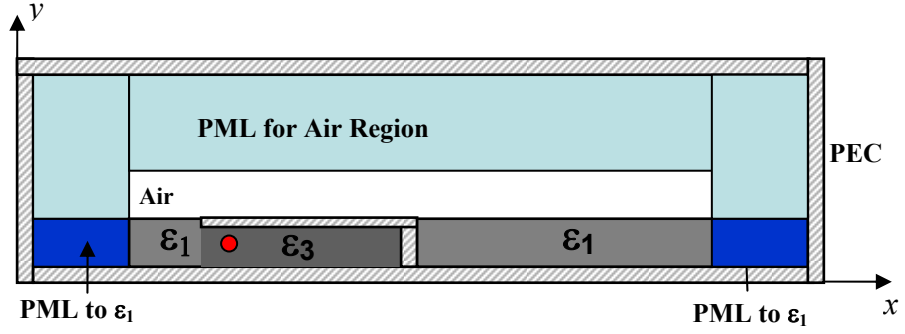


Figure 17: Modified THW antenna with increased slab with PML layers and source location (in red)

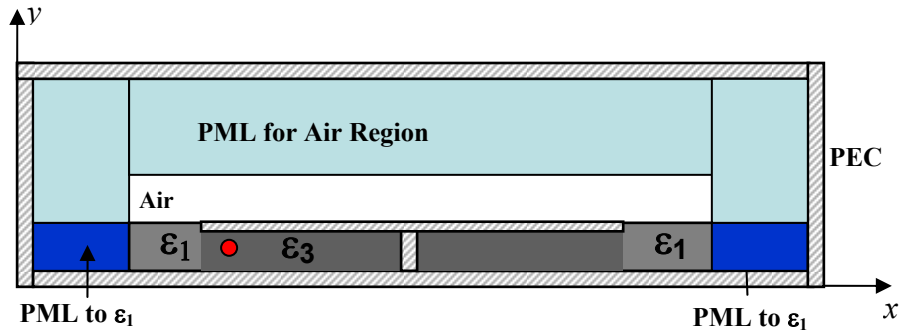


Figure 18: Modified TFW antenna with PML layers and source location (in red)

found to match the results of the original set-up in Figure 16. As such, the original set-up can be used with confidence to determine the propagation characteristics.

2.3.3. Extraction of Propagation Constants Using FDTD

The process by which the propagation constants are extracted for a particular microstrip structure is a fairly straightforward one, albeit very time consuming. A y -directed sinusoidal source \vec{E}_i is introduced into the structure and the fields are propagated over thousands of time step iterations (equivalent to 30 periods at a given frequency). At the end of these 30 periods, all fields within the structure have propagated and attenuated to a steady state. It is at this point that the magnitude of the y -directed fields can be used to compute the attenuation and phase constants for the structure. The location of the cells from which these fields are taken is just 1 cell to the left (in x) of the red dot (source location) in Figure 16. This point stays constant in x and y , but runs the length of the structure in z .

Typical FDTD output can be seen in Figures 19 and 20. For this example, 325 cells are used to represent the length of the structure. The first 12 cells are used to represent the PML in the z -direction and the source can be seen at cell number 17. The y -directed electric fields propagate along the length of the antenna from the source down to cell number 317. The last 12 cells represent the PML in the z -direction at the end of the length of the structure.

In order to extract the propagation constants from the y -directed electric field data, it is necessary to start with the expression for that field

$$E_y(z, \omega) = E_0 e^{-jk_z z} \Rightarrow E_y(z, t) = \text{Re}\{E_0 e^{-jk_z z} e^{j\omega t}\} \quad (2.2)$$

if the sinusoidal excitation is in steady state. Equation (2.2) can be re-written using the expression for $k_z = \beta_z - j\alpha_z$

$$E_y(z, t) = E_0 e^{-\alpha_z z} \cos(\omega t - \beta_z z) \quad (2.3)$$

Taking the natural log of both sides gives

$$\begin{aligned} \ln \left| \frac{E_y(z, t)}{E_0} \right| &= \ln \left(e^{-\alpha_z z} |\cos(\omega t - \beta_z z)| \right) \\ &= \ln e^{-\alpha_z z} + \ln |\cos(\omega t - \beta_z z)| \\ &= -\alpha_z z + \ln |\cos(\omega t - \beta_z z)| \end{aligned} \quad (2.4)$$

The propagation characteristics can be computed using (2.4) and the natural log of the normalized y -directed electric field data. Figure 20 shows a typical plot of such data. By measuring the distance in meters between peaks (or between nulls), the period of the electric field is obtained (λ_z in the figure). Using the fundamental relation: $\beta_z = 2\pi / \lambda_z$, the desired phase constant, β_z , can be computed. As an example, Figure 21 reveals that $\lambda_z/2=0.035$ m, resulting in $\beta_z/k_0 = 0.64038$.

Examination of the amount of attenuation between peaks provides the value for α_z . In this case, the peak-to-peak slope of the $\ln E$ curve in Figure 20 gives the value for $\alpha_z / k_0 = 0.043335$. In order to check the accuracy of α_z and β_z , an exponential curve is produced using these values and overlaid onto the natural log plot of the raw data (see Figure 21). Figure 22 shows the same data as Figure 21, but without taking the natural log of the values.

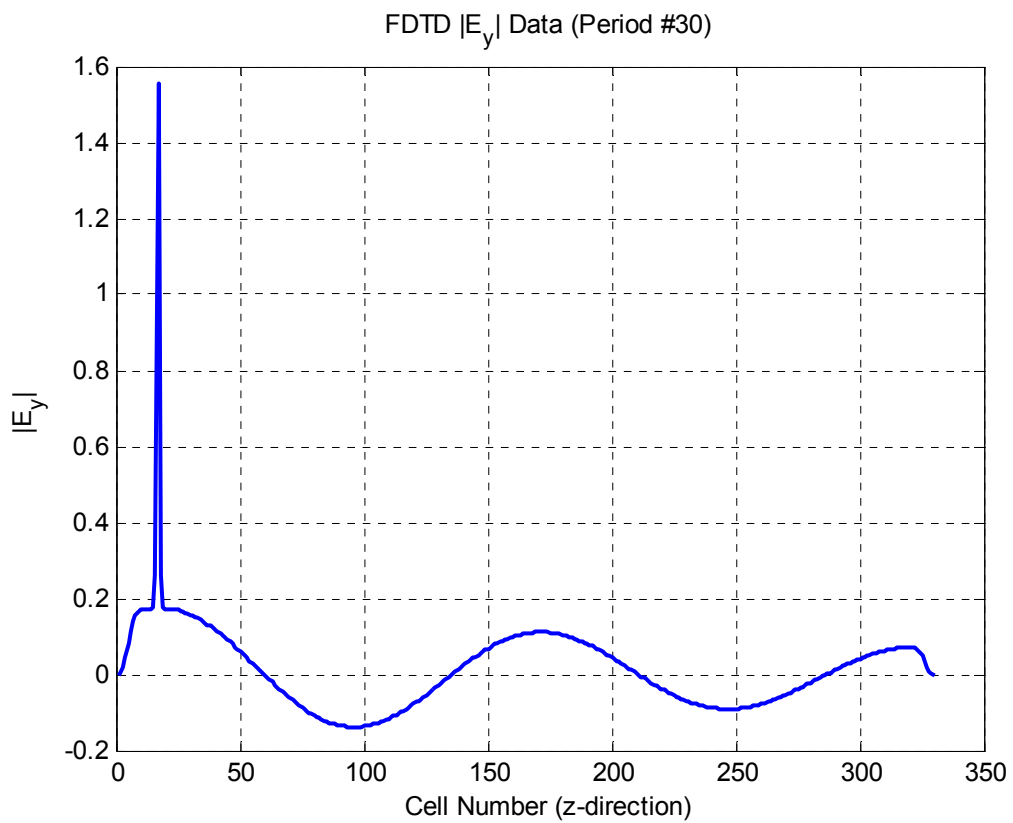


Figure 19: FDTD y-directed electric field data (magnitude only) for THW antenna taken longitudinally with x fixed at cell #18 and y fixed at cell #17. The source can be seen at cell #17 in z-direction.

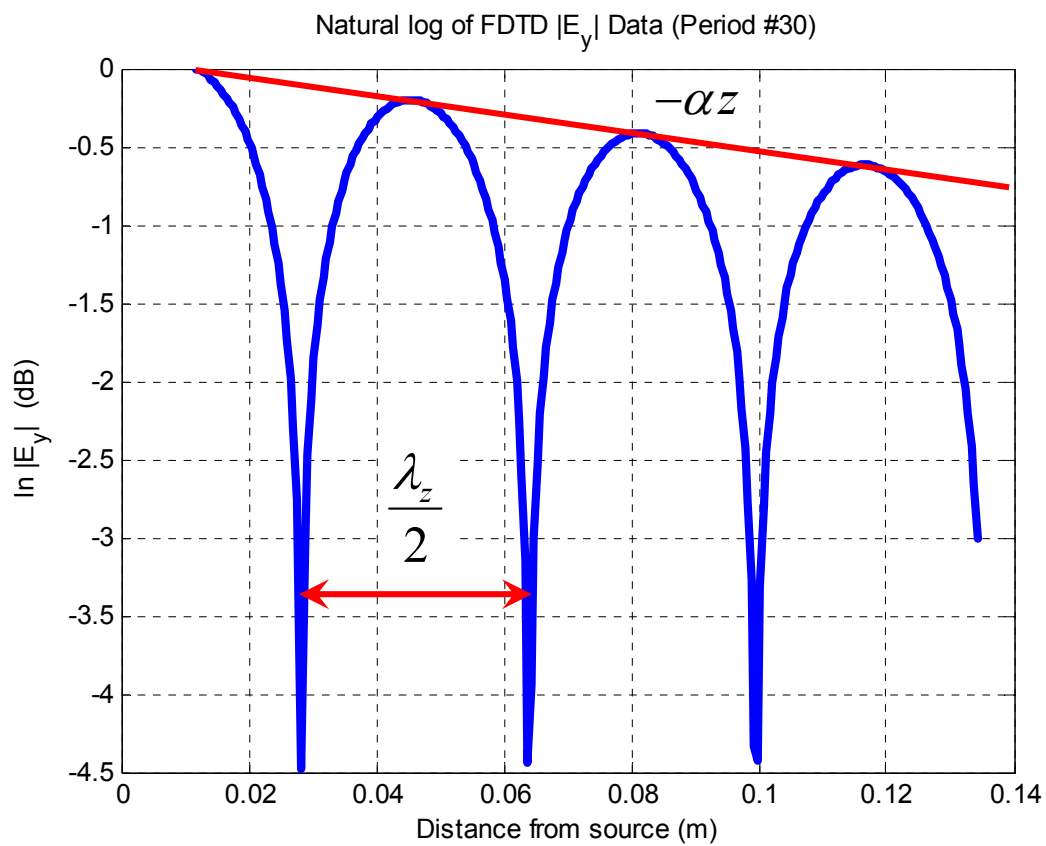


Figure 20: Natural log of FDTD y-directed electric field data (magnitude only) for THW antenna taken longitudinally with x fixed at cell #18 and y fixed at cell #17.

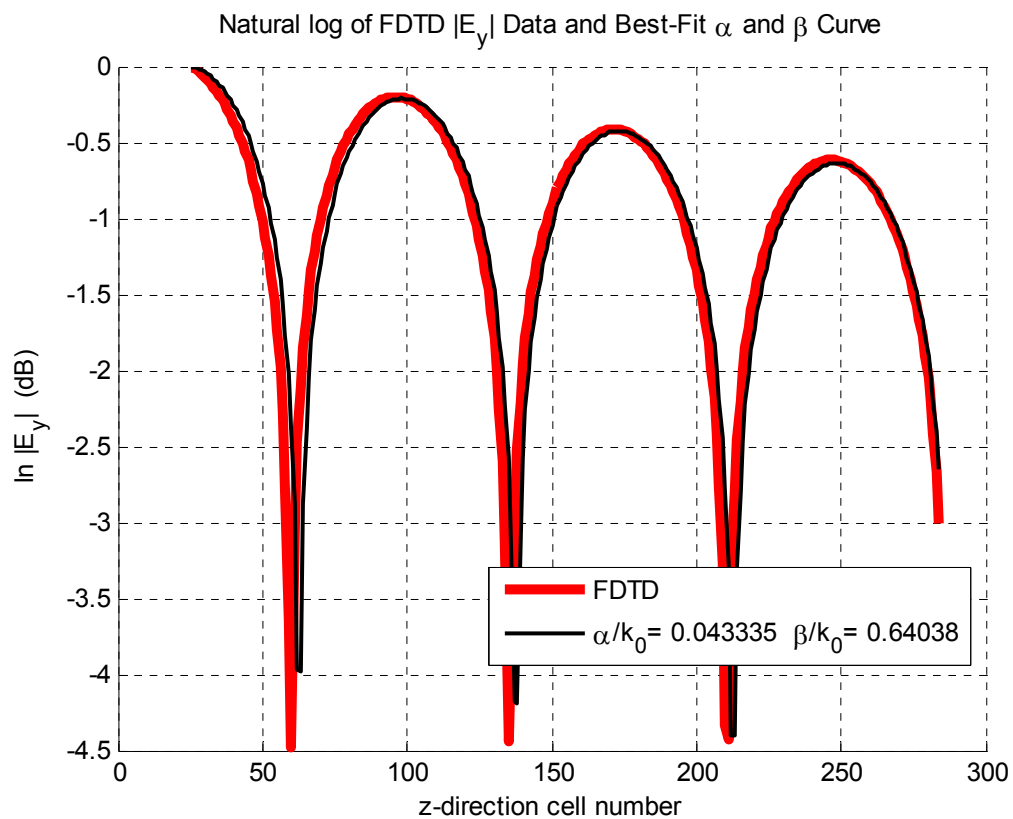


Figure 21: Natural log of FDTD y-directed electric field data (magnitude only) and corresponding best-fit α and β curve.

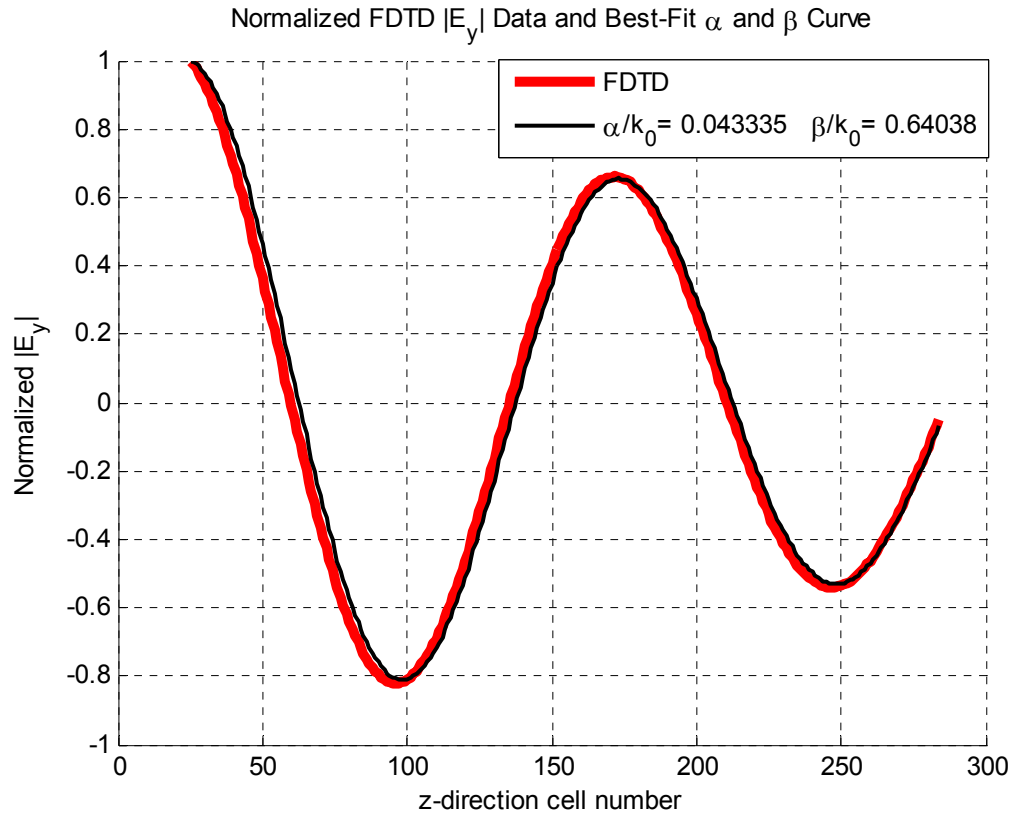


Figure 22: Normalized FDTD y-directed electric field data (magnitude only) and corresponding best-fit α and β curve.

2.3.4 FDTD Methodology and Results

The first step performed was to validate the code by reproducing the results obtained by Zelinski during his research. The parameters for the THW antenna were entered into the code and the results were compared with the TRC. As stated in the previous section, the TRC has been shown to accurately predict the propagation constants for a standard microstrip structure, thus the TRC data will be used as “truth” data for the non-modified microstrip only. From Figure 23, it can be seen that the FDTD code did a very good job predicting the propagation constants for the baseline antenna. The values for the phase and attenuation constants are within 1 to 3% of the values obtained from using the TRC for the majority of the radiation regime. The values close to cutoff (where the α and β curves intersect) tend to vary greater than the rest of the values. This is due to the nature of the FDTD results near cutoff and will be explained later in this chapter. Overall, it can still be said that the bandwidth of the baseline antenna can now be predicted using FDTD with confidence. The next step is to modify the structure and analyze the results using the same method.

Before the modified microstrip configuration could be tested, some modifications of the FDTD code were required. These modifications allowed for the material under the strip conductor to vary while keeping the rest of the structure the same.

In order to validate the changes to the code, ϵ_1 and ϵ_3 were both set to the baseline permittivity (2.33). The results were exactly the same as FDTD results for the baseline THW antenna (as shown in Figure 23), thus the code could then be used with modified ϵ_1 and ϵ_3 values with confidence.

The baseline THW antenna was modified by inserting a different permittivity ϵ_3 under the top conductor than the remainder of the substrate (ϵ_1), similar to that which was done earlier in this chapter using the TRC. Table 3 shows the test matrix used for this microstrip configuration. The values chosen in the test matrix give a range of realistic permittivity values that center around the baseline THW antenna permittivity (2.33), giving some values that are lower than the baseline case and one value that is greater. By using these values, it is desired that trends and physical insight can be gained without having to perform dozens of test cases.

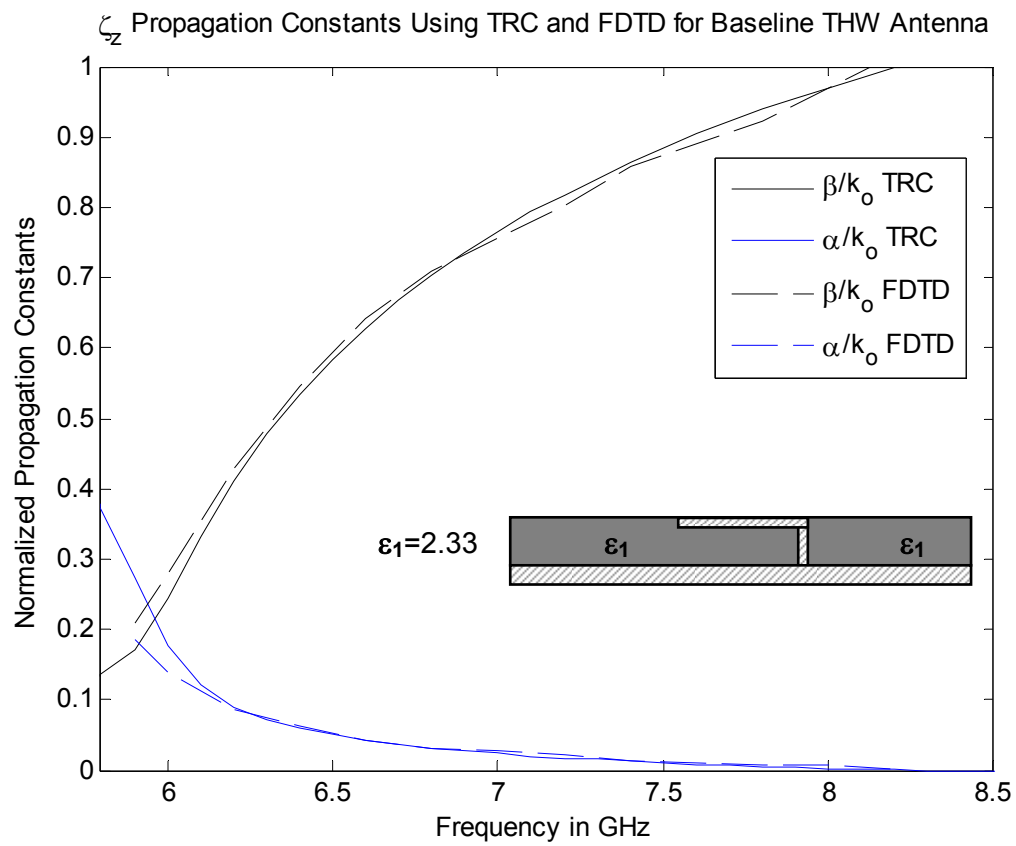


Figure 23: TRC and FDTD predictions of propagation constants for baseline THW antenna.

Table 3: Test Matrix for Varied Permittivity Under Top Conductor Using FDTD.

Top Conductor Width (in mm)	ϵ_1	ϵ_3
7.5	1.03	2.33
7.5	1.33	2.33
7.5	2.33	2.33
7.5	3.33	2.33
7.5	1.03	1.33
7.5	1.33	1.33
7.5	2.33	1.33

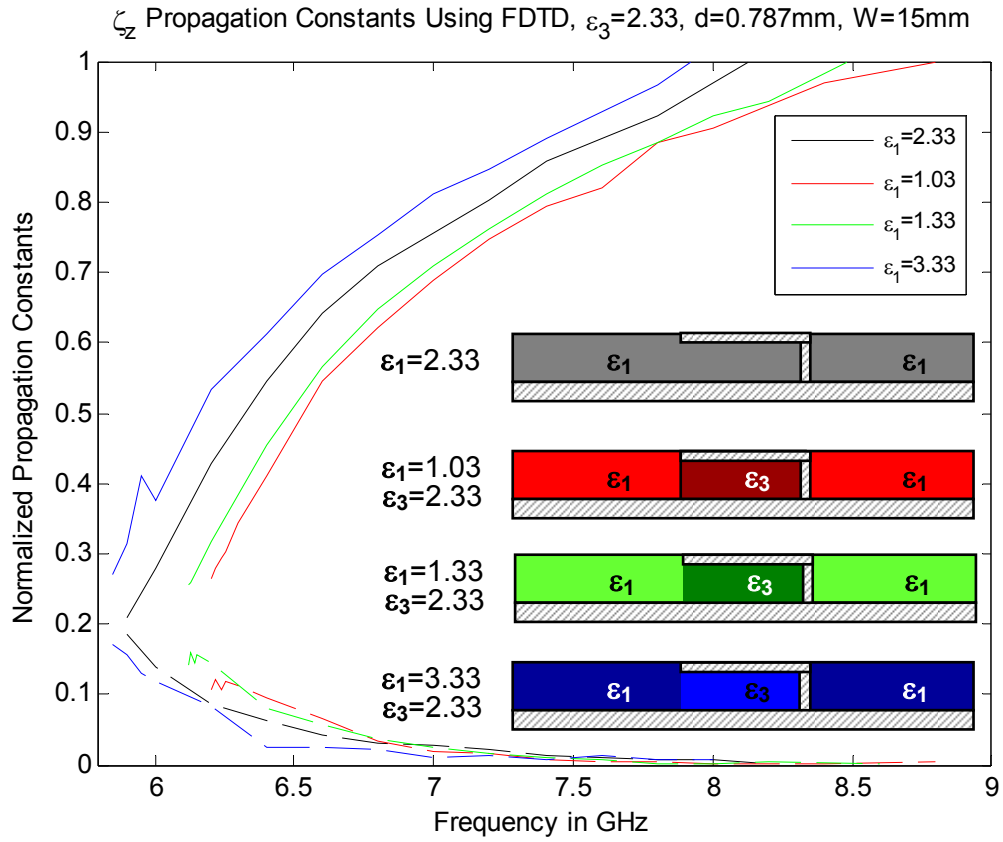
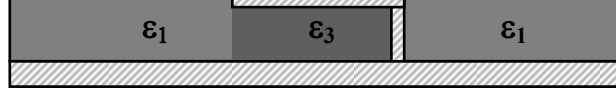


Figure 24: FDTD prediction of propagation constants for modified THW antenna.

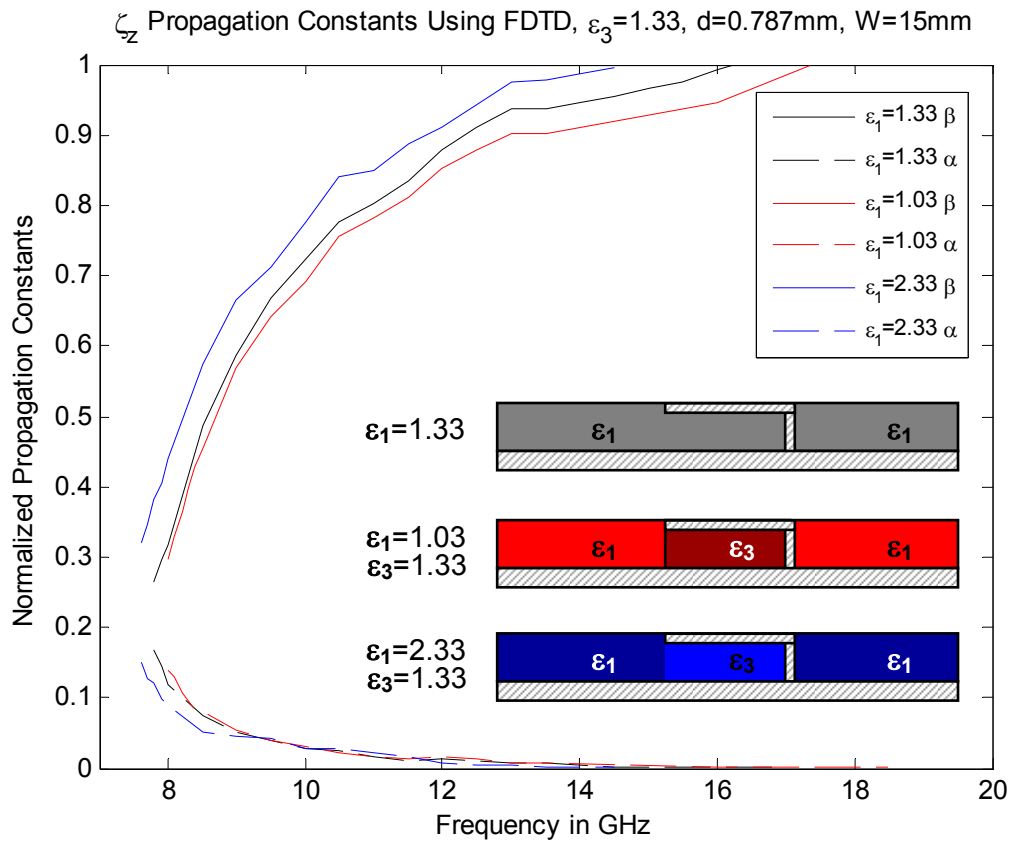


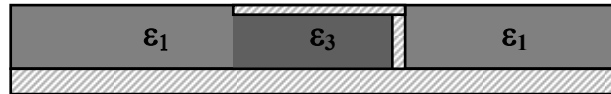
Figure 25: FDTD prediction of propagation constants for microstrip with $\epsilon_3 = 1.33$.

Figures 24 and 25 show the affect of changing the permittivity of region 1. The plots show cases where the permittivity of the substrate under the top conductor was kept constant and the permittivity of the rest of the substrate sheet was varied.

As with the TRC predictions, the bandwidth and percentage bandwidth of the modified microstrip antenna was determined from the plots. Table 4 summarizes these results for the data seen in Figures 24 and 25 and compares them to the corresponding TRC data obtained in the previous section.

Table 4: FDTD Predicted Bandwidth for Varied Permittivity Under Top Conductor.

ϵ_1	ϵ_3	FDTD BW in GHz	FDTD BW%	TRC BW in GHz	TRC BW%
1.03	2.33	2.7 GHz	36.24%	24.05 GHz	133.8%
1.33	2.33	2.43 GHz	33.48%	6.55 GHz	71.0%
2.33	2.33	2.25 GHz	32.17%	2.25 GHz	32.6%
3.33	2.33	2.12 GHz	30.90%	1.41 GHz	21.2%
1.03	1.33	9.54 GHz	75.89%	34.3 GHz	138.0%
1.33	1.33	8.56 GHz	71.76%	8.7 GHz	72.3%
2.33	1.33	7.25 GHz	65.76%	2.8 GHz	31.1%



From the plots, several trends can be observed:

- When $\epsilon_1 = \epsilon_3$, the propagation constants match the TRC predictions very closely, as expected.
- As the permittivity of the sheet is lowered, the cutoff frequency of the radiation regime is increased, similar to decreasing ϵ_r in a loaded rectangular waveguide.
- As the permittivity of the sheet is increased, the cutoff frequency of the radiation

regime is decreased, similar to increasing ϵ_r in a loaded rectangular waveguide.

- The bandwidth of the radiation regime does increase as the permittivity of the sheet is lowered and the permittivity of the material under the top conductor is held constant (8.43% improvement by lowering ϵ_l from 2.33 to 1.03 in Figure 24). The fields are less tightly bound to the substrate in the lower permittivity dielectric, thus more leakage.
- The bandwidth of the radiation regime does decrease as the permittivity of the sheet is increased and the permittivity of the material under the top conductor is held constant. The fields are more tightly bound to the substrate in the higher permittivity dielectric, thus less leakage.
- The FDTD code has a very hard time accurately predicting both α and β as the frequency approached the cutoff frequency where attenuation becomes severe (where $\alpha = \beta$). This same observation was seen by Zelinski in his research using the FDTD code [5]. This is due to the waveform attenuating too rapidly ($\alpha > 0.1$) to be able to locate definitive peaks or zero crossings in the raw Ey data (Figures 26 through 28). Without these values, α and β can not be computed with accuracy. This is one of the biggest deficiencies of the FDTD code when used to calculate the propagation constants for a microstrip structure and, thus, why another method is sought to compute the constants of the structure (i.e., an integral equation formulation).
- The time required to compute one data point (i.e., one attenuation and propagation combination at one frequency) was significant. The time required to find one data

point would range from 2 to 10 hours to compute using a PC (2.66 GHz Dual Intel ® Xeon X5355 with 8GB RAM). As the frequency increased within the leaky regime, the time required to compute a data point would decrease, but still remain above an hour.

- For the modified structure, TRC does not compare well with FDTD. This is most likely due to the lack of inclusion of the y-directed fields and the coupling that takes place between those fields and the currents on the surface of the strip conductor.

Overall, the results of this modification to the microstrip structure were good, but not dramatic. The results show that variations in the impedance looking out into the substrate do affect the amount of energy leakage across the radiation regime.

The FDTD analysis of the variations of the baseline THW antenna is by no means intended to be a definitive look at what happens when modifying the material characteristics of the antenna. It is meant solely to be a "first-look" to (a) see that changing the material properties of the THW antenna does cause variations in the bandwidth of the radiation regime and (b) give a sense for how much improvement can be expected.

One of the biggest drawbacks of using FDTD to obtain the propagation constants of the antenna structures was the time required to obtain the results. Typical data runs would take 2 to 10 hours to obtain *one* propagation constant at *one* frequency on a PC.

Another deficiency of FDTD is that all that is possible is to perform a number of test cases to see what the results are (i.e., it is somewhat limited in providing fundamental physical insight into the operational characteristics of the modified antenna). These, combined with the inability of FDTD to compute the propagation characteristics for large values of α (>0.1) lead to the need to find another method to compute these constants. An integral-equation based frequency domain full-wave analysis is one such method that can more definitively provide physical insight into what changes are required to lead to more radiation. This method will be described in the following chapters.

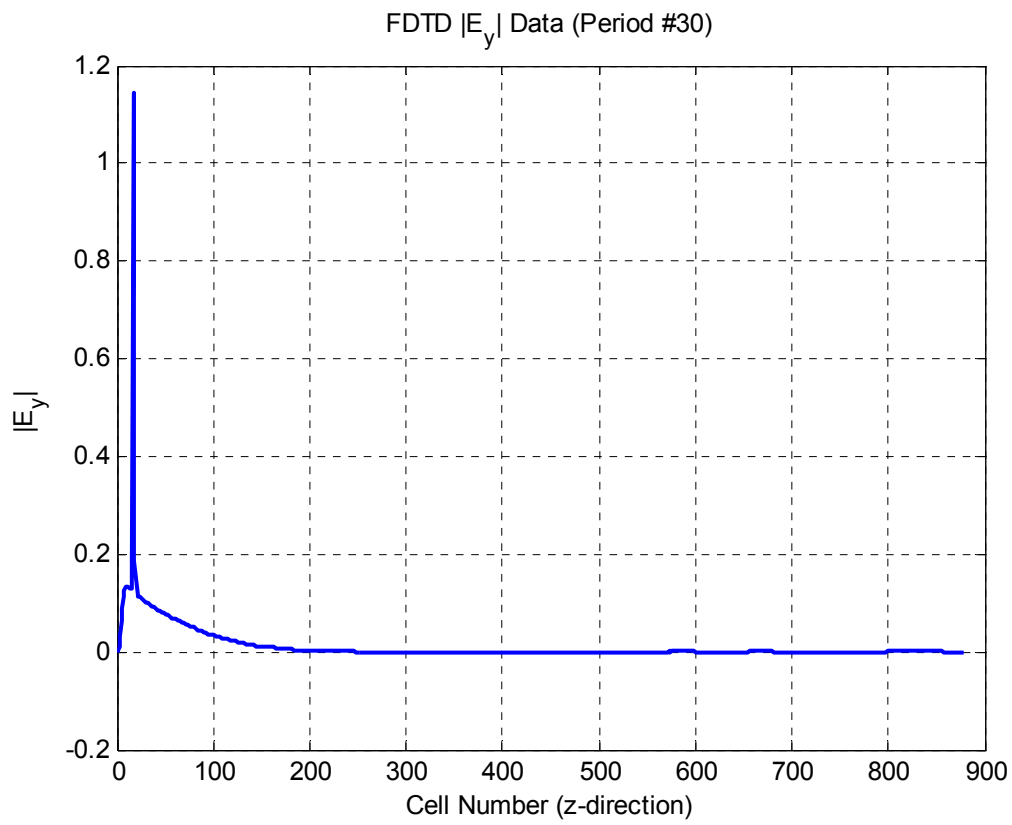


Figure 26: FDTD y-directed electric field data (magnitude only) near cut-off frequency
for radiation regime (6 GHz).

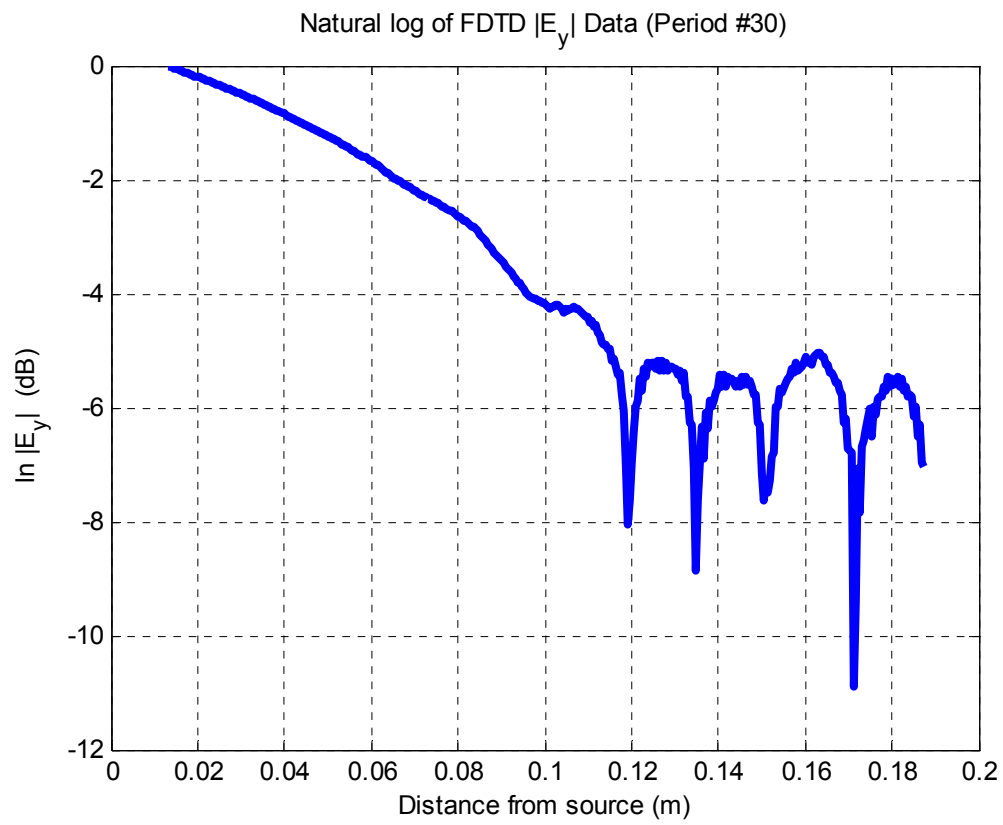


Figure 27: Natural log of FDTD y-directed electric field data (magnitude only) near cut-off frequency for radiation regime (6 GHz).

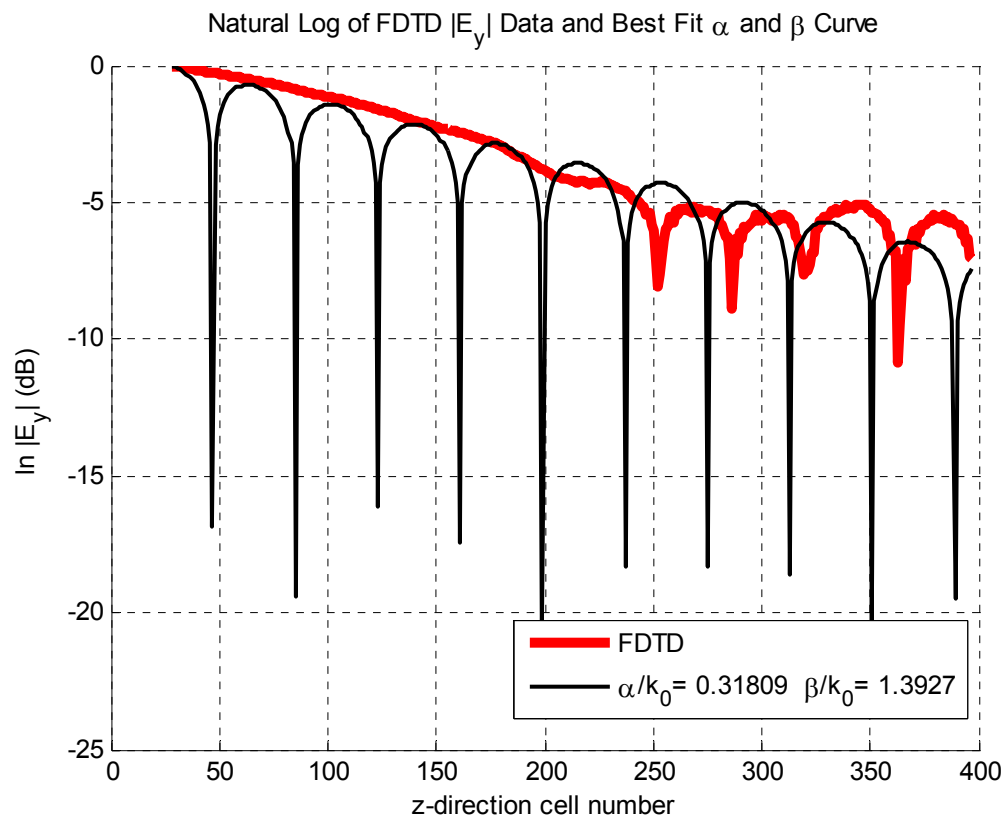


Figure 28: Natural log of FDTD y-directed electric field data (magnitude only) and corresponding best-fit α and β curve (6 GHz).

Chapter 3

GREEN'S FUNCTION FORMULATION FOR FULL-WAVE ANALYSIS

3.1 Introduction

The TRC allowed for a quick computation of the propagation constants of the microstrip structure, but did not properly handle variations within the substrate layer. FDTD allowed for variations in the structure, but was a very slow method to compute the propagation constants of the microstrip. Some FDTD data runs would take upwards of 10 hours to compute *one* propagation constant at *one* frequency on a stand-alone PC. In addition, for frequencies in which α became significant, FDTD failed to converge. FDTD also suffered a drawback in that physical insight into design parameters and how material properties effect bandwidth is somewhat obscure. Because of this, a more physically insightful and computationally efficient method of deriving the propagation constants for all frequencies is desired. One such method is to develop an integral equation formulation based on a full-wave vector potential analysis in which microstrip material perturbations are treated using equivalent currents.

3.2 Full-Wave Solution

Full-wave solutions (i.e., based on Maxwell's equations) to problems such as the microstrip antenna provide a rigorous understanding of the full electromagnetic interactions between various elements in the structure. The full-wave analysis is an

approach that typically relies on the use of a Hertzian potential ($\vec{\pi}$) which satisfies the *Hertzian potential wave equation* [12]

$$\nabla^2 \vec{\pi} + k^2 \vec{\pi} = -\frac{\vec{J}}{j\omega\epsilon} \quad (3.1)$$

where \vec{J} is the current. Field recovery, which is essential for enforcing boundary conditions, is obtained through the use of the relations

$$\vec{E} = k^2 \vec{\pi} + \nabla \nabla \cdot \vec{\pi} \quad (3.2)$$

$$\vec{H} = j\omega\epsilon(\nabla \times \vec{\pi}) \quad (3.3)$$

It will be shown in this chapter that the solution to (3.1) is given by

$$\vec{\pi}(\vec{r}) = \int_V \vec{G}(\vec{r} | \vec{r}') \cdot \frac{\vec{J}(\vec{r}')}{j\omega\epsilon} dV' \quad (3.4)$$

where \vec{G} is the Hertzian potential dyadic Green's function for the current \vec{J} immersed in the substrate layer of the grounded-slab background environment (see Figure 29).

Although the goal of this chapter is to develop the necessary Green's function, the overall process to rigorously compute the desired propagation constants is as follows:

1. Decompose the wave equation (3.1) into principal (particular) and reflected (complementary) contributions to more easily find the general solution.
2. Apply appropriate boundary conditions on the background environment to uniquely compute the unknown spectral coefficients of the wave equation solution.
3. Identify the Hertzian-Potential Dyadic Green's function of the generic volumetric current source embedded in the microstrip background environment by comparing the solution in step 2 with equation (3.4).

4. Formulate the coupled Electric-Field Integral Equations (EFIEs) by enforcing boundary conditions on the equivalent volume and surface currents of the modified THW antenna.

5. Solve the EFIEs using the Method of Moments which leads to the computation of the propagation constants.

The Method of Moments will establish the interactions between the equivalent volume currents in the region of interest and the surface currents on the strip conductor. It will be shown that the eigenvalues of the MoM matrix are inherently the propagation constants for the modified THW structure. From solving for these propagation constants at various frequencies, the leaky regimes of the structure can be determined with the aid of the constraint equation. Steps 1-3 of this process will be carried out in this chapter and steps 4-5 will be performed in the following chapter.

3.2.1 Spectral Coefficients

The first step in obtaining the Hertzian potential dyadic Green's function for a generic 3-D current immersed in region 1 is to formulate the wave equation in each of the regions of the microstrip background environment. This involves decomposing the wave equation into principal and/or reflected contributions for each region, as required. Figure 26 shows the cross-section of the microstrip background environment. This background environment only varies in the y -direction, with the height of the substrate being d .

From the figure, three distinct regions are defined: region 1 is the substrate layer of permittivity ϵ_1 , region 2 is the air layer above the antenna, and the third region is the

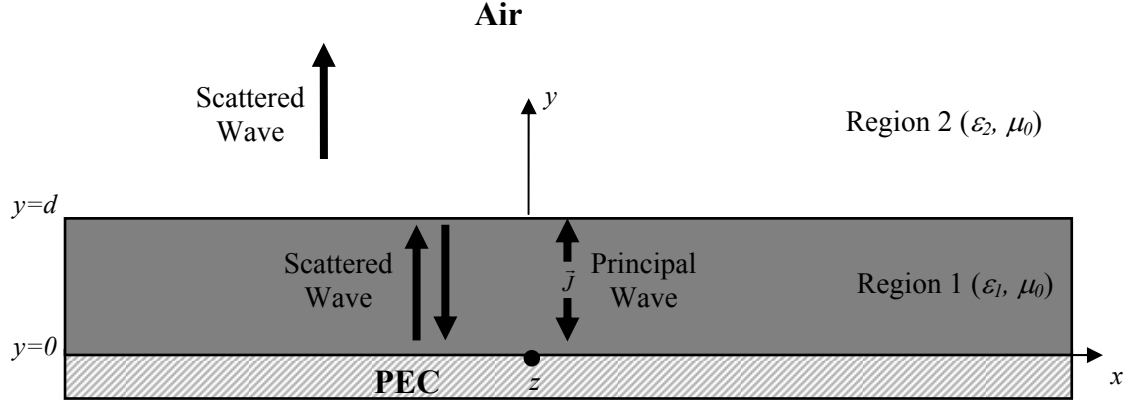


Figure 29: Cross-section of microstrip background environment. The structure is assumed to be infinite in extent along the x - and z -directions.

perfect electric conductor (PEC) layer below the substrate. Both regions 1 and 2 have a permeability of μ_0 and, thus, are assumed to be non-magnetic.

Since the equivalent volume current (due to material changes under the strip) and equivalent surface current (due to presence of the strip) are currents immersed in region 1, we are interested in the Dyadic Green's function of a generic 3-D current immersed in this region.

For the microstrip antennas used in this research, the source \vec{J} will always be located in region 1. This is represented as the *principal wave*, with a component traveling in the $+y$ and the $-y$ directions in an unbounded region of permittivity ϵ_l . This is analogous to the particular solution with no boundaries present. Due to the discontinuities at the *PEC/substrate* boundary and the *substrate/air* boundary, a *scattered wave* will be present in both regions 1 and 2. This scattered wave is analogous to the

homogeneous solution when boundaries are present. Additionally, since there is no current in region 2, there is no principal contribution.

Thus, for each region, the total Hertzian potential can be written as

$$\vec{\pi}_1 = \vec{\pi}_1^p + \vec{\pi}_1^r \quad (3.5)$$

$$\vec{\pi}_2 = \vec{\pi}_2^r \quad (3.6)$$

where $\vec{\pi}_1^p$, $\vec{\pi}_1^r$, and $\vec{\pi}_2^r$ satisfy the following wave equations

$$\nabla^2 \vec{\pi}_1^p + k_1^2 \vec{\pi}_1^p = -\frac{\vec{J}}{j\omega\epsilon_1} \quad (3.7)$$

$$\nabla^2 \vec{\pi}_1^r + k_1^2 \vec{\pi}_1^r = 0 \quad (3.8)$$

$$\nabla^2 \vec{\pi}_2^r + k_2^2 \vec{\pi}_2^r = 0 \quad (3.9)$$

with $k_1^2 = \omega^2 \mu_0 \epsilon_1$ and $k_2^2 = \omega^2 \mu_0 \epsilon_2$. Each of these vector wave equations can be decomposed into the scalar wave equations, assuming separable solutions, as

$$\nabla^2 \pi_{1\alpha}^p(\vec{r}) + k_1^2 \pi_{1\alpha}^p(\vec{r}) = -\frac{J_\alpha(\vec{r})}{j\omega\epsilon_1} \quad (3.10)$$

$$\nabla^2 \pi_{1\alpha}^r(\vec{r}) + k_1^2 \pi_{1\alpha}^r(\vec{r}) = 0 \quad (3.11)$$

$$\nabla^2 \pi_{2\alpha}^r(\vec{r}) + k_2^2 \pi_{2\alpha}^r(\vec{r}) = 0 \quad (3.12)$$

with $\alpha = x, y, z$. Given that the background environment is infinite in extent along the x and z directions, this prompts the Fourier transformation on these variables to help solve these equations. Consider the generic 2-D transform pair

$$\tilde{f}(\vec{\lambda}, y) = \int_{-\infty}^{\infty} \int_{-\infty}^{\infty} f(\vec{r}) e^{-j\vec{\lambda} \cdot \vec{r}} dx dz \quad (3.13)$$

$$f(\vec{r}) = \frac{1}{(2\pi)^2} \int_{-\infty}^{\infty} \int_{-\infty}^{\infty} \tilde{f}(\vec{\lambda}, y) e^{j\vec{\lambda} \cdot \vec{r}} d^2\lambda \quad (3.14)$$

where $\vec{\lambda} = \hat{x}\xi + \hat{z}\zeta$ ($\Rightarrow \lambda^2 = \vec{\lambda} \cdot \vec{\lambda} = \xi^2 + \zeta^2$), $\vec{r} = \hat{x}x + \hat{y}y + \hat{z}z$ and $d^2\lambda = d\xi d\zeta$. Upon

Fourier Transformation, equations (3.10) to (3.12) simplify to

$$\frac{\partial^2 \tilde{\pi}_{1\alpha}^p(\vec{\lambda}, y)}{\partial y^2} - p_1^2 \tilde{\pi}_{1\alpha}^p(\vec{\lambda}, y) = -\frac{\tilde{J}_\alpha(\vec{\lambda}, y)}{j\omega\epsilon_1} \quad (3.15)$$

$$\frac{\partial^2 \tilde{\pi}_{1\alpha}^r(\vec{\lambda}, y)}{\partial y^2} - p_1^2 \tilde{\pi}_{1\alpha}^r(\vec{\lambda}, y) = 0 \quad (3.16)$$

$$\frac{\partial^2 \tilde{\pi}_{2\alpha}^r(\vec{\lambda}, y)}{\partial y^2} - p_2^2 \tilde{\pi}_{2\alpha}^r(\vec{\lambda}, y) = 0 \quad (3.17)$$

where $p_1 = \sqrt{\lambda^2 - k_1^2}$, $p_2 = \sqrt{\lambda^2 - k_2^2}$ with the positive square root chosen so that $\text{Re}\{p_l\} > 0$ and $\text{Re}\{p_2\} > 0$ (this will be discussed in-depth in the following chapter).

The principal wave $\tilde{\pi}_{1\alpha}^p$ used in (3.15) is assumed to exist in an unbounded medium of permittivity ϵ_l , thus we can transform in y using the Fourier differentiation theorem, leading to

$$-\eta^2 \tilde{\pi}_{1\alpha}^p(\vec{\lambda}, \eta) - p_1^2 \tilde{\pi}_{1\alpha}^p(\vec{\lambda}, \eta) = -\frac{\tilde{J}_\alpha(\vec{\lambda}, \eta)}{j\omega\epsilon_1} \quad (3.18)$$

where η is the transform variable associated with y and

$$\tilde{\pi}_{1\alpha}^p(\vec{\lambda}, \eta) = \int_{-\infty}^{\infty} \tilde{\pi}_{1\alpha}^p(\vec{\lambda}, y) e^{-j\eta y} dy \quad (3.19)$$

$$\tilde{J}_\alpha(\vec{\lambda}, \eta) = \int_{-\infty}^{\infty} \tilde{J}_\alpha(\vec{\lambda}, y) e^{-j\eta y} dy \quad (3.20)$$

Solving for $\tilde{\pi}_{1\alpha}^p(\vec{\lambda}, \eta)$ in (3.18) gives

$$\tilde{\pi}_{1\alpha}^p(\vec{\lambda}, \eta) = \frac{\tilde{J}_\alpha(\vec{\lambda}, \eta)/j\omega\epsilon_1}{(\eta^2 + p_1^2)} = \frac{\tilde{J}_\alpha(\vec{\lambda}, \eta)/j\omega\epsilon_1}{(\eta + jp_1)(\eta - jp_1)} \quad (3.21)$$

From this it can be seen that the poles of this equation are located at $\eta = \pm jp_1$.

The principal wave $\tilde{\pi}_{1\alpha}^p(\vec{\lambda}, y)$ can be recovered by taking the inverse transform of (3.21), giving

$$\tilde{\pi}_{1\alpha}^p(\vec{\lambda}, y) = \frac{1}{2\pi} \int_{-\infty}^{\infty} \tilde{\pi}_{1\alpha}^p(\vec{\lambda}, \eta) e^{j\eta y} d\eta = \frac{1}{2\pi} \int_{-\infty}^{\infty} \frac{\tilde{J}_\alpha(\vec{\lambda}, \eta)/j\omega\epsilon_1}{(\eta + jp_1)(\eta - jp_1)} e^{j\eta y} d\eta \quad (3.22)$$

Since the source current does not exist ($\tilde{J}_\alpha(\vec{\lambda}, y') = 0$) outside of the source region, its Fourier representation is slightly different than in (3.13), namely, the limits of integration are as follows

$$\tilde{J}_\alpha(\vec{\lambda}, \eta) = \int_{-\infty}^{\infty} \tilde{J}_\alpha(\vec{\lambda}, y') e^{-j\eta y'} dy' = \int_0^d \tilde{J}_\alpha(\vec{\lambda}, y') e^{-j\eta y'} dy' \quad (3.23)$$

where y' is used as a integration variable within the source region. Inserting (3.23) into (3.22) leaves the result

$$\tilde{\pi}_{1\alpha}^p(\vec{\lambda}, y) = \int_0^d \tilde{G}_1^p(\vec{\lambda}; y|y') \frac{\tilde{J}_\alpha(\vec{\lambda}, y')}{j\omega\epsilon_1} dy' \quad (3.24)$$

where

$$\tilde{G}_1^p(\vec{\lambda}; y|y') = \tilde{G}_1^p(\vec{\lambda}; y - y') = \frac{1}{2\pi} \int_{-\infty}^{\infty} \frac{e^{j\eta(y-y')}}{(\eta + jp_1)(\eta - jp_1)} d\eta \quad (3.25)$$

is the principal wave Hertzian-potential Green's function in the spectral domain. Using Cauchy's Integral Theorem [12], the solution to (3.25) is

$$\tilde{G}_1^p(\vec{\lambda}; y|y') = \tilde{G}_1^p(\vec{\lambda}; y - y') = \frac{e^{-p_1|y-y'|}}{2p_1} \quad (3.26)$$

Substitution of (3.26) into (3.24) leads to the principal wave contribution

$$\tilde{\pi}_{1\alpha}^p(\vec{\lambda}, y) = \int_0^d \frac{e^{-p_1|y-y'|}}{2p_1} \frac{\tilde{J}_\alpha(\vec{\lambda}, y')}{j\omega\epsilon_1} dy' \quad (3.27)$$

with y as the field point, y' as the source point, and p_1 as the y -directed propagation constant in region 1.

The scattered wave (or reflected contribution) solutions to equations (3.16) and (3.17) are well-known and are given by

$$\tilde{\pi}_{1\alpha}^r(\vec{\lambda}, y) = W_{1\alpha}^+(\vec{\lambda})e^{-p_1y} + W_{1\alpha}^-(\vec{\lambda})e^{p_1y} \quad (3.28)$$

$$\tilde{\pi}_{2\alpha}^r(\vec{\lambda}, y) = W_{2\alpha}^+(\vec{\lambda})e^{-p_2y} + W_{2\alpha}^-(\vec{\lambda})e^{p_2y} \quad (3.29)$$

where $W_{\beta\alpha}^\pm$ are the α -component spectral coefficients for the $+y$ and $-y$ directed reflected waves in region β . Thus, the total potentials in each region can be represented as

$$\tilde{\pi}_{1\alpha} = \tilde{\pi}_{1\alpha}^p + \tilde{\pi}_{1\alpha}^r = V_\alpha^+ e^{-p_1y} + W_{1\alpha}^+ e^{-p_1y} + W_{1\alpha}^- e^{p_1y} \dots y' < y < d \quad (3.30)$$

$$\tilde{\pi}_{1\alpha} = \tilde{\pi}_{1\alpha}^p + \tilde{\pi}_{1\alpha}^r = V_\alpha^- e^{p_1y} + W_{1\alpha}^+ e^{-p_1y} + W_{1\alpha}^- e^{p_1y} \dots 0 < y < y' \quad (3.31)$$

$$\tilde{\pi}_{2\alpha} = \tilde{\pi}_{2\alpha}^r = W_{2\alpha}^+ e^{-p_2y} + W_{2\alpha}^- e^{p_2y} \dots y > d \quad (3.32)$$

with $\alpha = x, y, z$ and where $p_1 = \sqrt{\lambda^2 - k_1^2}$, $p_2 = \sqrt{\lambda^2 - k_2^2}$, and

$$V_\alpha^\pm = V_\alpha^\pm(\vec{\lambda}) = \int_0^d \frac{e^{\pm p_1(\vec{\lambda})y'}}{2p_1(\vec{\lambda})} \frac{\tilde{J}_\alpha(\vec{\lambda}, y')}{j\omega\epsilon_1} dy' \quad (3.33)$$

are the $+y$ and $-y$ directed waves emanating from the source.

From equations (3.30) - (3.32), there are twelve spectral coefficients $W_{\beta\alpha}^{\pm}$ that must be determined [12]. This will be done by applying the boundary conditions for the background environment (Figure 29). Note, the boundary conditions on $\vec{\pi}$ come from the boundary conditions on \vec{E} and \vec{H} , specifically that \vec{E}_{tang} at $y = 0$ must be zero and that \vec{E}_{tang} and \vec{H}_{tang} are continuous at $y = d$. Additionally, the magnitudes of \vec{E} and \vec{H} will remain finite ($< \infty$) as $y \rightarrow \infty$. It is typically easier to satisfy the boundary conditions on $\vec{\pi}$ than on \vec{E} and \vec{H} . From Havrilla [12], the boundary conditions on $\vec{\pi}$ that ensure $\vec{E}_{\text{tang}} = 0$ at $y = 0$, continuity of \vec{E}_{tang} and \vec{H}_{tang} at $y = d$ and $\vec{E}, \vec{H} < \infty$ for $y \rightarrow \infty$ are

$$\tilde{\pi}_{2\alpha}(\lambda, y \rightarrow \infty) = 0 \quad \alpha = x, y, z \quad (3.34)$$

$$\varepsilon_1 \tilde{\pi}_{1\alpha}(\lambda, d) = \varepsilon_2 \tilde{\pi}_{2\alpha}(\lambda, d) \quad \alpha = x, z \quad (3.35)$$

$$\varepsilon_1 \frac{\partial \tilde{\pi}_{1\alpha}(\lambda, d)}{\partial y} = \varepsilon_2 \frac{\partial \tilde{\pi}_{2\alpha}(\lambda, d)}{\partial y} \quad \alpha = x, z \quad (3.36)$$

$$\varepsilon_1 \tilde{\pi}_{1y}(\lambda, d) = \varepsilon_2 \tilde{\pi}_{2y}(\lambda, d) \quad (3.37)$$

$$\frac{\partial \tilde{\pi}_{1y}(\lambda, d)}{\partial y} - \frac{\partial \tilde{\pi}_{2y}(\lambda, d)}{\partial y} = \left[1 - \frac{\varepsilon_2}{\varepsilon_1} \right] \left[j\zeta \tilde{\pi}_{2x}(\lambda, d) + j\zeta \tilde{\pi}_{2z}(\lambda, d) \right] \quad (3.38)$$

$$\tilde{\pi}_{1\alpha}(\lambda, y = 0) = 0 \quad \alpha = x, z \quad (3.39)$$

$$\frac{\partial \tilde{\pi}_{1y}(\lambda, y = 0)}{\partial y} = 0 \quad (3.40)$$

The first boundary condition relation (3.34) exists since the air layer (region 2) extends off to infinity but \vec{E} and \vec{H} remain finite, thus the potential will eventually be attenuated to zero. Continuity across the air/dielectric interface at $y = d$ leads to (3.35) and (3.36)

for tangential and (3.37) for normal components. The PEC interface at $y = 0$ will create the boundary conditions in (3.39) and (3.40). That is, at the PEC boundary, the tangential potential fields are driven to zero, as is the derivative of the normal field. Lastly, (3.38) represents the mixed/coupled boundary condition (i.e., how x and z -directed currents couple into y -directed potential). Using these boundary conditions, the spectral coefficients can now be determined.

Applying boundary condition (3.34) to (3.32) results in

$$\tilde{\pi}_{2\alpha}(\lambda, y \rightarrow \infty) = 0 \quad \alpha = x, y, z \quad (3.41)$$

$$\lim_{y \rightarrow \infty} \tilde{\pi}_{2\alpha} = \lim_{y \rightarrow \infty} (W_{2\alpha}^+ e^{-p_2 y} + W_{2\alpha}^- e^{p_2 y}) = 0 \quad (3.42)$$

$$\lim_{y \rightarrow \infty} (W_{2\alpha}^+ \cdot 0 + W_{2\alpha}^- e^{p_2 y}) = 0 \quad (3.43)$$

$$\Rightarrow W_{2\alpha}^- \equiv 0 \quad \alpha = x, y, z \quad (3.44)$$

$$\Rightarrow \tilde{\pi}_{2\alpha} = W_{2\alpha}^+ e^{-p_2 y} \quad d < y < \infty \quad (\alpha = x, y, z) \quad (3.45)$$

thus, the resultant Hertzian potential in region 2 has only a upward propagating wave associated with it. This is expected since the source is located in region 1 and region 2 extends to infinity and there will be no scattered wave in the $-y$ direction.

The next step is to apply the tangential boundary condition (3.39) at the PEC boundary ($y = 0$) to (3.31)

$$\tilde{\pi}_{1\alpha}(\lambda, y = 0) = 0 \quad \alpha = x, z \quad (3.46)$$

$$\tilde{\pi}_{1\alpha} = V_{\alpha}^- e^0 + W_{1\alpha}^+ e^0 + W_{1\alpha}^- e^0 = 0 \quad \alpha = x, z \quad (3.47)$$

$$\Rightarrow W_{1\alpha}^- = -W_{1\alpha}^+ - V_{\alpha}^- \quad \alpha = x, z \quad (3.48)$$

The tangential boundary condition (3.35) and the result from (3.45) at the air-substrate boundary ($y = d$) leads to

$$\varepsilon_1 \tilde{\pi}_{1\alpha}(\lambda, d) = \varepsilon_2 \tilde{\pi}_{2\alpha}(\lambda, d) \quad \alpha = x, z \quad (3.49)$$

$$\varepsilon_1 \left(V_\alpha^+ e^{-p_1 d} + W_{1\alpha}^+ e^{-p_1 d} + W_{1\alpha}^- e^{p_1 d} \right) = \varepsilon_2 W_{2\alpha}^+ e^{-p_2 d} \quad \alpha = x, z \quad (3.50)$$

$$\Rightarrow W_{2\alpha}^+ = \frac{\varepsilon_1}{\varepsilon_2} e^{p_2 d} \left(V_\alpha^+ e^{-p_1 d} + W_{1\alpha}^+ e^{-p_1 d} + W_{1\alpha}^- e^{p_1 d} \right) \quad \alpha = x, z \quad (3.51)$$

$$\Rightarrow \tilde{\pi}_{2\alpha} = \frac{\varepsilon_1}{\varepsilon_2} e^{-p_2(y-d)} \left(V_\alpha^+ e^{-p_1 d} + W_{1\alpha}^+ e^{-p_1 d} + W_{1\alpha}^- e^{p_1 d} \right) \quad \alpha = x, z \quad (3.52)$$

Applying the second tangential boundary condition (3.36) with the new $\tilde{\pi}_{2\alpha}$ (3.52) and the original $\tilde{\pi}_{1\alpha}$ (3.30) gives

$$\varepsilon_1 \frac{\partial \tilde{\pi}_{1\alpha}(\lambda, d)}{\partial y} = \varepsilon_2 \frac{\partial \tilde{\pi}_{2\alpha}(\lambda, d)}{\partial y} \quad \alpha = x, z \quad (3.53)$$

$$-p_1 \varepsilon_1 \left(V_\alpha^+ e^{-p_1 d} + W_{1\alpha}^+ e^{-p_1 d} - W_{1\alpha}^- e^{p_1 d} \right) = -p_2 \frac{\varepsilon_1}{\varepsilon_2} \varepsilon_2 W_{2\alpha}^+ e^{-p_2(d-d)} \left(V_\alpha^+ e^{-p_1 d} + W_{1\alpha}^+ e^{-p_1 d} + W_{1\alpha}^- e^{p_1 d} \right) \quad (3.54)$$

Solving for $W_{1\alpha}^-$ leads to

$$W_{1\alpha}^- = \frac{p_1 - p_2}{p_1 + p_2} e^{-2p_1 d} \left(V_\alpha^+ + W_{1\alpha}^+ \right) = -R e^{-2p_1 d} \left(V_\alpha^+ + W_{1\alpha}^+ \right) \quad \alpha = x, z \quad (3.55)$$

where

$$R = \frac{p_2 - p_1}{p_2 + p_1} \quad (3.56)$$

Substituting this result into (3.48) gives

$$W_{1\alpha}^+ + V_\alpha^- = R e^{-2p_1 d} \left(V_\alpha^+ + W_{1\alpha}^+ \right) \quad \alpha = x, z \quad (3.57)$$

or, solving for $W_{1\alpha}^+$, leads to

$$W_{1\alpha}^+ = \frac{Re^{-2p_1d}V_{\alpha}^+ - V_{\alpha}^-}{1 - Re^{-2p_1d}} \quad \alpha = x, z \quad (3.58)$$

Substituting (3.58) into (3.55) produces the desired result

$$W_{1\alpha}^- = \frac{-Re^{-2p_1d}V_{\alpha}^+ + Re^{-2p_1d}V_{\alpha}^-}{1 - Re^{-2p_1d}} \quad \alpha = x, z \quad (3.59)$$

The spectral coefficient $W_{2\alpha}^+$ can easily be determined by inserting (3.58) and (3.59) into (3.50).

Applying the normal boundary condition (3.37), using the equations for $\tilde{\pi}_{1y}$ and $\tilde{\pi}_{2y}$, and solving for W_{2y}^+ and, thus, $\tilde{\pi}_{2y}$ gives

$$\varepsilon_1 \tilde{\pi}_{1y}(\lambda, d) = \varepsilon_2 \tilde{\pi}_{2y}(\lambda, d) \quad (3.60)$$

$$\Rightarrow W_{2y}^+ = \frac{\varepsilon_1}{\varepsilon_2} e^{p_2d} \left(V_y^+ e^{-p_1d} + W_{1y}^+ e^{-p_1d} + W_{1y}^- e^{p_1d} \right) \quad (3.61)$$

$$\Rightarrow \tilde{\pi}_{2y} = \frac{\varepsilon_1}{\varepsilon_2} e^{-p_2(y-d)} \left(V_y^+ e^{-p_1d} + W_{1y}^+ e^{-p_1d} + W_{1y}^- e^{p_1d} \right) \quad (3.62)$$

The coupled/mixed boundary conditions can now be used to solve for the remaining two coefficients, W_{1y}^+ and W_{1y}^- . Starting with equation (3.38) and using the equation derived above for $\tilde{\pi}_{2y}$ at $y = d$ leads to

$$\frac{\partial \tilde{\pi}_{1y}(\lambda, d)}{\partial y} - \frac{\partial \tilde{\pi}_{2y}(\lambda, d)}{\partial y} = \left[1 - \frac{\varepsilon_2}{\varepsilon_1} \right] \left[j\xi \tilde{\pi}_{2x}(\lambda, d) + j\xi \tilde{\pi}_{2z}(\lambda, d) \right] \quad (3.63)$$

$$-p_2 \frac{\varepsilon_1}{\varepsilon_2} (V_y^+ e^{-p_1 d} + W_{1y}^+ e^{-p_1 d} + W_{1y}^- e^{p_1 d}) + p_1 (V_y^+ e^{-p_1 d} + W_{1y}^+ e^{-p_1 d} - W_{1y}^- e^{p_1 d}) = A \left(1 - \frac{\varepsilon_1}{\varepsilon_2} \right)$$

where (3.64)

$$A = j\xi A_x + j\zeta A_z \quad (3.65)$$

$$A_x = V_x^+ e^{-p_1 d} + W_{1x}^+ e^{-p_1 d} + W_{1x}^- e^{p_1 d} \quad (3.66)$$

$$A_z = V_z^+ e^{-p_1 d} + W_{1z}^+ e^{-p_1 d} + W_{1z}^- e^{p_1 d} \quad (3.67)$$

Solving for W_{1y}^- leads to

$$W_{1y}^- = -\bar{R}e^{-2p_1 d} V_y^+ - \bar{R}e^{-2p_1 d} W_{1y}^+ + \frac{\left(\frac{\varepsilon_1}{\varepsilon_2} - 1 \right) e^{-p_1 d} A}{\left(p_2 \frac{\varepsilon_1}{\varepsilon_2} + p_1 \right)} \quad (3.68)$$

The boundary condition (3.40) at the PEC boundary ($y = 0$) leads to

$$\frac{\partial \tilde{\pi}_{1y}(\lambda, y=0)}{\partial y} = 0 \quad (3.69)$$

$$\Rightarrow W_{1y}^- = W_{1y}^+ - V_y^- \quad (3.70)$$

Substituting equation (3.68) for W_{1y}^- gives an expression for W_{1y}^+

$$W_{1y}^+ = \frac{V_y^- - \bar{R}e^{-2p_1 d} V_y^+ + \frac{(\varepsilon_1/\varepsilon_2 - 1) e^{-p_1 d} A}{(p_2 \cdot \varepsilon_1/\varepsilon_2 + p_1)}}{(\bar{R}e^{-2p_1 d} + 1)} \quad (3.71)$$

Similarly, using equation (3.70) and the above solution leads to an expression for W_{1y}^-

$$W_{1y}^- = \frac{-\bar{R}e^{-2p_1 d} V_y^- - \bar{R}e^{-2p_1 d} V_y^+ + \frac{(\varepsilon_1/\varepsilon_2 - 1) e^{-p_1 d} A}{(p_2 \cdot \varepsilon_1/\varepsilon_2 + p_1)}}{(\bar{R}e^{-2p_1 d} + 1)} \quad (3.72)$$

The next step involves the A portions of these two equations. Since the definition of A (and subsequently A_x and A_z) includes aspects of W_{1x}^\pm and W_{1z}^\pm , these must be defined in terms of the source and not the spectral coefficients. Havrilla derives the following relationships [12]

$$W_{1y}^+ = W_{1yx}^+ + W_{1yy}^+ + W_{1yz}^+ \quad (3.73)$$

$$W_{1y}^- = W_{1yx}^- + W_{1yy}^- + W_{1yz}^- \quad (3.74)$$

where

$$W_{1yx}^+ = \frac{(N^2 - 1)e^{-p_1 d} j \xi A_x}{p_2 N^2 + p_1} = \frac{C_{yx} V_x^+ e^{-2p_1 d} - C_{yx} V_x^- e^{-2p_1 d}}{(1 + \bar{R} e^{-2p_1 d})(1 - R e^{-2p_1 d})} \quad (3.75)$$

$$W_{1yy}^+ = \frac{-\bar{R} e^{-2p_1 d} V_y^+ + V_y^-}{1 + \bar{R} e^{-2p_1 d}} \quad (3.76)$$

$$W_{1yz}^+ = \frac{(N^2 - 1)e^{-p_1 d} j \zeta A_z}{p_2 N^2 + p_1} = \frac{C_{yz} V_z^+ e^{-2p_1 d} - C_{yz} V_z^- e^{-2p_1 d}}{(1 + \bar{R} e^{-2p_1 d})(1 - R e^{-2p_1 d})} \quad (3.77)$$

$$C_{yx} = \frac{j \xi (N^2 - 1)(1 - R)}{(p_2 N^2 + p_1)} \quad (3.78)$$

$$C_{yz} = \frac{j \zeta (N^2 - 1)(1 - R)}{(p_2 N^2 + p_1)} \quad (3.79)$$

and $N^2 = \varepsilon_1 / \varepsilon_2$. Now that all of the spectral coefficients have been computed, the

Hertzian potential dyadic Green's function $\vec{\vec{G}}(\vec{r}|\vec{r}')$ can be identified.

3.2.2 Green's Function

Before \vec{E} and \vec{H} can be computed, the Hertzian Potential Green's function must be identified. The Green's function can be found from the spectral coefficients derived in the previous section. Starting with the *tangential* components of the Hertzian potential in region 1, $\tilde{\pi}_{1x}$ and $\tilde{\pi}_{1z}$, we have

$$\tilde{\pi}_{1\alpha} = \tilde{\pi}_{1\alpha}^p + \tilde{\pi}_{1\alpha}^r = V_{\alpha}^{\pm} e^{\mp p_1 y} + W_{1\alpha}^+ e^{-p_1 y} + W_{1\alpha}^- e^{p_1 y} \quad \alpha = x, z \quad (3.80)$$

$$\tilde{\pi}_{1\alpha} = \int_0^d \frac{e^{-p_1 |y-y'|}}{2p_1} \frac{\tilde{J}_{\alpha}(\vec{\lambda}, y')}{j\omega\epsilon_1} dy' + W_{1\alpha}^+ e^{-p_1 y} + W_{1\alpha}^- e^{p_1 y} \quad \alpha = x, z \quad (3.81)$$

Substituting for $W_{1\alpha}^+$ and $W_{1\alpha}^-$ gives

$$\tilde{\pi}_{1\alpha} = \int_0^d \frac{e^{-p_1 |y-y'|}}{2p_1} \frac{\tilde{J}_{\alpha}(\vec{\lambda}, y')}{j\omega\epsilon_1} dy' + \frac{Re^{-2p_1 d} V_{\alpha}^+ - V_{\alpha}^-}{1 - Re^{-2p_1 d}} e^{-p_1 y} + \frac{-Re^{-2p_1 d} V_{\alpha}^+ + Re^{-2p_1 d} V_{\alpha}^-}{1 - Re^{-2p_1 d}} e^{p_1 y} \quad (3.82)$$

Using the relationship for V_{α}^{\pm} and $\tilde{J}_{\alpha}(\vec{\lambda}, y')$ in equation (3.33), equation (3.82) can be re-written as

$$\tilde{\pi}_{1\alpha} = \int_0^d \left[\tilde{G}^p(\vec{\lambda}; y - y') + \tilde{G}_{\alpha\alpha}^r(\vec{\lambda}; y, y') \right] \frac{\tilde{J}_{\alpha}(\vec{\lambda}, y')}{j\omega\epsilon_1} dy' \quad \alpha = x, z \quad (3.83)$$

with

$$\tilde{G}^p(\vec{\lambda}; y - y') = \frac{e^{-p_1 |y-y'|}}{2p_1} \quad (3.84)$$

$$\tilde{G}_{\alpha\alpha}^r(\vec{\lambda}; y, y') = \frac{Re^{-p_1 \phi_1} - e^{-p_1 \phi_2} + Re^{-p_1 \phi_3} - Re^{-p_1 \phi_4}}{2p_1(1 - Re^{-2p_1 d})} \quad \alpha = x, z \quad (3.85)$$

$$\phi_1 = 2d + y - y' \quad \phi_2 = y + y' \quad (3.86), (3.87)$$

$$\phi_3 = 2d - y + y' \quad \phi_4 = 2d - y - y' \quad (3.88), (3.89)$$

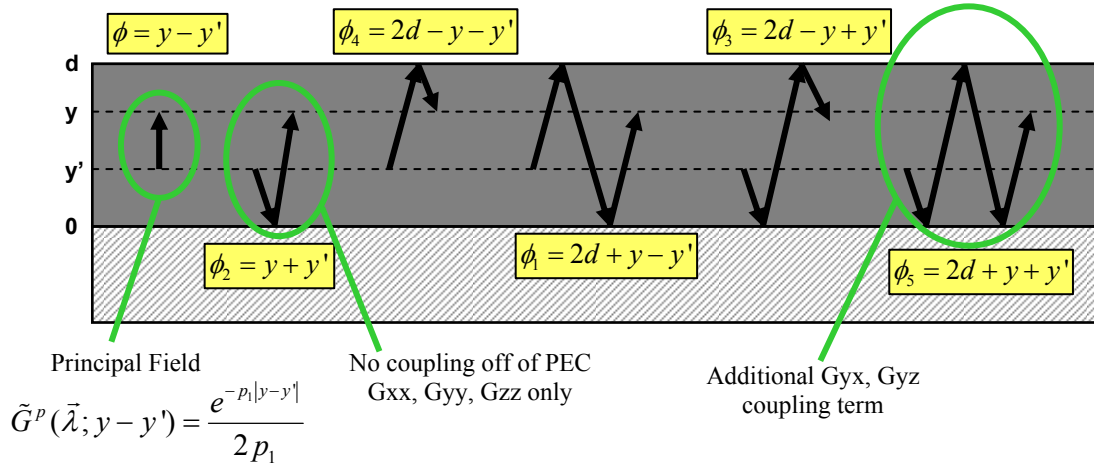


Figure 30: Source (y') and observation (y) points and paths of interaction within background environment.

An examination of these terms within the background layer shows multiple paths and contributions (see Figure 30). This figure shows the specific case where the observation point (y) is located above the source point (y'). The first path is the direct path ($y - y'$) for when $y > y'$. This path represents the principal field contribution \tilde{G}^p . The second path shown is only for the \tilde{G}_{xx} , \tilde{G}_{yy} , and \tilde{G}_{zz} contributions – no coupling will take place off of the PEC layer due to the requirement that the tangential electric fields on the PEC are zero. The last path shown ($2d + y + y'$) is included as the fourth coupling term \tilde{G}_{yx} and \tilde{G}_{yz} . An infinite number of reflections take place within the substrate region, however only four terms are necessary in the reflected fields \tilde{G}^r as all remaining reflections are accommodated within these primary terms due to the pole-series summation of these terms. This will be confirmed later in the results of this research.

An examination of the *normal* component of the Hertzian potential in Region 1

$\tilde{\pi}_{1y}$ leads to

$$\tilde{\pi}_{1y} = \tilde{\pi}_{1y}^p + \tilde{\pi}_{1y}^r = V_y^\pm e^{\mp p_1 y} + W_{1y}^+ e^{-p_1 y} + W_{1y}^- e^{p_1 y} \quad (3.90)$$

$$\begin{aligned} &= \int_0^d \left[\tilde{G}^p(\vec{\lambda}; y - y') + \tilde{G}_{yy}^r(\vec{\lambda}; y, y') \right] \frac{\tilde{J}_y(\vec{\lambda}, y')}{j\omega\epsilon_1} dy' + \\ &\int_0^d \tilde{G}_{yx}^r(\vec{\lambda}; y, y') \frac{\tilde{J}_x(\vec{\lambda}, y')}{j\omega\epsilon_1} dy' + \int_0^d \tilde{G}_{yz}^r(\vec{\lambda}; y, y') \frac{\tilde{J}_z(\vec{\lambda}, y')}{j\omega\epsilon_1} dy', \end{aligned} \quad (3.91)$$

where

$$\tilde{G}_{yy}^r(\vec{\lambda}; y, y') = \frac{-\bar{R}e^{-p_1\phi_1} + e^{-p_1\phi_2} - \bar{R}e^{-p_1\phi_3} - \bar{R}e^{-p_1\phi_4}}{2p_1(1 + \bar{R}e^{-2p_1d})} \quad (3.92)$$

$$\tilde{G}_{y\alpha}^r(\vec{\lambda}; y, y') = \frac{C_{y\alpha}^{++}e^{-p_1\phi_1} - C_{y\alpha}^{+-}e^{-p_1\phi_2} - C_{y\alpha}^{--}e^{-p_1\phi_3} + C_{y\alpha}^{-+}e^{-p_1\phi_4}}{2p_1(1 + \bar{R}e^{-2p_1d})(1 - Re^{-2p_1d})} \quad \alpha = x, z \quad (3.93)$$

and $\phi_5 = 2d + y + y'$.

Placing the above relationships for the spectral-domain Hertzian potential Green's function in dyadic form gives

$$\tilde{\tilde{G}}(\vec{\lambda}; y, y') = \tilde{\tilde{G}}^p(\vec{\lambda}; y - y') + \tilde{\tilde{G}}^r(\vec{\lambda}; y, y') \quad (3.94)$$

$$\tilde{\tilde{G}}^p(\vec{\lambda}; y - y') = \tilde{I}\tilde{G}^p = \hat{x}\tilde{G}^p\hat{x} + \hat{y}\tilde{G}^p\hat{y} + \hat{z}\tilde{G}^p\hat{z} \quad (3.95)$$

$$\tilde{\tilde{G}}^r(\vec{\lambda}; y, y') = \hat{x}\tilde{G}_{xx}^r\hat{x} + \hat{y}\tilde{G}_{yx}^r\hat{x} + \hat{y}\tilde{G}_{yy}^r\hat{y} + \hat{y}\tilde{G}_{yz}^r\hat{z} + \hat{z}\tilde{G}_{zz}^r\hat{z} \quad (3.96)$$

Note that no \tilde{G}_{xz}^r , \tilde{G}_{zx}^r , \tilde{G}_{xy}^r , or \tilde{G}_{zy}^r terms are required in the normal or tangential components of the reflected Green's functions. This is due to the properties of the interfaces at $y = 0$ and $y = d$. Coupling will only occur when an x or z -directed current

interacts with the dielectric-air boundary, which is accommodated by the \tilde{G}_{yx}^r and \tilde{G}_{yz}^r components in the reflected dyadic Green's function.

Summarizing, the Green's function is identified as

$$\tilde{G}_{\alpha\alpha}(\vec{\lambda}; y, y') = \frac{e^{-p_1|y-y'|}}{2p_1} + \frac{(p_2 - p_1)e^{-2p_1d}[e^{-p_1(y-y')} + e^{p_1(y-y')} - e^{p_1(y+y')}] - (p_2 + p_1)e^{-p_1(y+y')}}{2p_1[p_2 + p_1 - (p_2 - p_1)e^{-2p_1d}]} \quad \alpha = x, z \quad (3.97)$$

$$\tilde{G}_{yy}(\vec{\lambda}; y, y') = \frac{e^{-p_1|y-y'|}}{2p_1} + \frac{(p_2N^2 + p_1)e^{-p_1(y+y')} - (p_2N^2 - p_1)e^{-2p_1d}[e^{-p_1(y-y')} + e^{p_1(y-y')} + e^{p_1(y+y')}] }{2p_1[p_2N^2 + p_1 + (p_2N^2 - p_1)e^{-2p_1d}]} \quad (3.98)$$

$$\tilde{G}_{yx}(\vec{\lambda}; y, y') = j\xi(N^2 - 1) \frac{e^{-2p_1d}[e^{p_1(y+y')} + e^{-p_1(y-y')} - e^{p_1(y-y')} - e^{-p_1(y+y')}] }{[p_2N^2 + p_1 + (p_2N^2 - p_1)e^{-2p_1d}][p_2 + p_1 - (p_2 - p_1)e^{-2p_1d}]} \quad (3.99)$$

$$\tilde{G}_{yz}(\vec{\lambda}; y, y') = j\zeta(N^2 - 1) \frac{e^{-2p_1d}[e^{p_1(y+y')} + e^{-p_1(y-y')} - e^{p_1(y-y')} - e^{-p_1(y+y')}] }{[p_2N^2 + p_1 + (p_2N^2 - p_1)e^{-2p_1d}][p_2 + p_1 - (p_2 - p_1)e^{-2p_1d}]} \quad (3.100)$$

Note, since $\tilde{G}_{\alpha\alpha}^p$ contains the absolute value $|y - y'|$, integrals or derivatives operating on this term must be handled carefully (it is this term located in the volume of interest that is crucial in the analysis of the modified leaky-wave antenna investigated in this research). This will be addressed in the following chapter.

Now that the Green's function for the microstrip background structure has been identified, it can be used to develop the coupled Electric Field Integral Equation formulation for the modified THW antenna structure. The EFIEs can then be solved using the Method of Moments to find the propagation constants for the modified antenna structure, as discussed in the next chapter.

Chapter 4

ELECTRIC FIELD INTEGRAL EQUATION FORMULATION AND METHOD OF MOMENTS SOLUTION

4.1 Introduction

For the modified traveling-wave microstrip antenna under investigation (see Figure 31), two currents will exist: one on the surface of the PEC strip conductor \vec{J}_s and one within the volume under the strip $\vec{J}_v = j\omega(\epsilon_3 - \epsilon_1)\vec{E}$. Since both of these currents are immersed in region 1 of the grounded slab background environment (see Chapter 3, Figure 29), the Green's function derived in the previous chapter can be used to represent the scattered fields maintained by these currents.

This chapter will demonstrate how these scattered fields are used to develop a coupled Electric Field Integral Equation (EFIE) formulation for the unknown currents \vec{J}_s and \vec{J}_v and subsequently solved via the Method of Moments (MoM). From the MoM solution, the desired propagation characteristics can be computed for the baseline antenna (strip conductor only), as well as for the modified microstrip structure.

It is important to note that although the THW antenna is under investigation, the full-width antenna shown in Figure 31 will be analyzed in this and subsequent chapters. This is due to the ease of modeling the full-width antenna and its associated boundary conditions as compared to the relative difficulty required to apply the boundary

conditions (specifically, the vertical shunt) to the half-width antenna. Zelinski showed that for the odd-numbered higher-order modes of operation, there was no difference between the results for the half-width versus the full-width antenna [5]. Given that this research is focused on finding the propagation characteristics of the first higher-order mode (i.e., the EH_1 mode) for the antenna structure, the results for the full-width antenna will be the same as the half-width antenna in this mode. Additionally, it will be shown later in this chapter how the basis functions used to represent the strip currents and electric fields are chosen such that they will drive the solution to an odd-numbered higher-order mode. The desired EH_1 mode will therefore be the lowest-order odd mode. Thus, due to the proper choice of basis functions, the shunt is not required for the full-wave analysis.

Note, however, the physical implementation of the antenna requires the shunt to be present in order to block the dominant mode, and subsequent even higher order modes, so that the antenna can operate as a leaky-wave antenna. The fact that the shunt maintains odd-mode purity is important in the integral equation development as it allows a natural-mode current solution to be sought (since we are interested here in only the propagation characteristics, a forced solution is not necessary due to this mode purity).

Finally, it is important to mention that the length of the modified antenna modeled in this chapter is assumed to be infinite in extent along the guiding axis in order to simplify the analytical development. Although the actual THW antenna is finite in length, its leaky-wave behavior effectively supports a forward traveling wave only (with minimal terminal reflection), thus appearing as though it were infinite in length.

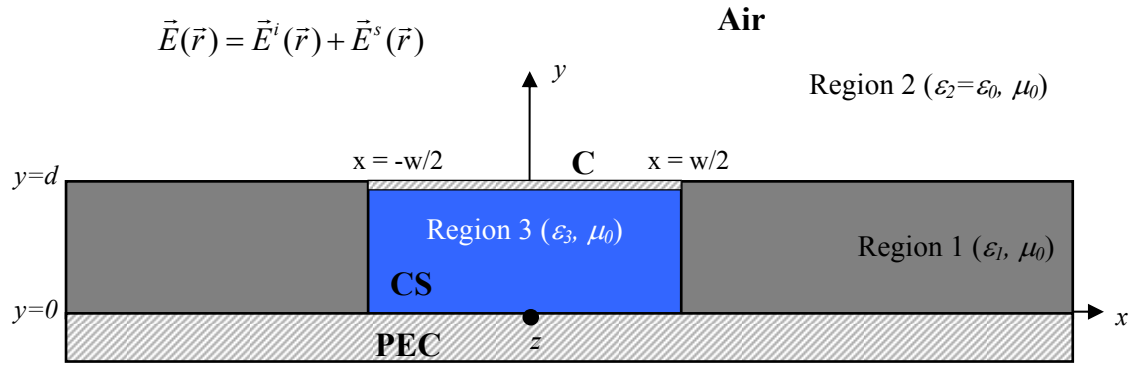


Figure 31: Cross-sectional view of the modified full-width leaky-wave microstrip antenna.

4.2 Electric Field Integral Equation Formulation

The Green's function for the background environment was derived in the previous chapter. This expression can be used to find the scattered electric field within the specific region of interest which, when inserted into the coupled EFIEs, can be solved using the MoM technique and the specific propagation characteristics of the antenna can be found.

Figure 31 shows the modified leaky-wave microstrip antenna. The infinitesimally-thin PEC strip conductor supporting surface current \vec{J}_S is assumed to be infinite in extent along the guiding axis (i.e., the z -axis) and located at $y=d$ (rigorously, $y=d^-$). The region 3 material supporting volume current \vec{J}_V is also assumed to be infinite in extent along the guiding axis and has cross-sectional dimensions $-\frac{W}{2} < x < \frac{W}{2}, 0 < y < d$. The total electric field at any location is comprised of two components: the *impressed* field and the *scattered* field, and can be written as

$$\vec{E}(\vec{r}) = \vec{E}^i(\vec{r}) + \vec{E}^s(\vec{r}) \quad (4.1)$$

or in the ζ – domain (transform on z prompted by the infinite guiding length) as

$$\vec{\tilde{E}}(\vec{\rho}, \zeta) = \vec{\tilde{E}}^i(\vec{\rho}, \zeta) + \vec{\tilde{E}}^s(\vec{\rho}, \zeta). \quad (4.2)$$

where $\vec{\rho} = \hat{x}x + \hat{y}y$. This fundamental field relation is utilized in the coupled EFIE formulation in the following manner described next.

In order to ensure uniqueness, appropriate boundary conditions for the modified structure must be satisfied. The boundary conditions of the background environment are naturally satisfied since they are built into the Green's function development of Chapter 3. The remaining boundary/field conditions that require enforcement are at the surface of the strip conductor (surface contour C) and within region 3 (cross section CS), namely

$$\hat{t} \cdot \vec{\tilde{E}}(\vec{\rho}, \zeta) = 0 \quad \dots \text{for } \vec{\rho} \in C; \hat{t} = \hat{x}, \hat{z} \quad (4.3)$$

$$\vec{\tilde{E}}(\vec{\rho}, \zeta) = \vec{\tilde{E}}^i(\vec{\rho}, \zeta) + \vec{\tilde{E}}^s(\vec{\rho}, \zeta) \quad \dots \text{for } \vec{\rho} \in CS. \quad (4.4)$$

The spectral-domain boundary condition in equation (4.3) states that the total tangential electric field must be zero at the surface of the strip conductor. Equation (4.4) is the relation that must exist on the total electric field within region 3. With the aid of equation (4.2), the above boundary condition relations can be written as

$$\hat{t} \cdot \vec{\tilde{E}}^s(\vec{\rho}, \zeta) = -\hat{t} \cdot \vec{\tilde{E}}^i(\vec{\rho}, \zeta) \quad \dots \text{for } \vec{\rho} \in C; \hat{t} = \hat{x}, \hat{z} \quad (4.5)$$

$$\vec{\tilde{E}}^s(\vec{\rho}, \zeta) - \vec{\tilde{E}}^i(\vec{\rho}, \zeta) = -\vec{\tilde{E}}^i(\vec{\rho}, \zeta) \quad \dots \text{for } \vec{\rho} \in CS. \quad (4.6)$$

These two boundary condition relations form the basis of the coupled EFIEs. To complete the EFIE development, an expression for $\vec{\tilde{E}}^s(\vec{\rho}, \zeta)$ must be found and is discussed next.

The spatial-domain scattered electric field in region 1 can be written in terms of the Hertzian potential using equation (2.45)

$$\vec{E}^s(\vec{\rho}, z) = (k_1^2 + \nabla \nabla \cdot) \vec{\pi}_1(\vec{\rho}, z). \quad (4.7)$$

Upon Fourier transformation of equation (4.7), the scattered field in the ζ -domain becomes

$$\vec{E}^s(\vec{\rho}, \zeta) = (k_1^2 + \tilde{\nabla} \tilde{\nabla} \cdot) \vec{\pi}_1(\vec{\rho}, \zeta) \quad (4.8)$$

where $\tilde{\nabla} = \hat{x} \frac{\partial}{\partial x} + \hat{y} \frac{\partial}{\partial y} + \hat{z} j\zeta$. Note, the term $j\zeta$ results from application of the Fourier differentiation theorem.

The Hertzian potential $\vec{\pi}_1(\vec{\rho}, \zeta)$ can be found from $\vec{\tilde{\pi}}_1(\xi, y, \zeta)$ derived in Chapter 3 using an inverse transform in ξ , namely

$$\vec{\pi}_1(\vec{\rho}, \zeta) = \frac{1}{2\pi} \int_{-\infty}^{\infty} \vec{\tilde{\pi}}_1(\xi, y, \zeta) e^{j\xi x} d\xi \quad (4.9)$$

From the previous chapter, it was shown that the Hertzian potential $\vec{\tilde{\pi}}_1(\xi, y, \zeta)$ can be expressed as (using the Green's functions derived in Chapter 3 and the total current)

$$\vec{\tilde{\pi}}_1(\xi, y, \zeta) = \int_0^d \frac{\vec{\tilde{G}}_1(y|y'; \xi, \zeta)}{j\omega\epsilon_1} \cdot \vec{\tilde{J}}(\xi, y', \zeta) dy' \quad (4.10)$$

Recall, the current is decomposed into two components, the surface conduction current on the top conductor and the volume polarization current in region 3, thus

$$\vec{\tilde{J}}(\xi, y', \zeta) = \vec{\tilde{J}}_c(\xi, y', \zeta) + \vec{\tilde{J}}_v(\xi, y', \zeta) \quad (4.11)$$

Since boundary conditions must be applied in the x, y - domain, and the currents exist on the strip conductor and within region 3, it is necessary to represent $\tilde{\tilde{J}}(\xi, y', \zeta)$ in terms of $\tilde{J}(x', y', \zeta)$ using the inverse transform relation, that is

$$\tilde{\tilde{J}}(\xi, y', \zeta) = \int_{-W/2}^{W/2} \left(\tilde{J}_C(x', y', \zeta) + \tilde{J}_V(x', y', \zeta) \right) e^{-j\xi x'} dx' \quad (4.12)$$

within Region 3. Substituting (4.12) into (4.10) and the resultant into (4.9) leads to

$$\tilde{\pi}_1(\vec{\rho}, \zeta) = \frac{1}{2\pi} \int_{-\infty}^{\infty} \left\{ \int_0^d \frac{\tilde{\tilde{G}}_1(y | y', \xi, \zeta)}{j\omega\epsilon_1} \cdot \left[\int_{-W/2}^{W/2} \left(\tilde{J}_C(x', y', \zeta) + \tilde{J}_V(x', y', \zeta) \right) e^{-j\xi x'} dx' \right] dy' \right\} e^{j\xi x} d\xi \quad (4.13)$$

Interchanging limits of integration gives

$$\tilde{\pi}_1(\vec{\rho}, \zeta) = \frac{1}{2\pi} \int_{-\infty}^{\infty} \int_0^d \int_{-W/2}^{W/2} \frac{\tilde{\tilde{G}}_1(y | y', \xi, \zeta)}{j\omega\epsilon_1} e^{j\xi(x-x')} \cdot \left(\tilde{J}_C(x', y', \zeta) + \tilde{J}_V(x', y', \zeta) \right) dx' dy' d\xi \quad (4.14)$$

and upon substitution into (4.7) produces the desired expression for the scattered field

$$\vec{E}^s(\vec{\rho}, \zeta) = \left(k_1^2 + \tilde{\nabla} \tilde{\nabla} \cdot \right) \int_{-\infty}^{\infty} \int_0^d \int_{-W/2}^{W/2} \frac{\tilde{\tilde{G}}_1(y | y', \xi, \zeta)}{2\pi j\omega\epsilon_1} e^{j\xi(x-x')} \cdot \left(\tilde{J}_C(x', y', \zeta) + \tilde{J}_V(x', y', \zeta) \right) dx' dy' d\xi \quad (4.15)$$

As a final step, the volume current density $\tilde{\tilde{J}}_V$ is related to the total electric field (using volume equivalence) by the relation $\tilde{\tilde{J}}_V = j\omega(\epsilon_3 - \epsilon_1)\vec{\tilde{E}}$. Thus, upon rearranging this volume current relation, the electric field $\vec{\tilde{E}}$ can be written as

$$\vec{E}(\vec{\rho}, \zeta) = \frac{\vec{J}_V(\vec{\rho}, \zeta)}{j\omega(\varepsilon_3 - \varepsilon_1)} \quad (4.16)$$

provided $\varepsilon_3 \neq \varepsilon_1$. In addition, the strip conduction surface current density can be represented using the relation

$$\vec{J}_C(x', y', \zeta) = \vec{J}_S(x', \zeta) \delta(y' - d) \quad (4.17)$$

Therefore, using the relations (4.15)-(4.17) in equations (4.5) and (4.6) leads to the desired coupled EFIEs for the unknown spectral-domain current densities \vec{J}_S and \vec{J}_V

$$\begin{aligned} & \frac{\hat{t} \cdot (k_1^2 + \tilde{\nabla} \tilde{\nabla} \cdot)}{2\pi j\omega\varepsilon_1} \int_{-\infty}^{\infty} \left[\int_{-W/2}^{W/2} \tilde{G}_1(y|d; \xi, \zeta) e^{j\xi(x-x')} \cdot \vec{J}_S(x', \zeta) dx' \right. \\ & \left. + \int_0^d \int_{-W/2}^{W/2} \tilde{G}_1(y|y'; \xi, \zeta) e^{j\xi(x-x')} \cdot \vec{J}_V(x', y', \zeta) dx' dy' \right] d\xi = -\hat{t} \cdot \vec{E}^i(\vec{\rho}, \zeta) \dots \text{for } \vec{\rho} \in C; \hat{t} = \hat{x}, \hat{z} \end{aligned} \quad (4.18)$$

$$\begin{aligned} & \frac{(k_1^2 + \tilde{\nabla} \tilde{\nabla} \cdot)}{2\pi j\omega\varepsilon_1} \int_{-\infty}^{\infty} \left[\int_{-W/2}^{W/2} \tilde{G}_1(y|d; \xi, \zeta) e^{j\xi(x-x')} \cdot \vec{J}_S(x', \zeta) dx' \right. \\ & \left. + \int_0^d \int_{-W/2}^{W/2} \tilde{G}_1(y|y'; \xi, \zeta) e^{j\xi(x-x')} \cdot \vec{J}_V(x', y', \zeta) dx' dy' \right] d\xi - \frac{\vec{J}_V(\vec{\rho}, \zeta)}{j\omega(\varepsilon_3 - \varepsilon_1)} = -\vec{E}^i(\vec{\rho}, \zeta) \dots \text{for } \vec{\rho} \in CS \end{aligned} \quad (4.19)$$

Note, the baseline antenna involving the strip conductor only can easily be analyzed based on equation (4.18) alone since the volume current density vanishes when $\varepsilon_3 = \varepsilon_1$.

As mentioned previously, we are only interested in the propagation constant ζ in this study, thus we are not interested in how the fields are ultimately related to the source strength. In addition, it is assumed that the excitation of the leaky-wave antenna leads to a very pure modal response (i.e., a nearly pure EH_1 mode response for the THW

antenna). Consequently, it is therefore sufficient to seek a natural-mode (i.e., eigenmode) current solution to the above coupled integral equations, which is developed next.

4.2.1 Eigenmode Current

In general, the response to an arbitrary excitation will result in a superposition of natural modes (i.e., eigenmodes) whose complex amplitude coefficients are related to the strength of the impressed source. However, due to the THW shunt design, the mode purity is very high. Thus, we anticipate a single mode (the EH_1 mode in this research) to be a very good model of the currents excited on the THW antenna. Since we are primarily only interested in the field distribution $e^{-j\zeta z}$ (i.e., $\zeta = \beta - j\alpha$) and not on how the field strength is related to the impressed source strength, we can formulate the integral equation for natural mode currents; that is, we are only interested in solving homogeneous and unforced coupled integral equations. The unforced coupled EFIEs can be developed as a special case of equations (4.18) - (4.19) and is discussed next.

If we let ζ_p represent the p^{th} natural mode propagation constant, the anticipated spatial field distribution is $e^{\mp j\zeta_p z}$ for a forward/reverse traveling wave, respectively. In the spectral domain (i.e., the ζ - domain), this exponential function manifests itself as a pole singularity of the form $1/(\zeta \pm \zeta_p)$. Thus, a spectral-domain current density behavior near an eigenmode can be represented as [12]

$$\tilde{\tilde{J}}(\vec{\rho}, \zeta) \cong \frac{\tilde{\tilde{J}}_p(\vec{\rho})}{\zeta \pm \zeta_p} \quad (4.20)$$

where $\tilde{\tilde{J}}_p$ is the eigenmode current associated with the p^{th} discrete natural mode.

Substituting (4.20) into (4.18) and (4.19) and multiplying through by $\zeta \pm \zeta_p$ produces

$$\begin{aligned} & \frac{\hat{t} \cdot (k_1^2 + \tilde{\nabla} \tilde{\nabla} \cdot)}{2\pi j\omega\epsilon_1} \int_{-\infty}^{\infty} \left[\int_{-W/2}^{W/2} \tilde{\tilde{G}}_1(y|d; \xi, \zeta) e^{j\xi(x-x')} \cdot \tilde{\tilde{J}}_{pS}(x', \zeta) dx' \right. \\ & \left. + \int_0^d \int_{-W/2}^{W/2} \tilde{\tilde{G}}_1(y|y'; \xi, \zeta) e^{j\xi(x-x')} \cdot \tilde{\tilde{J}}_{pV}(x', y', \zeta) dx' dy' \right] d\xi = -(\zeta \pm \zeta_p) \hat{t} \cdot \tilde{\tilde{E}}^i(\vec{\rho}, \zeta) \end{aligned} \quad (4.21)$$

$$\begin{aligned} & \frac{(k_1^2 + \tilde{\nabla} \tilde{\nabla} \cdot)}{2\pi j\omega\epsilon_1} \int_{-\infty}^{\infty} \left[\int_{-W/2}^{W/2} \tilde{\tilde{G}}_1(y|d; \xi, \zeta) e^{j\xi(x-x')} \cdot \tilde{\tilde{J}}_{pS}(x', \zeta) dx' \right. \\ & \left. + \int_0^d \int_{-W/2}^{W/2} \tilde{\tilde{G}}_1(y|y'; \xi, \zeta) e^{j\xi(x-x')} \cdot \tilde{\tilde{J}}_{pV}(x', y', \zeta) dx' dy' \right] d\xi - \frac{\tilde{\tilde{J}}_{pV}(\vec{\rho}, \zeta)}{j\omega(\epsilon_3 - \epsilon_1)} = -(\zeta \pm \zeta_p) \tilde{\tilde{E}}^i(\vec{\rho}, \zeta) \end{aligned} \quad (4.22)$$

Now, the impressed field $\tilde{\tilde{E}}^i$ is not influenced by the structure it is inserted into, similar to an ideal battery being inserted into a circuit. Thus, $\tilde{\tilde{E}}^i$ must be analytic near the guiding-structure poles $\zeta = \mp \zeta_p$. Therefore, in the limit as $\zeta \rightarrow \mp \zeta_p$, (4.21) and (4.22) reduce to the unforced coupled EFIEs

$$\begin{aligned} & \frac{\hat{t} \cdot (k_1^2 + \tilde{\nabla} \tilde{\nabla} \cdot)}{2\pi j\omega\epsilon_1} \int_{-\infty}^{\infty} \left[\int_{-W/2}^{W/2} \tilde{\tilde{G}}_1(y|d; \xi, \zeta) e^{j\xi(x-x')} \cdot \tilde{\tilde{J}}_S(x', \zeta) dx' \right. \\ & \left. + \int_0^d \int_{-W/2}^{W/2} \tilde{\tilde{G}}_1(y|y'; \xi, \zeta) e^{j\xi(x-x')} \cdot \tilde{\tilde{J}}_V(x', y', \zeta) dx' dy' \right] d\xi = 0 \quad \dots \text{for } \vec{\rho} \in C; \hat{t} = \hat{x}, \hat{z} \end{aligned} \quad (4.23)$$

$$\begin{aligned} & \frac{(k_1^2 + \tilde{\nabla} \tilde{\nabla} \cdot)}{2\pi j\omega\epsilon_1} \int_{-\infty}^{\infty} \left[\int_{-W/2}^{W/2} \tilde{\tilde{G}}_1(y|d; \xi, \zeta) e^{j\xi(x-x')} \cdot \tilde{\tilde{J}}_S(x', \zeta) dx' \right. \\ & \left. + \int_0^d \int_{-W/2}^{W/2} \tilde{\tilde{G}}_1(y|y'; \xi, \zeta) e^{j\xi(x-x')} \cdot \tilde{\tilde{J}}_V(x', y', \zeta) dx' dy' \right] d\xi - \frac{\tilde{\tilde{J}}_V(\vec{\rho}, \zeta)}{j\omega(\epsilon_3 - \epsilon_1)} = 0 \quad \dots \vec{\rho} \in CS \end{aligned} \quad (4.24)$$

since $\lim_{\zeta \rightarrow \mp \zeta_p} (\zeta \pm \zeta_p) \tilde{\tilde{E}}^i(\vec{\rho}, \zeta) = 0$. Note, the subscript p has been dropped from ζ and the eigenmode current terms in equations (4.23) and (4.24) for notational convenience. Finally, due to the presence of the $\varepsilon_3 - \varepsilon_1$ in the denominator of (4.24), it is better (from a numerical stability viewpoint), to utilize the relation $\tilde{\tilde{J}}_V = j\omega(\varepsilon_3 - \varepsilon_1) \tilde{\tilde{E}}$ in both equations (4.22) and (4.23), leading to the desired unforced coupled EFIEs

$$\begin{aligned} & \frac{\hat{t} \cdot (k_1^2 + \tilde{\nabla} \tilde{\nabla} \cdot)}{2\pi} \int_{-\infty}^{\infty} \left[\int_{-W/2}^{W/2} \tilde{\tilde{G}}_1(y | d; \xi, \zeta) e^{j\xi(x-x')} \cdot \frac{\tilde{\tilde{J}}_S(x', \zeta)}{j\omega\varepsilon_1} dx' \right. \\ & \left. + \int_0^d \int_{-W/2}^{W/2} \tilde{\tilde{G}}_1(y | y'; \xi, \zeta) e^{j\xi(x-x')} \cdot \frac{(\varepsilon_3 - \varepsilon_1)}{\varepsilon_1} \tilde{\tilde{E}}(x', y', \zeta) dx' dy' \right] d\xi = 0 \quad \dots \text{for } \vec{\rho} \in C; \hat{t} = \hat{x}, \hat{z} \end{aligned} \quad (4.23)$$

$$\begin{aligned} & \frac{(k_1^2 + \tilde{\nabla} \tilde{\nabla} \cdot)}{2\pi} \int_{-\infty}^{\infty} \left[\int_{-W/2}^{W/2} \tilde{\tilde{G}}_1(y | d; \xi, \zeta) e^{j\xi(x-x')} \cdot \frac{\tilde{\tilde{J}}_S(x', \zeta)}{j\omega\varepsilon_1} dx' \right. \\ & \left. + \int_0^d \int_{-W/2}^{W/2} \tilde{\tilde{G}}_1(y | y'; \xi, \zeta) e^{j\xi(x-x')} \cdot \frac{(\varepsilon_3 - \varepsilon_1)}{\varepsilon_1} \tilde{\tilde{E}}(x', y', \zeta) dx' dy' \right] d\xi - \tilde{\tilde{E}}(x', y', \zeta) = 0 \quad \dots \vec{\rho} \in CS \end{aligned} \quad (4.24)$$

Note, since the boundary condition in (4.23) must be enforced at $\vec{\rho} \in C$, this integral equation must be evaluated in the limit as $y \rightarrow d$. Next, the components of the dyadic Green's function, surface current density and electric field will be substituted into (4.23) and (4.24) to complete the unforced coupled EFIEs formulation.

4.2.2 Insertion of Green's Function into EFIEs

The scalar components of the coupled EFIEs can be identified by inserting the expression for the dyadic Green's function, surface current density and electric field into (4.23) and (4.24). From (3.94) to (3.96), the total Green's function can be written as

$$\tilde{\tilde{G}}(\vec{\lambda}; y, y') = \hat{x}(\tilde{\tilde{G}}^p + \tilde{\tilde{G}}_{xx}^r)\hat{x} + \hat{y}\tilde{\tilde{G}}_{yx}^r\hat{x} + \hat{y}(\tilde{\tilde{G}}^p + \tilde{\tilde{G}}_{yy}^r)\hat{y} + \hat{y}\tilde{\tilde{G}}_{yz}^r\hat{z} + \hat{z}(\tilde{\tilde{G}}^p + \tilde{\tilde{G}}_{zz}^r)\hat{z} \quad (4.25)$$

Combining the principal and the reflected terms into a total Green's function term gives

$$\tilde{\tilde{G}}(\vec{\lambda}; y, y') = \hat{x}\tilde{\tilde{G}}_{xx}\hat{x} + \hat{y}\tilde{\tilde{G}}_{yx}\hat{x} + \hat{y}\tilde{\tilde{G}}_{yy}\hat{y} + \hat{y}\tilde{\tilde{G}}_{yz}\hat{z} + \hat{z}\tilde{\tilde{G}}_{zz}\hat{z} \quad (4.26)$$

where the $\tilde{\tilde{G}}_{xx}$, $\tilde{\tilde{G}}_{yy}$, and $\tilde{\tilde{G}}_{zz}$ terms contain both the principal and reflected field contributions of the Green's function.

The surface current on the top conductor $\tilde{\tilde{J}}_s$ and the electric field $\tilde{\tilde{E}}$ within the volume of region 3 can be written as

$$\tilde{\tilde{J}}_s(x', \zeta) = \hat{x}\tilde{\tilde{J}}_x(x', \zeta) + \hat{z}\tilde{\tilde{J}}_z(x', \zeta) \quad (4.27)$$

$$\tilde{\tilde{E}}(x', y', \zeta) = \hat{x}\tilde{\tilde{E}}_x(x', y', \zeta) + \hat{y}\tilde{\tilde{E}}_y(x', y', \zeta) + \hat{z}\tilde{\tilde{E}}_z(x', y', \zeta) \quad (4.28)$$

thus, giving the following relations

$$\tilde{\tilde{G}}(\vec{\lambda}; y | d) \cdot \tilde{\tilde{J}}_s(x', \zeta) = \hat{x}\tilde{\tilde{G}}_{xx}\tilde{\tilde{J}}_x + \hat{y}\tilde{\tilde{G}}_{yx}\tilde{\tilde{J}}_x + \hat{y}\tilde{\tilde{G}}_{yz}\tilde{\tilde{J}}_z + \hat{z}\tilde{\tilde{G}}_{zz}\tilde{\tilde{J}}_z \quad (4.29)$$

$$\tilde{\tilde{G}}(\vec{\lambda}; y, y') \cdot \tilde{\tilde{E}}(x', y', \zeta) = \hat{x}\tilde{\tilde{G}}_{xx}\tilde{\tilde{E}}_x + \hat{y}\tilde{\tilde{G}}_{yx}\tilde{\tilde{E}}_x + \hat{y}\tilde{\tilde{G}}_{yy}\tilde{\tilde{E}}_y + \hat{y}\tilde{\tilde{G}}_{yz}\tilde{\tilde{E}}_z + \hat{z}\tilde{\tilde{G}}_{zz}\tilde{\tilde{E}}_z \quad (4.30)$$

which allows (4.23) and (4.24) to be written as

$$\begin{aligned}
& \lim_{y \rightarrow d} \hat{t} \cdot \frac{(k_1^2 + \tilde{\nabla} \tilde{\nabla} \cdot)}{2\pi} \int_{-\infty}^{\infty} \left[\int_{-W/2}^{W/2} \left(\hat{x} \tilde{G}_{xx} \tilde{J}_x + \hat{y} \tilde{G}_{yx} \tilde{J}_x + \hat{y} \tilde{G}_{yz} \tilde{J}_z + \hat{z} \tilde{G}_{zz} \tilde{J}_z \right) \frac{e^{j\xi(x-x')}}{j\omega\epsilon_1} dx' \right. \\
& \left. + \int_0^d \int_{-W/2}^{W/2} \left(\hat{x} \tilde{G}_{xx} \tilde{E}_x + \hat{y} \tilde{G}_{yx} \tilde{E}_x + \hat{y} \tilde{G}_{yy} \tilde{E}_y + \hat{y} \tilde{G}_{yz} \tilde{E}_z + \hat{z} \tilde{G}_{zz} \tilde{E}_z \right) \frac{(\epsilon_3 - \epsilon_1)}{\epsilon_1} e^{j\xi(x-x')} dx' dy' \right] d\xi = 0
\end{aligned} \tag{4.31}$$

$$\begin{aligned}
& \frac{(k_1^2 + \tilde{\nabla} \tilde{\nabla} \cdot)}{2\pi} \int_{-\infty}^{\infty} \left[\int_{-W/2}^{W/2} \left(\hat{x} \tilde{G}_{xx} \tilde{J}_x + \hat{y} \tilde{G}_{yx} \tilde{J}_x + \hat{y} \tilde{G}_{yz} \tilde{J}_z + \hat{z} \tilde{G}_{zz} \tilde{J}_z \right) \frac{e^{j\xi(x-x')}}{j\omega\epsilon_1} dx' \right. \\
& \left. + \int_0^d \int_{-W/2}^{W/2} \left(\hat{x} \tilde{G}_{xx} \tilde{E}_x + \hat{y} \tilde{G}_{yx} \tilde{E}_x + \hat{y} \tilde{G}_{yy} \tilde{E}_y + \hat{y} \tilde{G}_{yz} \tilde{E}_z + \hat{z} \tilde{G}_{zz} \tilde{E}_z \right) \frac{(\epsilon_3 - \epsilon_1)}{\epsilon_1} e^{j\xi(x-x')} dx' dy' \right] d\xi \tag{4.32} \\
& - \hat{x} \tilde{E}_x(x, y, \zeta) - \hat{y} \tilde{E}_y(x, y, \zeta) - \hat{z} \tilde{E}_z(x, y, \zeta) = 0
\end{aligned}$$

Before the $k_1^2 + \tilde{\nabla} \tilde{\nabla} \cdot$ operator can be brought inside the integrals, the principal field portions (3.84) of the Green's function must be considered. The absolute value term $|y - y'|$ in (3.84) causes a discontinuity at $y = y'$, thus any integration with respect to y' must be split into two integrals – one integral from 0 to y and the other from y to d . Thus, for only the terms containing the principal field (\tilde{G}_{xx}^p , \tilde{G}_{yy}^p , and \tilde{G}_{zz}^p)

$$\int_0^d \frac{e^{-p_1|y-y'|}}{2p_1} dy' = \lim_{\delta \rightarrow 0^+} \left[\int_0^{y-\delta} \frac{e^{p_1(y-y')}}{2p_1} dy' + \int_{y+\delta}^d \frac{e^{-p_1(y-y')}}{2p_1} dy' \right] = PV \int_0^d \frac{e^{-p_1|y-y'|}}{2p_1} dy' \tag{4.33}$$

where the PV notation indicates that the integral is evaluated in a Cauchy Principle Value sense.

Upon using Leibnitz's rule of differentiation, the x and z differentiation operators can freely pass through the integral as well as the $\partial/\partial y$ operator. However, the operator $\partial^2/\partial y^2$ will not freely pass through due to the y -dependent limits of integration in (4.33). Havrilla [12] showed that applying the $\partial^2/\partial y^2$ operator to (4.33) results in

$$\frac{\partial^2}{\partial y^2} \int_{-\frac{w}{2}}^{\frac{w}{2}} \int_0^d \frac{e^{-p_1|y-y'|}}{2p_1} dy' dx' = \int_{-\frac{w}{2}}^{\frac{w}{2}} \int_0^d \left[\frac{\partial^2}{\partial y^2} \frac{e^{-p_1|y-y'|}}{2p_1} - \delta(\bar{\rho} - \bar{\rho}') \right] dy' dx' \quad (4.34)$$

Examination of (4.31) and (4.32) reveals that the $\partial^2/\partial y^2$ operator will only be present for the term \tilde{G}_{yy} , with $\bar{\rho} = \bar{\rho}'$ leading to the extra contribution in (4.34).

Additionally, the $\partial/\partial x$ differentiation will only apply to the $\exp(j\xi(x-x'))$ term resulting in the factor $j\xi$, thus the operator $k_1^2 + \tilde{\nabla}\tilde{\nabla} \cdot$ can be represented as

$$k_1^2 + \left(j\xi \hat{x} + \frac{\partial}{\partial y} \hat{y} + j\zeta \hat{z} \right) \left(j\xi \hat{x} + \frac{\partial}{\partial y} \hat{y} + j\zeta \hat{z} \right). \quad (4.35)$$

Applying (4.35) to (4.31) and (4.32) results in

$$\begin{aligned} & \lim_{y' \rightarrow d} \hat{t} \cdot \left\{ \int_{-\infty}^{\infty} \left[\int_{-W/2}^{W/2} \left\{ \hat{x} \left[(k^2 - \xi^2) \tilde{G}_{xx} \tilde{J}_x + j\xi \frac{\partial}{\partial y} \left(\tilde{G}_{yx} \tilde{J}_x + \tilde{G}_{yz} \tilde{J}_z \right) - \xi\zeta \tilde{G}_{zz} \tilde{J}_z \right] \right. \right. \right. \\ & \quad + \hat{y} \left[\left(k^2 + \frac{\partial^2}{\partial y^2} \right) \left(\tilde{G}_{yx} \tilde{J}_x + \tilde{G}_{yz} \tilde{J}_z \right) + j\xi \frac{\partial}{\partial y} \tilde{G}_{xx} \tilde{J}_x + j\zeta \frac{\partial}{\partial y} \tilde{G}_{zz} \tilde{J}_z \right] \\ & \quad \left. \left. + \hat{z} \left[(k^2 - \zeta^2) \tilde{G}_{zz} \tilde{J}_z + j\zeta \frac{\partial}{\partial y} \left(\tilde{G}_{yx} \tilde{J}_x + \tilde{G}_{yz} \tilde{J}_z \right) - \xi\zeta \tilde{G}_{xx} \tilde{J}_x \right] \right\} \frac{e^{j\xi(x-x')}}{2\pi j\omega\epsilon_1} dx' \right. \\ & \quad + \int_0^d \int_{-W/2}^{W/2} \frac{(\epsilon_3 - \epsilon_1)}{2\pi\epsilon_1} \left\{ \hat{x} \left[(k^2 - \xi^2) \tilde{G}_{xx} \tilde{E}_x + j\xi \frac{\partial}{\partial y} \left(\tilde{G}_{yx} \tilde{E}_x + \tilde{G}_{yy} \tilde{E}_y + \tilde{G}_{yz} \tilde{E}_z \right) - \xi\zeta \tilde{G}_{zz} \tilde{E}_z \right] \right. \\ & \quad + \hat{y} \left[\left(k^2 + \frac{\partial^2}{\partial y^2} \right) \left(\tilde{G}_{yx} \tilde{E}_x + \tilde{G}_{yy} \tilde{E}_y + \tilde{G}_{yz} \tilde{E}_z \right) + j\xi \frac{\partial}{\partial y} \tilde{G}_{xx} \tilde{E}_x + j\zeta \frac{\partial}{\partial y} \tilde{G}_{zz} \tilde{E}_z \right] \\ & \quad \left. \left. + \hat{z} \left[(k^2 - \zeta^2) \tilde{G}_{zz} \tilde{E}_z + j\zeta \frac{\partial}{\partial y} \left(\tilde{G}_{yx} \tilde{E}_x + \tilde{G}_{yy} \tilde{E}_y + \tilde{G}_{yz} \tilde{E}_z \right) - \xi\zeta \tilde{G}_{xx} \tilde{E}_x \right] \right\} e^{j\xi(x-x')} dx' dy' \right] d\xi \} = 0 \end{aligned} \quad (4.36)$$

$$\begin{aligned}
& \int_{-\infty}^{\infty} \left[\int_{-W/2}^{W/2} \left\{ \hat{x} \left[(k^2 - \xi^2) \tilde{G}_{xx} \tilde{J}_x + j\xi \frac{\partial}{\partial y} \left(\tilde{G}_{yx} \tilde{J}_x + \tilde{G}_{yz} \tilde{J}_z \right) - \xi\zeta \tilde{G}_{zz} \tilde{J}_z \right] \right. \right. \\
& + \hat{y} \left[\left(k^2 + \frac{\partial^2}{\partial y^2} \right) \left(\tilde{G}_{yx} \tilde{J}_x + \tilde{G}_{yz} \tilde{J}_z \right) + j\xi \frac{\partial}{\partial y} \tilde{G}_{xx} \tilde{J}_x + j\zeta \frac{\partial}{\partial y} \tilde{G}_{zz} \tilde{J}_z \right] \\
& + \hat{z} \left[(k^2 - \zeta^2) \tilde{G}_{zz} \tilde{J}_z + j\zeta \frac{\partial}{\partial y} \left(\tilde{G}_{yx} \tilde{J}_x + \tilde{G}_{yz} \tilde{J}_z \right) - \xi\zeta \tilde{G}_{xx} \tilde{J}_x \right] \left. \right\} \frac{e^{j\xi(x-x')}}{2\pi j\omega\epsilon_1} dx' \\
& + \int_0^d \int_{-W/2}^{W/2} \frac{(\epsilon_3 - \epsilon_1)}{2\pi\epsilon_1} \left\{ \hat{x} \left[(k^2 - \xi^2) \tilde{G}_{xx} \tilde{E}_x + j\xi \frac{\partial}{\partial y} \left(\tilde{G}_{yx} \tilde{E}_x + \tilde{G}_{yy} \tilde{E}_y + \tilde{G}_{yz} \tilde{E}_z \right) - \xi\zeta \tilde{G}_{zz} \tilde{E}_z \right] \right. \\
& + \hat{y} \left[\left(k^2 + \frac{\partial^2}{\partial y^2} \right) \left(\tilde{G}_{yx} \tilde{E}_x + \tilde{G}_{yy} \tilde{E}_y + \tilde{G}_{yz} \tilde{E}_z \right) - \delta(y-y') + j\xi \frac{\partial}{\partial y} \tilde{G}_{xx} \tilde{E}_x + j\zeta \frac{\partial}{\partial y} \tilde{G}_{zz} \tilde{E}_z \right] \\
& + \hat{z} \left[(k^2 - \zeta^2) \tilde{G}_{zz} \tilde{E}_z + j\zeta \frac{\partial}{\partial y} \left(\tilde{G}_{yx} \tilde{E}_x + \tilde{G}_{yy} \tilde{E}_y + \tilde{G}_{yz} \tilde{E}_z \right) - \xi\zeta \tilde{G}_{xx} \tilde{E}_x \right] \left. \right\} e^{j\xi(x-x')} dx' dy' \Big] d\xi \\
& - \hat{x} \tilde{E}_x(x, y, \zeta) - \hat{y} \tilde{E}_y(x, y, \zeta) - \hat{z} \tilde{E}_z(x, y, \zeta) = 0
\end{aligned} \tag{4.37}$$

Note, this form assumes that the currents/fields are sufficiently smooth to allow this interchange and that the PV notation has been dropped for convenience. Again, it must be noted that the Green's function terms in (4.36) and (4.37) that are multiplied by the surface current are valid when $y' = d$ and the subscript p has been dropped from all ζ .

The next section will discuss how the Method of Moments will be used to discretize (4.36)-(4.37) and subsequently be solved for the p^{th} unknown eigenmode propagation constant of the modified microstrip structure in Figure 31.

4.3 Method of Moments

The solutions of (4.36) and (4.37) are discrete-mode strip currents and volumetric electric fields. As such, they lend themselves to the use of a Galerkin's Method of

Moments (MoM) solution. The coupled equations can then be solved for points at the discrete pole singularities ζ_p . It is from these singularity values that the propagation characteristics of the traveling wave microstrip structure can be directly determined.

The use of the Method of Moments to solve for the unknown strip currents and volumetric electric fields results in the homogeneous matrix equation

$$[L][u] = 0 \quad (4.38)$$

where $[L]$ is the matrix defined by the Green's function terms in (4.36) and (4.37) and the unknown vector $[u]$ is populated with the coefficients that define the strip currents and volumetric electric fields.

For non-trivial solutions, a propagation constant ζ_p exists that causes the determinant of $[L]$, written as $|L|$, to go to zero. A root search can then be used to find ζ_p for certain frequency/permittivity combinations. From these propagation constants; the radiation, surface, and bound regime characteristics of the antenna structure can be determined.

This section has given a brief overview of the Method of Moments and how it will be used to solve for the propagation characteristics of the microstrip structure. The next step in finding the propagation characteristics of the microstrip structure is to apply the MoM method to (4.36) and (4.37). It will be shown, with insight gained from the FDTD analysis in Chapter 2, that an appropriate choice of basis functions that closely model the fields and currents within the structure will significantly improve computational efficiency.

4.4 MoM Implementation

The previous section discussed how the unknown fields and currents within the EFIEs can be solved using the Method of Moments. This section will now apply the method to the coupled equations derived in Section 4.2 to build the desired matrix $[L]$. This matrix can then be used to find the propagation characteristics of the microstrip structure by numerically searching for ζ values that satisfy the relation $|L|=0$ (rigorously, $|L| < tol$, where tol is the specified solution accuracy – found that $tol = 1 \times 10^{-6}$ resulted in converging values for ζ).

As previously mentioned, an important step in the MoM technique is to expand the unknown fields and currents. The unknown electric field at a source point in Region 3 can be written as a summation of weighted basis functions

$$\begin{aligned}\tilde{E}(x', y', \zeta) &= \hat{x} \tilde{E}_x(x', y', \zeta) + \hat{y} \tilde{E}_y(x', y', \zeta) + \hat{z} \tilde{E}_z(x', y', \zeta) \\ &\cong \hat{x} \sum_{n=1}^N a_n e_{xn}(x', y', \zeta) + \hat{y} \sum_{n=1}^N b_n e_{yn}(x', y', \zeta) + \hat{z} \sum_{n=1}^N c_n e_{zn}(x', y', \zeta)\end{aligned}\quad (4.39)$$

where e_{xn} , e_{yn} , and e_{zn} are known expansion functions and a_n , b_n , and c_n are the unknown expansion coefficients. Note, the same expansion is used for a field point in Region 3. Similarly, for the surface currents

$$\begin{aligned}\tilde{J}_s(x', d, \zeta) &= \hat{x} \tilde{J}_x(x', d, \zeta) + \hat{z} \tilde{J}_z(x', d, \zeta) \\ &\cong \hat{x} \sum_{n=1}^N d_n j_{xn}(x', d, \zeta) + \hat{z} \sum_{n=1}^N e_n j_{zn}(x', d, \zeta)\end{aligned}\quad (4.40)$$

where j_{xn} and j_{zn} are known expansion functions and d_n and e_n are unknown expansion coefficients (note, the surface current component j_{yn} is not supported since the strip

conductor is assumed to be infinitesimally thin). Although theoretically an infinite number of expansion terms are generally required, only N terms are utilized for practical implementation of the MoM method (N is chosen sufficiently large to reach convergence within a specified tolerance).

Inserting (4.39) and (4.40) into (4.36) and (4.37), the resultant EFIEs can be decomposed into \hat{x} , \hat{y} , and \hat{z} components. Bringing the summation outside the integrals and dropping the x' , y' , and ζ notation within the Green's functions and fields and currents for notational convenience results in

for \hat{x} :

$$\begin{aligned} \lim_{y \rightarrow d} \left\{ \sum_{n=1}^N \int_{-\infty}^{\infty} \int_{-W/2}^{W/2} \left[(k^2 - \xi^2) \tilde{G}_{xx} d_n j_{xn} + j\xi \frac{\partial}{\partial y} \left(\tilde{G}_{yx} d_n j_{xn} + \tilde{G}_{yz} e_n j_{zn} \right) - \xi\zeta \tilde{G}_{zz} e_n j_{zn} \right] \frac{e^{j\xi(x-x')}}{2\pi j\omega\epsilon_1} dx' \right. \\ \left. + \int_0^d \int_{-W/2}^{W/2} \frac{(\epsilon_3 - \epsilon_1)}{2\pi\epsilon_1} \left[(k^2 - \xi^2) \tilde{G}_{xx} a_n e_{xn} + j\xi \frac{\partial}{\partial y} \left(\tilde{G}_{yx} a_n e_{xn} + \tilde{G}_{yy} b_n e_{yn} + \tilde{G}_{yz} c_n e_{zn} \right) - \xi\zeta \tilde{G}_{zz} c_n e_{zn} \right] \right. \\ \left. \cdot e^{j\xi(x-x')} dx' dy' \right] d\xi \Big\} = 0 \end{aligned} \quad (4.41)$$

$$\begin{aligned} \sum_{n=1}^N \int_{-\infty}^{\infty} \int_{-W/2}^{W/2} \left[(k^2 - \xi^2) \tilde{G}_{xx} d_n j_{xn} + j\xi \frac{\partial}{\partial y} \left(\tilde{G}_{yx} d_n j_{xn} + \tilde{G}_{yz} e_n j_{zn} \right) - \xi\zeta \tilde{G}_{zz} e_n j_{zn} \right] \frac{e^{j\xi(x-x')}}{2\pi j\omega\epsilon_1} dx' \\ + \int_0^d \int_{-W/2}^{W/2} \frac{(\epsilon_3 - \epsilon_1)}{2\pi\epsilon_1} \left[(k^2 - \xi^2) \tilde{G}_{xx} a_n e_{xn} + j\xi \frac{\partial}{\partial y} \left(\tilde{G}_{yx} a_n e_{xn} + \tilde{G}_{yy} b_n e_{yn} + \tilde{G}_{yz} c_n e_{zn} \right) - \xi\zeta \tilde{G}_{zz} c_n e_{zn} \right] \\ \cdot e^{j\xi(x-x')} dx' dy' \Big] d\xi - \sum_{n=1}^N a_n e_{xn}(x, y, \zeta) = 0 \end{aligned} \quad (4.42)$$

for \hat{y} :

$$\begin{aligned} & \sum_{n=1}^N \int_{-\infty}^{\infty} \int_{-W/2}^{W/2} \left[\left(k^2 + \frac{\partial^2}{\partial y^2} \right) \left(\tilde{G}_{yx} d_n j_{xn} + \tilde{G}_{yz} e_n j_{zn} \right) + j\zeta \frac{\partial}{\partial y} \tilde{G}_{xx} d_n j_{xn} + j\zeta \frac{\partial}{\partial y} \tilde{G}_{zz} e_n j_{zn} \right] \frac{e^{j\zeta(x-x')}}{2\pi j\omega\epsilon_1} dx' \\ & + \int_0^d \int_{-W/2}^{W/2} \frac{(\epsilon_3 - \epsilon_1)}{2\pi\epsilon_1} \left[\left(k^2 + \frac{\partial^2}{\partial y^2} \right) \left(\tilde{G}_{yx} a_n e_{xn} + \tilde{G}_{yy} b_n e_{yn} + \tilde{G}_{yz} c_n e_{zn} \right) + j\zeta \frac{\partial}{\partial y} \tilde{G}_{xx} a_n e_{xn} + j\zeta \frac{\partial}{\partial y} \tilde{G}_{zz} c_n e_{zn} \right] \\ & \cdot e^{j\zeta(x-x')} dx' dy' \Big] d\zeta - \sum_{n=1}^N b_n e_{yn}(x, y, \zeta) = 0 \end{aligned} \quad (4.43)$$

for \hat{z} :

$$\begin{aligned} & \lim_{y \rightarrow d} \left\{ \sum_{n=1}^N \int_{-\infty}^{\infty} \int_{-W/2}^{W/2} \left[(k^2 - \zeta^2) \tilde{G}_{zz} e_n j_{zn} + j\zeta \frac{\partial}{\partial y} \left(\tilde{G}_{yx} d_n j_{xn} + \tilde{G}_{yz} e_n j_{zn} \right) - \xi\zeta \tilde{G}_{xx} d_n j_{xn} \right] \frac{e^{j\zeta(x-x')}}{2\pi j\omega\epsilon_1} dx' \right. \\ & \left. + \int_0^d \int_{-W/2}^{W/2} \frac{(\epsilon_3 - \epsilon_1)}{2\pi\epsilon_1} \left[(k^2 - \zeta^2) \tilde{G}_{zz} c_n e_{zn} + j\zeta \frac{\partial}{\partial y} \left(\tilde{G}_{yx} a_n e_{xn} + \tilde{G}_{yy} b_n e_{yn} + \tilde{G}_{yz} c_n e_{zn} \right) - \xi\zeta \tilde{G}_{xx} a_n e_{xn} \right] \right. \\ & \left. \cdot e^{j\zeta(x-x')} dx' dy' \right] d\zeta \Big\} = 0 \end{aligned} \quad (4.44)$$

$$\begin{aligned} & \sum_{n=1}^N \int_{-\infty}^{\infty} \int_{-W/2}^{W/2} \left[(k^2 - \zeta^2) \tilde{G}_{zz} e_n j_{zn} + j\zeta \frac{\partial}{\partial y} \left(\tilde{G}_{yx} d_n j_{xn} + \tilde{G}_{yz} e_n j_{zn} \right) - \xi\zeta \tilde{G}_{xx} d_n j_{xn} \right] \frac{e^{j\zeta(x-x')}}{2\pi j\omega\epsilon_1} dx' \\ & + \int_0^d \int_{-W/2}^{W/2} \frac{(\epsilon_3 - \epsilon_1)}{2\pi\epsilon_1} \left[(k^2 - \zeta^2) \tilde{G}_{zz} c_n e_{zn} + j\zeta \frac{\partial}{\partial y} \left(\tilde{G}_{yx} a_n e_{xn} + \tilde{G}_{yy} b_n e_{yn} + \tilde{G}_{yz} c_n e_{zn} \right) - \xi\zeta \tilde{G}_{xx} a_n e_{xn} \right] \\ & \cdot e^{j\zeta(x-x')} dx' dy' \Big] d\zeta - \sum_{n=1}^N c_n e_{zn}(x, y, \zeta) = 0 \end{aligned} \quad (4.45)$$

Note that the total field appearing outside the integral in (4.42), (4.43), and (4.45) is represented as a summation of expansion functions in x and y (not x' and y').

Applying the Galerkin testing operators (discussed in the next section) to (4.41) through (4.45) will result in a matrix of the form (see Appendix C for an explanation as to how (4.47) through (4.71) are extracted from (4.41) through (4.45))

$$\begin{bmatrix} A_{mn} & B_{mn} & C_{mn} & D_{mn} & E_{mn} \\ F_{mn} & G_{mn} & H_{mn} & I_{mn} & J_{mn} \\ K_{mn} & L_{mn} & M_{mn} & N_{mn} & O_{mn} \\ P_{mn} & Q_{mn} & R_{mn} & S_{mn} & T_{mn} \\ U_{mn} & V_{mn} & W_{mn} & X_{mn} & Y_{mn} \end{bmatrix} \cdot \begin{bmatrix} a_n \\ b_n \\ c_n \\ d_n \\ e_n \end{bmatrix} = 0 \quad (4.46)$$

where

$$A_{mn} = \int_{-\infty}^{\infty} \int_0^d \int_{-W/2}^{W/2} \frac{(\varepsilon_3 - \varepsilon_1)}{2\pi\varepsilon_1} \left[(k^2 - \xi^2) \tilde{G}_{xx} + j\xi \frac{\partial}{\partial y} \tilde{G}_{yx} \right] e_{xn}(x', y') e_{xm}(x, y) e^{j\xi(x-x')} dx' dy' dx dy d\xi \\ - \int_0^d \int_{-W/2}^{W/2} e_{xn}(x, y) e_{xm}(x, y) dx dy \quad (4.47)$$

$$B_{mn} = \int_{-\infty}^{\infty} \int_0^d \int_{-W/2}^{W/2} \frac{(\varepsilon_3 - \varepsilon_1)}{2\pi\varepsilon_1} \left[j\xi \frac{\partial}{\partial y} \tilde{G}_{yy} e_{yn}(x', y') e_{xm}(x, y) \right] e^{j\xi(x-x')} dx' dy' dx dy d\xi \quad (4.48)$$

$$C_{mn} = \int_{-\infty}^{\infty} \int_0^d \int_{-W/2}^{W/2} \frac{(\varepsilon_3 - \varepsilon_1)}{2\pi\varepsilon_1} \left[j\xi \frac{\partial}{\partial y} \tilde{G}_{yz} - \xi\xi \tilde{G}_{zz} \right] e_{zn}(x', y') e_{xm}(x, y) e^{j\xi(x-x')} dx' dy' dx dy d\xi \quad (4.49)$$

$$D_{mn} = \int_{-\infty}^{\infty} \int_{-W/2}^{W/2} \int_0^d \left[(k^2 - \xi^2) \tilde{G}_{xx} + j\xi \frac{\partial}{\partial y} \tilde{G}_{yx} \right] j_{xn}(x') e_{xm}(x, y) \frac{e^{j\xi(x-x')}}{2\pi j\omega\varepsilon_1} dx' dx dy d\xi \quad (4.50)$$

$$E_{mn} = \int_{-\infty}^{\infty} \int_{-W/2}^{W/2} \int_0^d \left[j\xi \frac{\partial}{\partial y} \tilde{G}_{yz} - \xi\xi \tilde{G}_{zz} \right] j_{zn}(x') e_{xm}(x, y) \frac{e^{j\xi(x-x')}}{2\pi j\omega\varepsilon_1} dx' dx dy d\xi \quad (4.51)$$

$$F_{mn} = \int_{-\infty}^{\infty} \int_0^d \int_{-W/2}^{W/2} \frac{(\varepsilon_3 - \varepsilon_1)}{2\pi\varepsilon_1} \left[(k^2 + \frac{\partial^2}{\partial y^2}) \tilde{G}_{yx} + j\xi \frac{\partial}{\partial y} \tilde{G}_{xx} \right] e_{xn}(x', y') e_{ym}(x, y) e^{j\xi(x-x')} dx' dy' dx dy d\xi \quad (4.52)$$

$$G_{mn} = \int_{-\infty}^{\infty} \int_0^d \int_{-W/2}^{W/2} \frac{(\varepsilon_3 - \varepsilon_1)}{2\pi\varepsilon_1} \left[\left((k^2 + \frac{\partial^2}{\partial y^2}) \tilde{G}_{yy} - \delta(\vec{r} - \vec{r}') \right) e_{yn}(x', y') e_{ym}(x, y) \right] e^{j\xi(x-x')} dx' dy' dx dy d\xi \\ - \int_0^d \int_{-W/2}^{W/2} e_{yn}(x, y) e_{ym}(x, y) dx dy \quad (4.53)$$

$$H_{mn} = \int_{-\infty}^{\infty} \int_0^d \int_{-W/2}^{W/2} \frac{(\varepsilon_3 - \varepsilon_1)}{2\pi\varepsilon_1} \left[(k^2 + \frac{\partial^2}{\partial y^2}) \tilde{G}_{yz} + j\zeta \frac{\partial}{\partial y} \tilde{G}_{zz} \right] e_{zn}(x', y') e_{ym}(x, y) e^{j\xi(x-x')} dx' dy' dx dy d\xi \quad (4.54)$$

$$I_{mn} = \int_{-\infty}^{\infty} \int_{-W/2}^{W/2} \int_0^d \left[(k^2 + \frac{\partial^2}{\partial y^2}) \tilde{G}_{yx} + j\zeta \frac{\partial}{\partial y} \tilde{G}_{xx} \right] j_{xn}(x') e_{ym}(x, y) \frac{e^{j\xi(x-x')}}{2\pi j\omega\varepsilon_1} dx' dx dy d\xi \quad (4.55)$$

$$J_{mn} = \int_{-\infty}^{\infty} \int_{-W/2}^{W/2} \int_0^d \left[(k^2 + \frac{\partial^2}{\partial y^2}) \tilde{G}_{yz} + j\zeta \frac{\partial}{\partial y} \tilde{G}_{zz} \right] j_{zn}(x') e_{ym}(x, y) \frac{e^{j\xi(x-x')}}{2\pi j\omega\varepsilon_1} dx' dx dy d\xi \quad (4.56)$$

$$K_{mn} = \int_{-\infty}^{\infty} \int_0^d \int_{-W/2}^{W/2} \frac{(\varepsilon_3 - \varepsilon_1)}{2\pi\varepsilon_1} \left[j\zeta \frac{\partial}{\partial y} \tilde{G}_{yx} - \xi\zeta \tilde{G}_{xx} \right] e_{xn}(x', y') e_{zm}(x, y) e^{j\xi(x-x')} dx' dy' dx dy d\xi \quad (4.57)$$

$$L_{mn} = \int_{-\infty}^{\infty} \int_0^d \int_{-W/2}^{W/2} \frac{(\varepsilon_3 - \varepsilon_1)}{2\pi\varepsilon_1} \left[j\zeta \frac{\partial}{\partial y} \tilde{G}_{yy} e_{yn}(x', y') e_{zm}(x, y) \right] e^{j\xi(x-x')} dx' dy' dx dy d\xi \quad (4.58)$$

$$M_{mn} = \int_{-\infty}^{\infty} \int_0^d \int_{-W/2}^{W/2} \frac{(\varepsilon_3 - \varepsilon_1)}{2\pi\varepsilon_1} \left[(k^2 - \zeta^2) \tilde{G}_{zz} + j\zeta \frac{\partial}{\partial y} \tilde{G}_{yz} \right] e_{zn}(x', y') e_{zm}(x, y) e^{j\xi(x-x')} dx' dy' dx dy d\xi \\ - \int_0^d \int_{-W/2}^{W/2} e_{zn}(x, y) e_{zm}(x, y) dx dy \quad (4.59)$$

$$N_{mn} = \int_{-\infty}^{\infty} \int_{-W/2}^{W/2} \int_0^d \left[j\zeta \frac{\partial}{\partial y} \tilde{G}_{yx} - \xi\zeta \tilde{G}_{xx} \right] j_{xn}(x') e_{zm}(x, y) \frac{e^{j\xi(x-x')}}{2\pi j\omega\varepsilon_1} dx' dx dy d\xi \quad (4.60)$$

$$O_{mn} = \int_{-\infty}^{\infty} \int_{-W/2}^{W/2} \int_0^d \left[(k^2 - \zeta^2) \tilde{G}_{zz} + j\zeta \frac{\partial}{\partial y} \tilde{G}_{yz} \right] j_{zn}(x') e_{zm}(x, y) \frac{e^{j\xi(x-x')}}{2\pi j\omega\varepsilon_1} dx' dx dy d\xi \quad (4.61)$$

$$P_{mn} = \lim_{y \rightarrow d} \hat{t} \cdot \left\{ \int_{-\infty}^{\infty} \int_0^d \int_{-W/2}^{W/2} \frac{(\varepsilon_3 - \varepsilon_1)}{2\pi\varepsilon_1} \left[j\zeta \frac{\partial}{\partial y} \tilde{G}_{yx} - \xi\zeta \tilde{G}_{xx} \right] e_{xn}(x', y') j_{zm}(x) e^{j\xi(x-x')} dx' dy' dx d\xi \right\} \quad (4.62)$$

$$Q_{mn} = \lim_{y \rightarrow d} \hat{t} \cdot \left\{ \int_{-\infty}^{\infty} \int_0^d \int_{-W/2}^{W/2} \frac{(\varepsilon_3 - \varepsilon_1)}{2\pi\varepsilon_1} \left[j\zeta \frac{\partial}{\partial y} \tilde{G}_{yy} e_{yn}(x', y') j_{zm}(x) \right] e^{j\xi(x-x')} dx' dy' dx d\xi \right\} \quad (4.63)$$

$$R_{mn} = \lim_{y \rightarrow d} \hat{t} \cdot \left\{ \int_{-\infty}^{\infty} \int_0^d \int_{-W/2}^{W/2} \frac{(\varepsilon_3 - \varepsilon_1)}{2\pi\varepsilon_1} \left[(k^2 - \zeta^2) \tilde{G}_{zz} + j\zeta \frac{\partial}{\partial y} \tilde{G}_{yz} \right] e_{zn}(x', y') j_{zm}(x) e^{j\xi(x-x')} dx' dy' dx d\xi \right\} \quad (4.64)$$

$$S_{mn} = \lim_{y \rightarrow d} \hat{t} \cdot \left\{ \int_{-\infty}^{\infty} \int_{-W/2}^{W/2} \left[j\zeta \frac{\partial}{\partial y} \tilde{G}_{yx} - \xi\zeta \tilde{G}_{xx} \right] j_{xn}(x') j_{zm}(x) \frac{e^{j\xi(x-x')}}{2\pi j\omega\varepsilon_1} dx' dx d\xi \right\} \quad (4.65)$$

$$T_{mn} = \lim_{y \rightarrow d} \hat{t} \cdot \left\{ \int_{-\infty}^{\infty} \int_{-W/2}^{W/2} \left[(k^2 - \zeta^2) \tilde{G}_{zz} + j\zeta \frac{\partial}{\partial y} \tilde{G}_{yz} \right] j_{zn}(x') j_{zm}(x) \frac{e^{j\xi(x-x')}}{2\pi j\omega\varepsilon_1} dx' dx d\xi \right\} \quad (4.66)$$

$$U_{mn} = \lim_{y \rightarrow d} \hat{t} \cdot \left\{ \int_{-\infty}^{\infty} \int_0^d \int_{-W/2}^{W/2} \frac{(\varepsilon_3 - \varepsilon_1)}{2\pi\varepsilon_1} \left[(k^2 - \xi^2) \tilde{G}_{xx} + j\xi \frac{\partial}{\partial y} \tilde{G}_{yx} \right] e_{xn}(x', y') j_{xm}(x) e^{j\xi(x-x')} dx' dy' dx d\xi \right\} \quad (4.67)$$

$$V_{mn} = \lim_{y \rightarrow d} \hat{t} \cdot \left\{ \int_{-\infty}^{\infty} \int_0^d \int_{-W/2}^{W/2} \frac{(\varepsilon_3 - \varepsilon_1)}{2\pi\varepsilon_1} \left[j\xi \frac{\partial}{\partial y} \tilde{G}_{yy} e_{yn}(x', y') j_{xm}(x) \right] e^{j\xi(x-x')} dx' dy' dx d\xi \right\} \quad (4.68)$$

$$W_{mn} = \lim_{y \rightarrow d} \hat{t} \cdot \left\{ \int_{-\infty}^{\infty} \int_0^d \int_{-W/2}^{W/2} \frac{(\varepsilon_3 - \varepsilon_1)}{2\pi\varepsilon_1} \left[j\xi \frac{\partial}{\partial y} \tilde{G}_{yz} - \xi\zeta \tilde{G}_{zz} \right] e_{zn}(x', y') j_{xm}(x) e^{j\xi(x-x')} dx' dy' dx d\xi \right\} \quad (4.69)$$

$$X_{mn} = \lim_{y \rightarrow d} \hat{t} \cdot \left\{ \int_{-\infty}^{\infty} \int_{-W/2}^{W/2} \left[(k^2 - \xi^2) \tilde{G}_{xx} + j\xi \frac{\partial}{\partial y} \tilde{G}_{yx} \right] j_{xn}(x') j_{xm}(x) \frac{e^{j\xi(x-x')}}{2\pi j\omega\varepsilon_1} dx' dx d\xi \right\} \quad (4.70)$$

$$Y_{mn} = \lim_{y \rightarrow d} \hat{t} \cdot \left\{ \int_{-\infty}^{\infty} \int_{-W/2}^{W/2} \left[j\xi \frac{\partial}{\partial y} \tilde{G}_{yz} - \xi\zeta \tilde{G}_{zz} \right] j_{zn}(x') j_{xm}(x) \frac{e^{j\xi(x-x')}}{2\pi j\omega\varepsilon_1} dx' dx d\xi \right\} \quad (4.71)$$

Note that the expansion coefficients (a_n to e_n), each of length N , in (4.41) to (4.45) form the unknown vector $[u]$ in (4.46).

$$\begin{array}{c}
\begin{array}{l}
\text{volume observer – volume source} \\
\text{volume observer – surface source } y'=d
\end{array} \\
\begin{array}{c}
E_{xn} \quad E_{yn} \quad E_{zn} \quad J_{xn} \quad J_{zn} \\
\begin{array}{c}
E_{xm} \\
E_{ym} \\
E_{zm} \\
J_{zm} \\
J_{xm}
\end{array}
\begin{array}{|c|c|c|c|c|}
\hline
\text{green} & \text{green} & \text{green} & \text{yellow} & \text{yellow} \\
\hline
A_{mn} & B_{mn} & C_{mn} & D_{mn} & E_{mn} \\
F_{mn} & G_{mn} & H_{mn} & I_{mn} & J_{mn} \\
K_{mn} & L_{mn} & M_{mn} & N_{mn} & O_{mn} \\
\hline
\text{blue} & \text{blue} & \text{blue} & \text{white} & \text{white} \\
\hline
P_{mn} & Q_{mn} & R_{mn} & S_{mn} & T_{mn} \\
U_{mn} & V_{mn} & W_{mn} & X_{mn} & Y_{mn} \\
\hline
\end{array}
\begin{array}{c}
a_n \\
b_n \\
c_n \\
d_n \\
e_n
\end{array}
\end{array}
= \begin{array}{c}
0 \\
0 \\
0 \\
0 \\
0
\end{array}
\end{array}$$

$\boxed{\vec{E}^s(\vec{r}) - \vec{E}(\vec{r}) = 0}$ $\boxed{\hat{t} \cdot \vec{E}^s(\vec{r}) = 0}$

$\text{surface observer – volume source } y=d$ $\text{surface observer – surface source } y=y'=d$

Figure 32: Equation (4.46) split into the four regions of interaction between source and observer locations.

4.4.2 Interpretation of MoM Matrix Elements

The matrix (4.46) is made up of the Green's function terms found in (4.47) through (4.71). Each of these has a physical interpretation as to what they represent within the microstrip structure. This section will describe each of these functions and what physical interactions they represent and will provide the reader with a better understanding of what is driving the results seen in the following chapter.

In order to gain a better understanding of what each element of (4.46) represents, refer to Figure 32. The figure clearly depicts four distinct regions. These represent the four types of interactions that take place in the microstrip structure: volume-volume, volume-surface, surface-volume, and surface-surface. For each of these descriptions, the

first term represents the observer (field or current) and uses m as its designator. The second terms represents the source (field or current) and uses n as its designator. Thus, the green section, for example, would describe the terms that take into account an x , y , or z -directed electric field (n^{th} volume source term) acting on an x , y , or z -directed electric field (m^{th} volume observer term). As an example, the B_{mn} term would represent the n^{th} x -directed volume observed electric field due to the m^{th} y -directed volume source electric field. The matrix terms A_{mn} , B_{mn} , C_{mn} , F_{mn} , G_{mn} , H_{mn} , K_{mn} , L_{mn} , and M_{mn} account for all of the volume-volume interactions in the antenna.

The volume observer – surface source terms are highlighted in the yellow region and include the terms D_{mn} , E_{mn} , I_{mn} , J_{mn} , N_{mn} , and O_{mn} . For all of these terms, $y' = d$ since they involve having the source term located on the strip conductor. As an example, the I_{mn} term would represent the m^{th} y -directed volume observed electric field due to the n^{th} x -directed surface current source.

The surface observer – volume source terms are highlighted in the blue region and include the P_{mn} , Q_{mn} , R_{mn} , U_{mn} , V_{mn} , and W_{mn} terms. For all of these terms, $y = d$ since they involve having the observation term located on the strip conductor. This will be accounted for in the integrals themselves, with any derivatives with respect to y being taken *before* $y = d$ is applied. As an example, the Q_{mn} term would represent the m^{th} z -directed current observed on the surface due to the n^{th} y -directed electric field volume source.

Lastly, the surface observer – surface source terms are highlighted in the white region and include the S_{mn} , T_{mn} , X_{mn} , and Y_{mn} sub-matrix terms. For all of these terms,

$y' = d$ and $y = d$ since they involve having the source and the observer located on the strip conductor. Again, any derivatives with respect to y are being taken *before* $y = d$ is applied. As an example, the Y_{mn} term would represent the m^{th} z -directed observer surface current due to the n^{th} x -directed source surface current.

Now that the various terms representing the interactions within the microstrip structure have been identified in (4.46), it is necessary to represent these currents and fields properly using appropriate basis functions. The next section will go through the process by which these basis functions were chosen.

4.4.1 Basis Functions

The last step in developing the matrix that represents the coupled EFIEs of interest is to properly choose the basis functions. The basis functions will serve as the expansion and test functions found in (4.47) - (4.71) that represent the electric fields and surface currents within the microstrip structure. Because of this, they should be representative of how the real physical fields and currents behave. For example, if it is known that a current will be at a maximum in the center of the conducting strip (in x'), then it is ill-advised to choose a basis function that is odd in nature to represent this current. The oddness of the function will always cause the magnitude of the current to be zero at the center ($x' = 0$), which is non-physical for certain modes.

Sine and cosine basis functions were chosen for this research effort due to their even/odd nature; their ability to closely mimic the electric fields and currents within the microstrip structure; and their orthogonal characteristics.

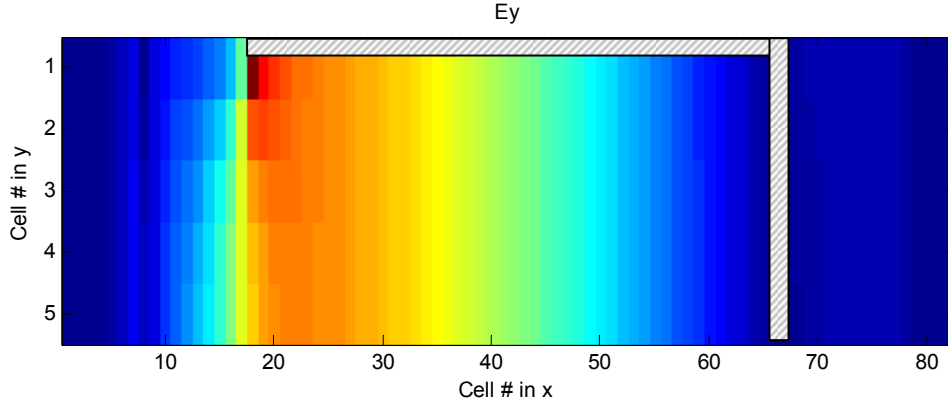


Figure 33: The FDTD y -directed electric fields within the cross-section of Thiele half-width antenna. The vertical shunt is at cell #68 and the edge of the top conductor is at cell #18.

In order to properly choose which sine and cosine basis functions should be used to model the x -, y -, and z -directed fields and the x - and z -directed surface currents, insight was needed as to how these behave within the structure. Looking at the structure in Figure 2 and knowing that the antenna is designed to operate in the first higher order mode (see Figure 4), the even and odd nature of the fields and currents can be deduced.

Operating in the first higher order mode requires the y -directed electric fields within region 3 to be odd about the center point ($x' = 0$). Physically, this means that the y -directed fields must always equal zero at this point. A sine function in x' will properly model these fields, given its odd nature. Thus, a reasonable choice for $e_{yn}(x')$ is

$$e_{yn}(x') = \sin \frac{(2n+1)\pi x'}{W} \quad n = 0, 1, 2, \dots \quad (4.72)$$

In order to validate the choice of basis functions, an intensity plot of the electric fields inside Region 3 was analyzed from the FDTD simulations performed earlier in this research (see Figure 33). The plot is of the y -directed electric fields in the cross-section

of the Thiele half-width antenna, thus the shunt exists at $x=0$. It can be seen in the plot that these fields indeed are greatest at the edge of the top conductor (cell #18 in x) and go to zero at the location of the shunt (cell # 66 in x). Thus, the choice of a sine basis function appears to be a physically reasonable choice. In addition, its mathematical properties are sufficiently smooth to ensure the resulting integrals will be well behaved.

The behavior of the currents on the conductive strip is fairly well known for a microstrip antenna [13]. Any transverse current moving in the x -direction is going to be driven to zero at the edges ($x' = \pm W/2$). It is also shown in [13] that J_x can also be at a maximum value at $x' = 0$. A cosine function in x' will model this properly, leading to

$$j_{xn}(x') = \cos \frac{(2n+1)\pi x'}{W} \quad n = 0, 1, 2, \dots \quad (4.73)$$

Conversely, the longitudinal (z -directed) currents moving down the length of the conductor will be at a maximum at the edges ($x' = \pm W/2$) and zero in the center [13]. A sine function in x' will model this current adequately, namely

$$j_{zn}(x') = \sin \frac{(2n+1)\pi x'}{W} \quad n = 0, 1, 2, \dots \quad (4.74)$$

For the remaining two unknowns (the x - and z -directed electric fields), the nature of these will be strongly influenced by the respective currents on the conducting strip. Thus, given that the x -directed currents are represented as an even function in x , the electric fields in the volume will also be an even function (due to the relation between the fields, potentials, and currents), thus

$$e_{xn}(x') = \cos \frac{(2n+1)\pi x'}{W} \quad n = 0, 1, 2, \dots \quad (4.75)$$

The z -directed currents were shown to have odd basis functions in x . The fields supported by these currents in the volume will also be odd in x (again, due to the relation between the fields, potentials, and currents), therefore

$$e_{zn}(x') = \sin \frac{(2n+1)\pi x'}{W} \quad n = 0, 1, 2, \dots \quad (4.76)$$

Only the electric fields will require basis functions in the y -direction. It is known that the transverse fields (x and z) will vanish at a PEC surface. Thus, at the surface of the top conductor ($y=d$) and the PEC ground plane ($y=0$), a sine basis function will always go to zero at these points. Thus, a suitable representation for $e_{xn}(y')$ and $e_{zn}(y')$ is

$$e_{xn}(y') = \sin \frac{(n+1)\pi y'}{d} \quad n = 0, 1, 2, \dots \quad (4.77)$$

$$e_{zn}(y') = \sin \frac{(n+1)\pi y'}{d} \quad n = 0, 1, 2, \dots \quad (4.78)$$

Again, looking at an intensity plot of the y -directed fields from the FDTD simulations (Figure 33), it can be seen how the y -directed fields stay fairly constant from 0 to d in y' (as expected from this approximate parallel-plate region). They do not go to zero at the surface of the PECs, like the transverse fields do (as expected from the boundary conditions on the normal component of electric field at a PEC surface). Given this, a cosine function is best suited to represent these fields, that is

$$e_{yn}(y') = \cos \frac{n\pi y'}{d} \quad n = 0, 1, 2, \dots \quad (4.79)$$

If, indeed, the fields are of constant value from 0 to d , the cosine basis function would still model it properly by having $n=0$ (thus, the basis function is a constant value of $\cos(0)=1$ from 0 to d).

The Galerkin test functions used will be the same as the expansion functions, but with the variables n , x' , and y' swapped with m , x , and y to give

$$j_{xm}(x) = \cos \frac{(2m+1)\pi x}{W} \quad m = 0, 1, 2, \dots \quad (4.80)$$

$$j_{zm}(x) = \sin \frac{(2m+1)\pi x}{W} \quad m = 0, 1, 2, \dots \quad (4.81)$$

$$e_{xm}(x) = \cos \frac{(2m+1)\pi x}{W} \quad m = 0, 1, 2, \dots \quad (4.82)$$

$$e_{ym}(x) = \sin \frac{(2m+1)\pi x}{W} \quad m = 0, 1, 2, \dots \quad (4.83)$$

$$e_{zm}(x) = \sin \frac{(2m+1)\pi x}{W} \quad m = 0, 1, 2, \dots \quad (4.84)$$

$$e_{xm}(y) = \sin \frac{(m+1)\pi y}{d} \quad m = 0, 1, 2, \dots \quad (4.85)$$

$$e_{ym}(y) = \cos \frac{m\pi y}{d} \quad m = 0, 1, 2, \dots \quad (4.86)$$

$$e_{zm}(y) = \sin \frac{(m+1)\pi y}{d} \quad m = 0, 1, 2, \dots \quad (4.87)$$

These basis functions are summarized in Table 5.

Upon inserting the expansion and test functions given in (4.72) to (4.87) into the matrix elements defined by (4.47) to (4.71), these terms can finally be integrated in x , x' , y , and y' . The resultant matrix elements will therefore be functions of ξ and ζ . The

Table 5: Basis Functions Used to Represent Unknown Currents and Electric Fields (n Unknowns are the Same as the m Unknown Values Shown).

The diagram shows a cross-section of a microstrip structure. A central blue region, labeled 'Region 3', is bounded by $x = -w/2$ and $x = w/2$. It is flanked by two grey regions, 'Region 1' on the right and 'Region 2' on the left. The entire structure is on a hatched substrate labeled 'PEC'. The vertical axis is y , with the top boundary at $y = d$ and the bottom boundary at $y = 0$. The horizontal axis is x . A point C is marked on the top boundary of Region 3. A coordinate z is shown at the bottom center of Region 3.

$$j_{xm}(x) = \cos \frac{(2m+1)\pi x}{W} \quad m = 0, 1, 2, \dots$$

$$m = 0, 1, 2, \dots$$

$$j_{zm}(x) = \sin \frac{(2m+1)\pi x}{W} \quad m = 0, 1, 2, \dots$$

$$m = 0, 1, 2, \dots$$

$$e_{xm}(x) = \cos \frac{(2m+1)\pi x}{W} \quad m = 0, 1, 2, \dots$$

$$m = 0, 1, 2, \dots$$

$$e_{xm}(y) = \sin \frac{(m+1)\pi y}{d} \quad m = 0, 1, 2, \dots$$

$$m = 0, 1, 2, \dots$$

$$e_{ym}(x) = \sin \frac{(2m+1)\pi x}{W} \quad m = 0, 1, 2, \dots$$

$$m = 0, 1, 2, \dots$$

$$e_{ym}(y) = \cos \frac{m\pi y}{d} \quad m = 0, 1, 2, \dots$$

$$m = 0, 1, 2, \dots$$

$$e_{zm}(x) = \sin \frac{(2m+1)\pi x}{W} \quad m = 0, 1, 2, \dots$$

$$m = 0, 1, 2, \dots$$

$$e_{zm}(y) = \sin \frac{(m+1)\pi y}{d} \quad m = 0, 1, 2, \dots$$

$$m = 0, 1, 2, \dots$$

variable ζ is subsequently numerically iterated using Newton's method until the condition $|L| < tol$ is satisfied, resulting in the desired propagation constant ζ_p (the prior FDTD analysis is used to obtain the initial guess in this research).

The next step in finding the propagation constants of the microstrip structure is to consider the integration path of the matrix elements in ξ . Although the inverse Fourier transform path is along the real ξ axis, complex pole and branch point migration behavior constrains the integration path and consequently complicates the analysis and is discussed in the next section.

4.4.2 Integration Path

As discussed in Section 1.3.4, the microstrip structure used in this research can operate in four distinct regimes: reactive, radiation, surface, and bound. Each regime has distinct features as to how electromagnetic fields propagate throughout the structure; and are ultimately defined by the pole and branch point singularities that are associated with the EFIEs. The EFIEs derived in (4.36) and (4.37) represent a set of equations that define the propagation and coupling of electromagnetic energy within the structure. Closer investigation of these equations reveals situations where singularities will exist (where the denominator or square root functions will vanish). Some of these singularities (i.e., branch point) exist within Region 1 (those associated with p_1). These are removable singularities since these equations are even with respect to p_1 [14]. The branch point singularities associated with p_2 , however, are not removable and must be handled appropriately.

Another singularity, a simple pole (i.e., a discrete surface wave mode) associated with the background environment, is identified with the denominator found in the Green's function derived in Chapter 3 ((3.98) to (3.100)) when

$$p_2 N^2 + p_1 + (p_2 N^2 - p_1) e^{-2p_1 d} = 0 \quad (4.88)$$

or, rearranging terms

$$p_2 N^2 + p_1 \tanh p_1 d = 0 \quad (4.89)$$

where $p_1 = \sqrt{\lambda^2 - k_1^2}$, $p_2 = \sqrt{\lambda^2 - k_2^2}$, $N^2 = \epsilon_1 / \epsilon_2$, and d is the height of the substrate layer. This function defines the location of the poles for the EFIEs. By finding the λ_p

value (i.e., the pole of the background environment in the lambda plane) for which (4.89) is valid, the pole ξ_p can be found from

$$\xi_p = \pm \sqrt{\lambda_p^2 - \zeta^2} \quad (4.90)$$

Note, the operational frequency regime is assumed to be such that only a single background environment mode is propagating (i.e., only a single pole on the proper Riemann sheet).

Another singularity will arise when p_2 itself is zero. This occurs when

$$p_2 = \sqrt{\lambda^2 - k_2^2} = \sqrt{\xi^2 - (k_2^2 - \zeta^2)} = \sqrt{\xi - \sqrt{k_2^2 - \zeta^2}} \sqrt{\xi + \sqrt{k_2^2 - \zeta^2}} = 0 \quad (4.91)$$

where $\lambda^2 = \xi^2 + \zeta^2$. Thus, branch point singularities exist at

$$\xi_b = \pm \sqrt{k_2^2 - \zeta^2} \quad (4.92)$$

where ξ_b represents the branch point singularity location in the ξ -plane.

The next concern is the location of the branch cut. The branch cut is what separates the top and bottom Riemann sheets ($\text{Re}(p_2) > 0$ and $\text{Re}(p_2) < 0$) in the complex ξ plane. In order to determine the branch cut trajectory, it is convenient to square the value for p_2 . The initial p_2 plane and resultant p_2^2 plane are depicted in Figure 34, with the top Riemann sheet depicted by the shaded region. By squaring the value for p_2 , the branch cut now lies along the axis where $\text{Im}(p_2^2) = 0$ and $\text{Re}(p_2^2) < 0$. Using this expression, the branch cut trajectory can now be determined.

It is important to keep track of which Riemann sheet the integral is being evaluated on in order to maintain continuity of the fields. If the integration path causes

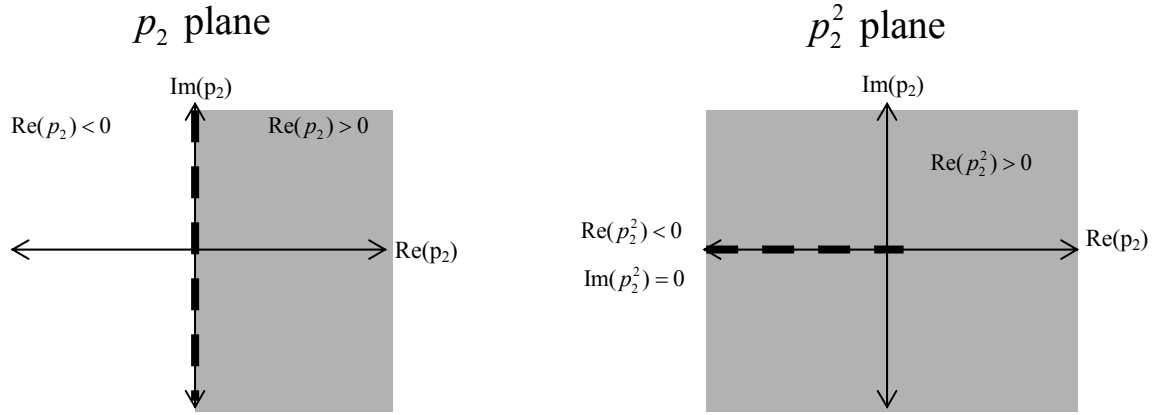


Figure 34: Riemann sheets in the complex p_2 and p_2^2 planes.

the interval to go from the upper Riemann sheet to the lower sheet (i.e., the integration path passes through the branch cut), this must be taken into account in order to evaluate the interval numerically. How this is accounted for in the numerical integration of the interval is discussed later in this section.

Solving for the branch cut results in

$$\begin{aligned}
 p_2^2 &= \xi_b^2 + \zeta^2 - k_2^2 = (\xi_r + j\xi_i)^2 + (\zeta_r + j\zeta_i)^2 - (k_{2r} + jk_{2i})^2 \\
 &= \xi_r^2 - \xi_i^2 + \zeta_r^2 - \zeta_i^2 - k_{2r}^2 + k_{2i}^2 + j2(\xi_r\xi_i + \zeta_r\zeta_i - k_{2r}k_{2i})
 \end{aligned} \tag{4.93}$$

Using $\text{Im}(p_2^2) = 0$ leads to

$$\xi_r\xi_i + \zeta_r\zeta_i - k_{2r}k_{2i} = 0 \quad \rightarrow \quad \xi_r = \frac{k_{2r}k_{2i} - \zeta_r\zeta_i}{\xi_i} \tag{4.94}$$

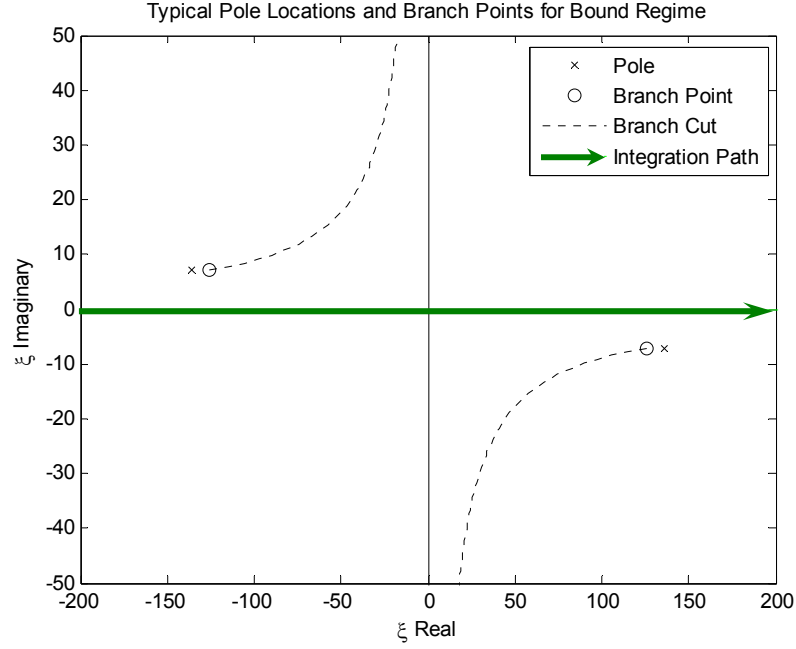


Figure 35: Typical pole and branch point locations for Bound Regime (lossy case)

Thus, (4.94) is the relationship between the imaginary and real components of the branch cut in ξ and describes a hyperbolic trajectory (i.e., the Sommerfeld branch cut path). The branch cut will start at the branch point ξ_b and stem off from that location as seen in Figure 35. This is a typical complex plane plot showing the location of the poles, branch points, and branch cuts for a microstrip structure operating in the *bound* regime. For this case, both the pole and branch point reside in quadrants II and IV.

The pole, branch point, and branch cut will move within the complex ξ plane as the material properties of the structure vary. Extreme care must be taken in understanding where these points are located for a given frequency before any integration in ξ can be performed. The pole and branch points transition between quadrants as the

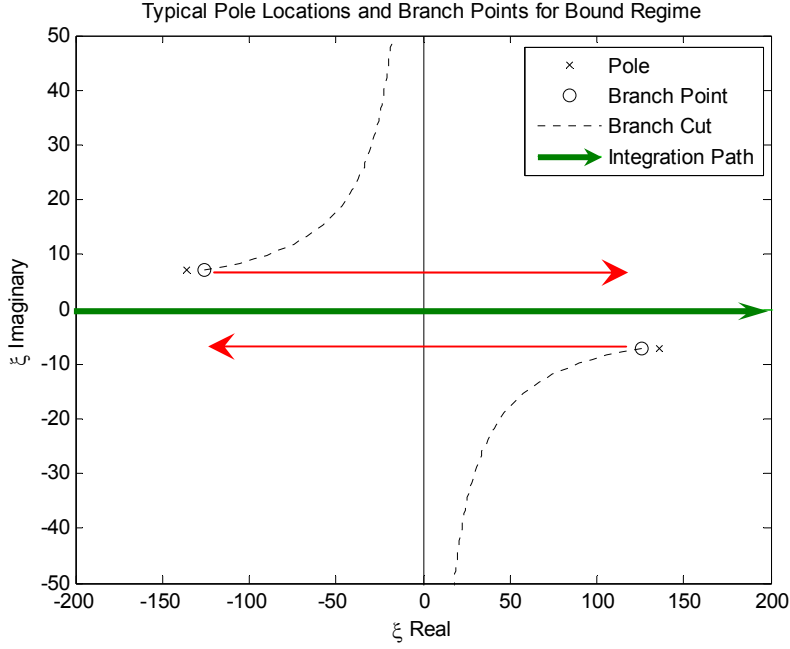


Figure 36: Migration path for the pole and branch points for Bound Regime (lossy to lossless)

permittivity of the sheet varies from lossy (large imaginary component) to lossless (no imaginary component) [13]. Sommerfeld states that when integrating in ξ , the integration path must remain on the same side of the pole and the branch point as they transition between quadrants in order to maintain physical continuity of the fields [15].

For the bound mode depicted in Figure 36, the pole and branch points will transition from quadrant II to I and from quadrant IV to III as the permittivity varies from lossy to a lossless. As such, neither set of points migrates across the real ξ -axis. Numerical integration can be performed along the real ξ -axis and will result in the Sommerfeld condition being met (this path is indicated with a green arrow in the figure).

Figure 37 shows the case where the pole and branch point are now associated with the radiation regime. Going from the lossy to lossless case, the poles and branch points

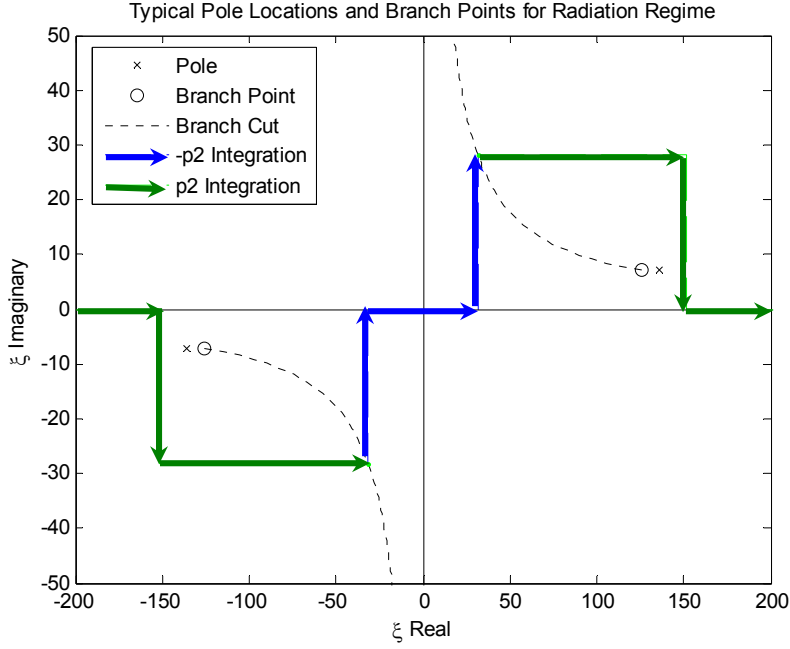


Figure 37: Integration path around typical pole and branch point locations in the
Radiation Regime (lossless case)

will migrate from quadrant II to III and quadrant IV to I. Because these points cross the real ξ -axis, the integration path must be deformed in order to remain on the same side of the pole and branch point. This results in the integration path shown in the figure (green and blue lines combine to give the total integration path) to be done numerically.

The indicated integration path goes above the pole and branch point (meets the Sommerfeld radiation condition), but must pass through the branch cut in order to do so. This is a violation of the Cauchy Integral Theorem [15] that states that the integration path can not pass through any singularity points in order to be valid, unless the branch cut violation is accommodated for, as discussed next.

In addition to having to meet the Sommerfeld radiation condition, there still exists the area of concern mentioned earlier. When the integration path crosses the branch cut, the value for p_2 now lies on the lower Riemann sheet ($\text{Re}(p_2) < 0$). In order to maintain continuity, $\text{Re}(p_2)$ must be set to $-\text{Re}(p_2)$ over this region (depicted as a blue line in Figure 37). Since all integration is being performed numerically, this can be done easily by setting $\text{Re}(p_2)$ to $-\text{Re}(p_2)$ along this interval and integrating on the lower Riemann sheet. However, doing this will result in growing waves over the interval. These growing waves will, thus, contribute to the leaky characteristics of the antenna [15].

As long as the Sommerfeld and Cauchy conditions are met and p_2 is properly handled numerically when the interval lies on the lower Riemann sheet, the integration path can be varied and the results of the integration will remain the same. However, before the elements of the MoM matrix can actually be integrated in ξ , a value for ζ must be determined. The following section will show how this is accomplished.

4.4.3 Newton Root Search

The last step in finding the propagation constants of the microstrip structure is to perform the integration of the matrix elements and solve for the determinant of the matrix in (4.46). A dilemma exists in that the EFIEs that make up the matrix can not be integrated in ξ until a value of ζ is determined, but ζ cannot be found without integrating the matrix elements to compute the determinant. The way around this problem is to perform a Newton Root Search of the matrix. The root search starts with an initial guess

for ζ and then iterates until a new value of ζ is found that causes the determinant to vanish within the specified tolerance.

The end result of performing the root search is a value of $\zeta = \zeta_p$ that represents the p^{th} natural mode propagation constant for the microstrip structure under investigation. As shown in Chapter 2, the real (β_z) and imaginary components (α_z) of ζ_p (also represented as ζ_z) and their relationship to each other versus frequency define the operating regimes for the antenna structure. The bandwidth of the radiation regime can directly be found from these values.

The next chapter will discuss specific cases of the modified THW antenna that were investigated and the resulting propagation constants for those cases. This data will then be used to perform a complex plane analysis to gain insight into how the material properties of the modified microstrip impact the movement of the pole and branch points and, thus, influence how the antenna radiates.

Chapter 5

RESULTS

5.1 Introduction

This chapter will present the results of the Method of Moments implementation discussed previously. Numerous material perturbations are made to the proposed microstrip antenna and the corresponding propagation constants and associated operational regimes are identified for each scenario using the TR, FDTD and MoM techniques. The results are compared and contrasted with the baseline antenna to identify conditions that lead to radiation bandwidth improvement. In addition, the advantages and fundamental limitations of each technique is compared and contrasted. Finally, a complex plane analysis of the pole and branch cut migration behavior versus frequency is discussed using the MoM results to gain a deeper physical understanding of the factors that define and influence the various operational regimes of the modified leaky-wave antenna.

5.2 Method of Moments Solution For The Baseline Microstrip Antenna

An MoM analysis of the baseline leaky-wave antenna (i.e., strip current only) is performed here for future comparison to the MoM analysis of the modified leaky-wave antenna (strip and volume currents). The baseline results are compared with those obtained from the TR and FDTD methods to ensure confidence in the MoM code.

In the baseline case (strip current only), $\varepsilon_3 = \varepsilon_1$ (see Figure 29), thus no volume current exists in Region 3. Under these conditions, the only boundary condition to be enforced is zero tangential electric field on the strip conductor, therefore the MoM matrix (4.46) reduces to (see previous chapter for surface observer – surface source interactions)

$$\begin{bmatrix} S_{mn} & T_{mn} \\ X_{mn} & Y_{mn} \end{bmatrix} \cdot \begin{bmatrix} d_n \\ e_n \end{bmatrix} = 0. \quad (5.1)$$

Thus, only the surface currents and respective Green's function of the background environment are driving the operation of the baseline microstrip structure.

In order to determine how well the Method of Moments predicts the propagation constants for the baseline Thiele half-width antenna, the results were compared to the TRC and FDTD data from Chapter 2. For comparison purposes, even and odd Chebyshev basis functions, as well as sinusoidal basis functions, were used in the MoM analysis to represent the surface currents of the baseline antenna. Chebyshev functions were selected because they are known to very accurately model the physical behavior of surface currents on the microstrip conductor [12, 13, 15, 16].

Given that this research will also model the electric fields in Region 3 for the modified antenna, it was intuitively decided that sinusoidal basis functions would also be investigated for the baseline antenna. Specifically, sinusoidal basis functions were chosen since they would adequately represent the surface current of the baseline antenna and, more importantly, do a much better job at modeling the actual field behavior in Region 3 for the modified antenna (weighted Chebyshev polynomials have edge singularities that are suitable for currents, but not for bounded fields). The sinusoidal

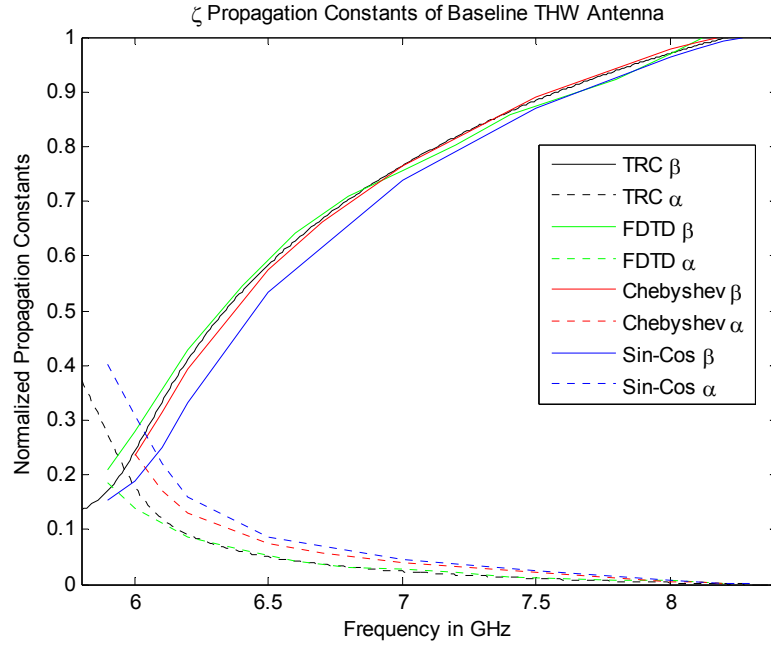
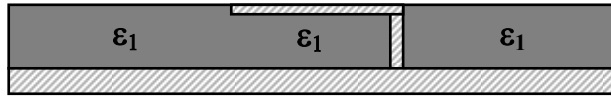


Figure 38: Propagation constants for the Baseline THW Antenna over the Radiation Regime using TRC, FDTD, and Method of Moments.

Table 6: Bandwidth of Baseline THW Antenna Using TRC, FDTD, and Method of Moments.



Method Used	Radiation Regime	Bandwidth	Percentage Bandwidth
TRC	5.96 to 8.22 GHz	2.26 GHz	31.88%
FDTD	5.87 to 8.12 GHz	2.25 GHz	32.17%
MoM Chebyshev	6.02 to 8.18 GHz	2.16 GHz	30.42%
MoM Sin-Cos	6.08 to 8.28 GHz	2.20 GHz	30.64%

basis functions sufficiently weaken the source-point singularity behavior in Region 3 discussed previously thereby improving convergence. A comparison of the propagation constant $\zeta = \beta - j\alpha$ using the MoM, TR and FDTD methods is shown in Figure 38.

It can be seen from Figure 38 that the Method of Moments does a very good job of matching the propagation constants for the baseline antenna with the same values found using TRC and FDTD. The percentage bandwidth found using the four methods is listed in Table 6.

At first inspection, it would appear that the Chebyshev basis functions do a better job matching the propagation constants found using TRC and FDTD than the results of using Sin-Cos basis functions. It is observed that the Sin-Cos curves are “shifted” in frequency to the right of the TRC and FDTD curves by roughly 100 MHz. However, looking closely at the results in Table 6, it can be seen that the Sin-Cos basis functions come closer to matching the TRC and FDTD bandwidth and percentage bandwidth values for the radiation regime. Given that the bandwidth of the radiation regime is maintained and that the cut-off frequency is within 100 MHz of the TRC and FDTD data by using sines and cosines, they are acceptable for use as basis functions for this research.

Additionally, as discussed previously, the Sin-Cos basis functions will do a better job than the Chebyshev functions at modeling the bounded field behavior within Region 3 of the modified antenna. This is due to the weighted Chebyshev functions having edge singularities that are excellent for modeling current behavior, but not for representing the fields within a volume. Note that this choice of weighting functions allows all spatial integrals to be computed in closed form, resulting in enhanced numerical efficiency.

5.3 Method of Moments Solution for the Modified Microstrip Antenna

The MoM was used to determine the propagation constants of several material perturbations of Regions 1 and 3 for the modified antenna as summarized in Table 7. The results of this analysis are shown in Figures 39 to 42. Table 8 summarizes the operating region of the radiation regime for the cases investigated (baseline THW antenna cases in **bold**) and compares the results to the corresponding TRC and FDTD data.

Looking at the summary of results in Table 8, the data obtained using the Method of Moments compares favorably to the results from the FDTD data, but varies greatly with the TRC data. The baseline case is the only situation where the TRC data matches the results from the Method of Moments and FDTD predictions. For the modified microstrip antenna cases, the data obtained using the TRC varies greatly from the other two methods. The TR method is not as robust of a method as FDTD and the Method of Moments. As discussed in Chapter 2, TR represents the microstrip structure as a transmission line system. In doing so, it does not take into account any y -varying fields nor the coupling and interaction of these fields with the x -directed fields and currents. These interactions are critical for determining the propagation constants of the modified structure. Thus, the TR technique in its present form is not deemed a valid method for predicting the propagation constants for a modified microstrip structure.

It can be seen in Table 8 how closely the Method of Moments results (Figures 39-42) compare with those derived from FDTD (Figures 23 and 24). In most cases, the bandwidth between the two methods only varies by 100 MHz or less. This is deemed to

be quite good, especially given that the baseline cases vary between them by 50 MHz alone.

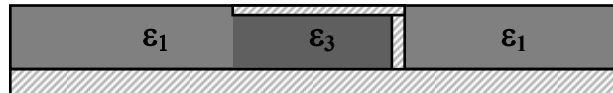
The real benefit of using the Method of Moments to predict the propagation constants for the baseline and modified structures over FDTD is that the Method of Moments does so at upwards of 200 times faster than FDTD. A typical data point (one propagation constant at one frequency) takes 3 minutes for the Method of Moments compared to upwards of 10 hours for FDTD on a PC (2.66 GHz Dual Intel ® Xeon X5355 with 8GB RAM).

Additionally, from the plots it can be observed how FDTD does not predict the alpha and beta values close to the cutoff frequency (as stated earlier in Chapter 2), but the Method of Moments predicts these values with ease.

All of the results obtained from the MoM analysis follow the same trends found in the FDTD data. The next section will discuss the physical meaning of these results and any design insight gained from them.

Table 7: Test Matrix for Modified THW Antennas Using Method of Moments.

ϵ_1	ϵ_3
1.03	2.33
1.33	2.33
2.33	2.33
3.33	2.33
1.03	1.33
1.33	1.33
2.33	1.33



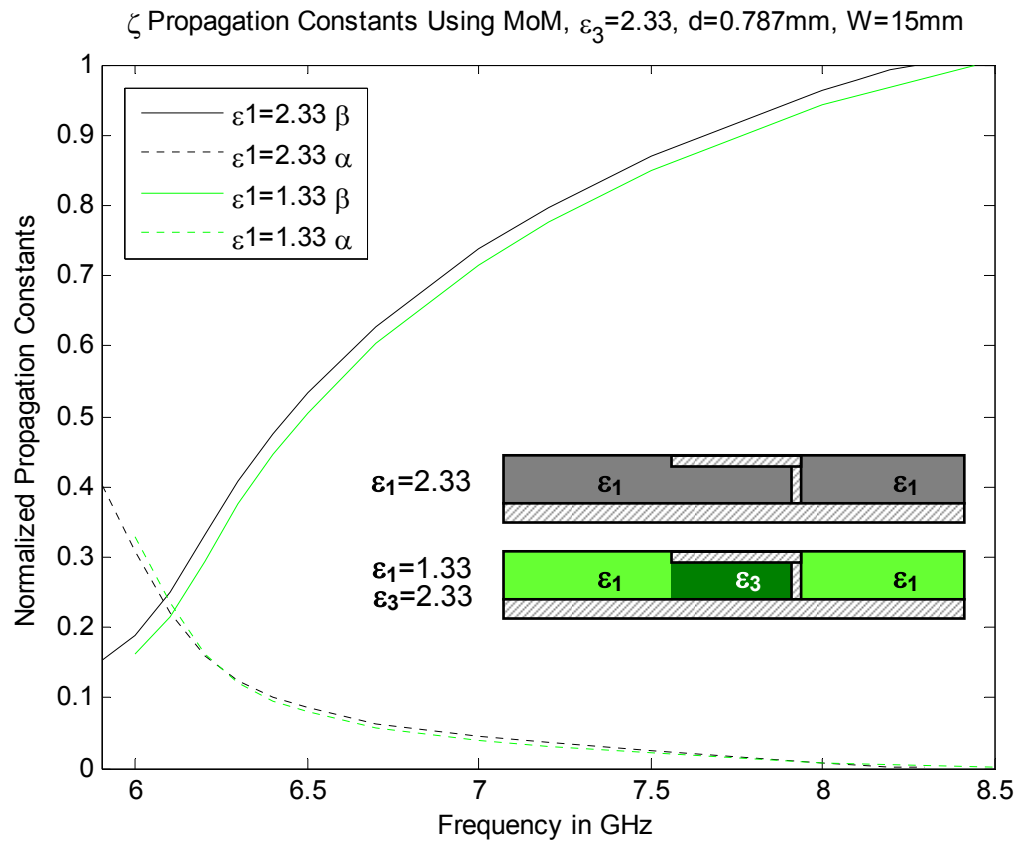


Figure 39: Propagation constants for radiation regime using MoM for $\epsilon_1=1.33$ and $\epsilon_3=2.33$.

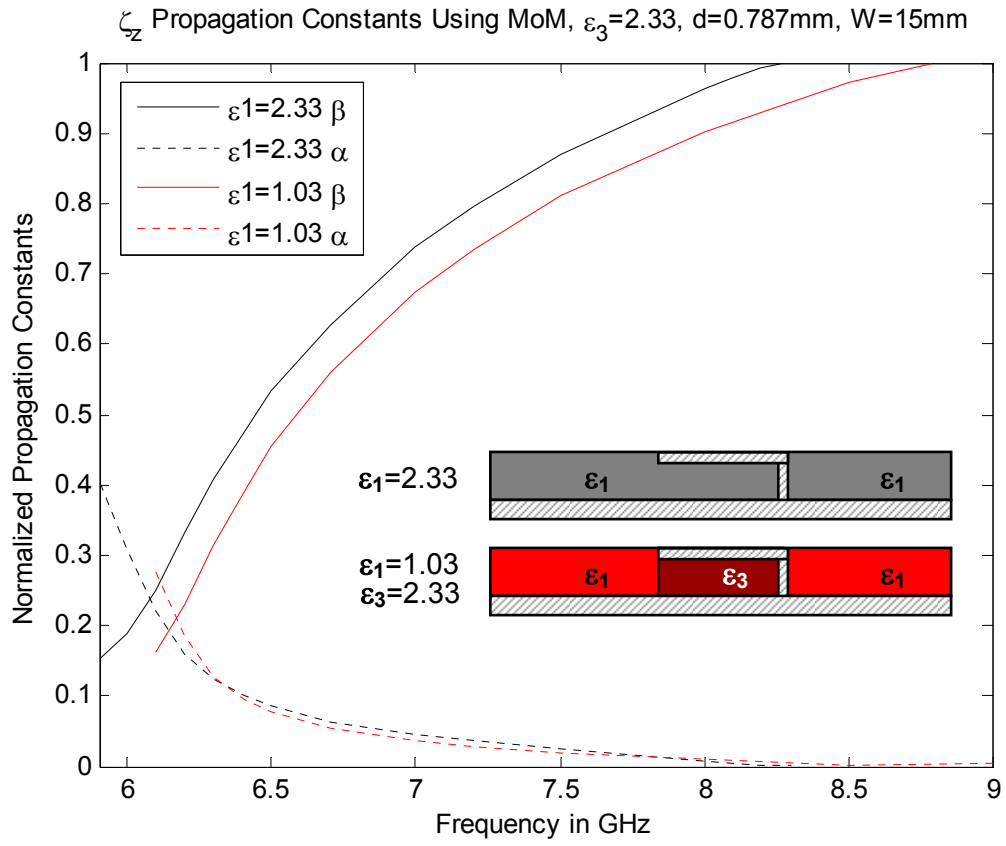


Figure 40: Propagation constants for radiation regime using MoM for $\epsilon_1=1.03$ and $\epsilon_3=2.33$.

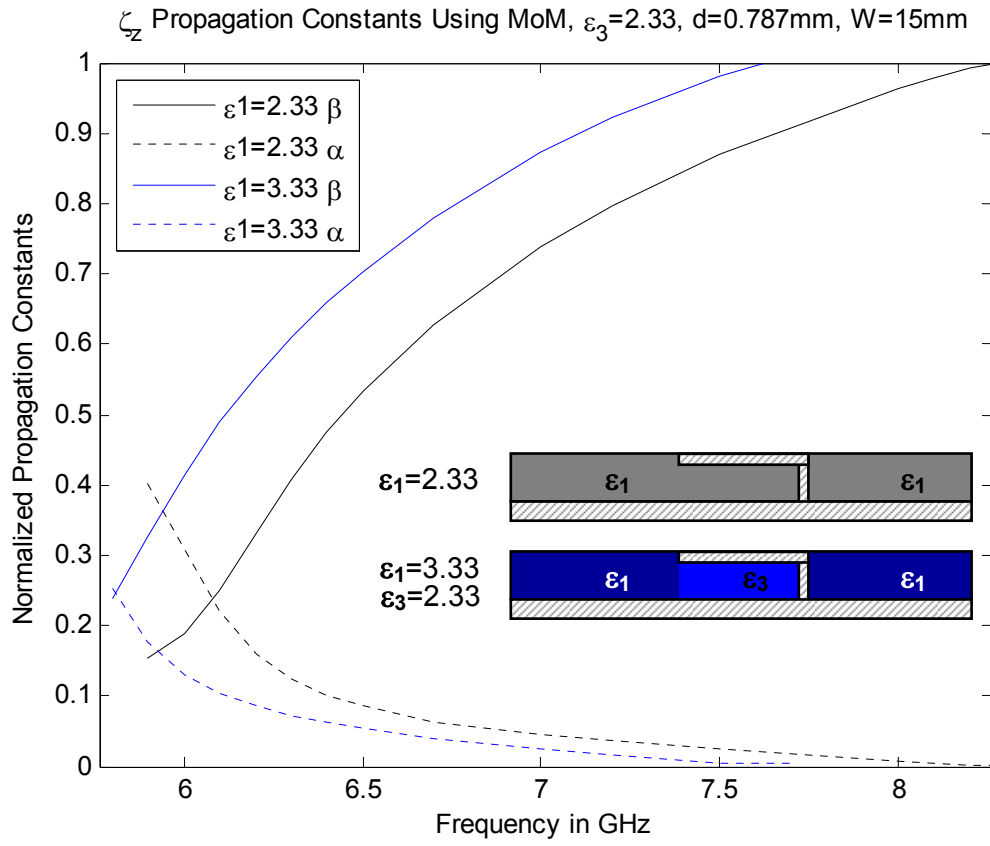


Figure 41: Propagation constants for radiation regime using MoM for $\epsilon_1=3.33$ and $\epsilon_3=2.33$.

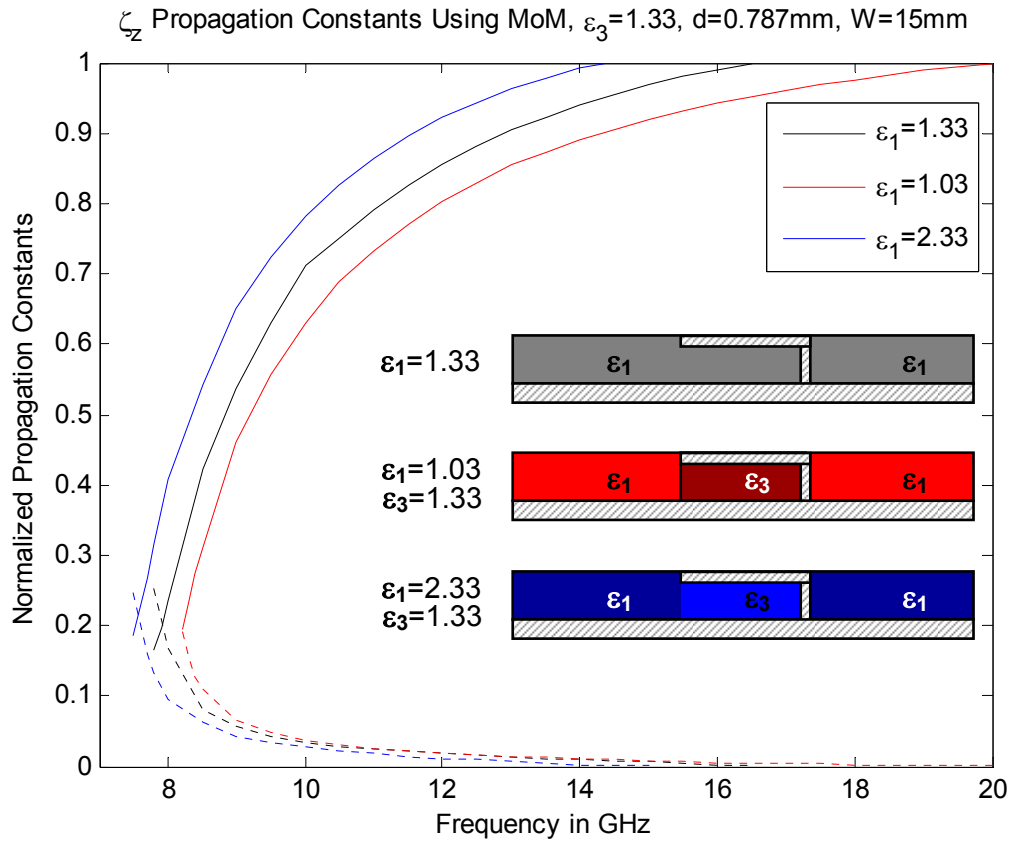
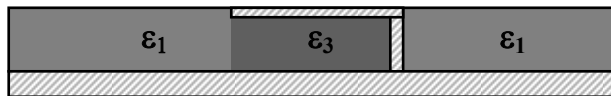


Figure 42: Propagation constants for radiation regime using MoM for $\epsilon_1=1.33$, 1.03, and 2.33 and $\epsilon_3=1.33$.

Table 8: Radiation Regime Bandwidth of Modified THW Antennas Using MoM, FDTD, and TRC.

		MoM	MoM	FDTD	FDTD	TRC	TRC
ϵ_1	ϵ_3	Bandwidth	Percentage Bandwidth	Bandwidth	Percentage Bandwidth	Bandwidth	Percentage Bandwidth
1.03	2.33	2.61 GHz	35.37%	2.7 GHz	36.24%	24.1 GHz	133.8%
1.33	2.33	2.33 GHz	31.98%	2.43 GHz	33.5%	6.55 GHz	71.0%
2.33	2.33	2.20 GHz	30.64%	2.25 GHz	32.17%	2.25 GHz	32.6%
3.33	2.33	1.81 GHz	25.88%	2.12 GHz	30.9%	1.41 GHz	21.2%
1.03	1.33	11.91 GHz	84.15%	9.54 GHz	75.89%	34.3 GHz	138.0%
1.33	1.33	8.59 GHz	70.38%	8.56 GHz	71.76%	8.7 GHz	72.3%
2.33	1.33	6.78 GHz	61.85%	7.25 GHz	65.76%	2.8 GHz	31.1%



5.3.1 Physical Insight From Radiation Regime Results

The results obtained from the MoM analysis were in agreement with the data derived from the FDTD analysis discussed in Chapter 2 and provided a much quicker and simpler method to obtain them. This section will talk more in-depth to those results, as well as attempt to give a physical understanding of why the data behaved as it did.

Similar to what was stated in Chapter 2, the bandwidth of the radiation regime increases as the permittivity of the sheet ϵ_l is lowered and the permittivity of the material in region 3 ϵ_3 is held constant. The opposite also holds true where the bandwidth of the radiation regime decreases as the permittivity of the sheet ϵ_l is increased and the permittivity of the material in region 3 ϵ_3 is held constant.

Physically, this can be thought of in the sense that the microstrip structure (the strip conductor, region 3 dielectric, and PEC ground plane) operating in the first higher-order mode is generating fringe fields based on the frequency of the source (as discussed in Chapter 1 and shown in Figure 4). These fringe fields radiate out from the structure and couple with the PEC ground plane. However, to do so, they must penetrate the slab of the background environment. If this slab is of higher permittivity, it will be more difficult for these fields to do so (due to depolarization) than if the slab were of lower permittivity. Thus, for the cases where the permittivity of the sheet ϵ_l is lowered, it is easier for the fields to couple with the PEC ground plane and, in turn, radiate away from the structure.

For the extremely high permittivity case, the slab would more readily reduce the fringe fields from attaching to the ground plane. This would lead to little energy being

allowed to radiate from the structure, thus causing it to resemble that of a tightly-confined field within a slab waveguide.

For the case where region 1 is air, the fringe fields would freely attach to the ground plane as they decoupled from the antenna structure. With no blockage of these fields due to the slab, this would result in a virtually infinite bandwidth (i.e., no trapped surface wave would exist in this case, thus radiation is the dominant scattering mechanism).

Further investigation into the results listed in Table 8 and in Figures 39 and 42 shows the impact of keeping sheet permittivity ϵ_l fixed and varying the ϵ_3 values in Region 3. For the case where ϵ_l is fixed at 2.33 and ϵ_3 increases from 1.33 to 2.33 the cutoff frequency decreases from 7.6 GHz to 6.2 GHz and the bandwidth decreases from 6.8 GHz to 2.2 GHz. For the case where ϵ_l is fixed at 1.33 and ϵ_3 increases from 1.33 to 2.33 the cutoff frequency decreases from 8 GHz to 6.2 GHz and the bandwidth decreases from 8.6 GHz to 2.3 GHz. These results follow those found in Appendix B and Figure 62 for a baseline THW antenna with varied permittivity.

Thus, the propagation characteristics of the antenna are strongly influenced by ϵ_3 (cutoff frequency and bandwidth of radiation regime). The sheet permittivity ϵ_l then serves to shift these values from those determined by ϵ_3 . This makes physical sense since the fields in Region 3 are setting up within the volume due to the surface currents on the strip. The electrons on the strip are causing fields to couple with the PEC directly below the strip, but doing so within the material of permittivity ϵ_3 . The fringe fields that do not

directly couple with the strip conductor do so within Region 1 and, in doing so, are influenced by ϵ_l .

In addition to the MoM analysis providing a significant improvement in the regime of convergence and computational efficiency in evaluating the desired propagation constants, these results can also be utilized to gain a deeper understanding of the governing factors that dictate the various operational regimes of the modified antenna. This deeper understanding is primarily accomplished through an analysis of how the pole and branch point singularities in the integrands of the coupled EFIEs migrate in the complex plane as the operational frequency is varied. This complex plane analysis is discussed next.

5.4 Complex Plane Analysis of Poles and Branch Points

The results of the full-wave analysis (using the Method of Moments) to solve for the propagation constants of the modified microstrip structure were given in the previous section. This section will take those results and perform a complex plane analysis to investigate how the materials within the structure can influence and modify the radiation and propagation regimes.

As discussed in Chapter 4, the microstrip antenna being investigated in this research can operate in four distinct regimes: reactive, radiation, surface, and bound. Each regime is defined by the location of the propagation constants in the complex ζ plane. However, these values can also be translated to the complex ξ plane (i.e., the x-

directed propagation) where further insight can be gained into the radiation and propagation characteristics of the antenna.

Using the values for ζ_z from Figures 39 to 42, combined with (4.90) and (4.92), the resultant pole and branch point singularities in the complex ξ plane are shown in Figures 43 to 53.

To understand these plots, start with the baseline THW antenna analyzed in Figure 43. The plot shows the location of the pole and branch point as the frequency is increased from 2 GHz up to 20 GHz. Starting in the lower right-hand corner, this represents the location of the pole and branch point at 2 GHz (reactive regime). Both points lie virtually on top of one another at this frequency and move to the left as the frequency is increased.

When the frequency reaches 5.97 GHz, the cut-off frequency (where $\alpha_z = \beta_z$) for the radiation regime is encountered and is highlighted in the figure. It is interesting to note that nothing “extraordinary” is seen in the curves at this point, even though it is considered a hard cross-over point between the reactive and radiation regimes. The poles and branch points continue to move in a straight line towards the imaginary ξ axis as the frequency transitions from the reactive regime to the radiation regime, with no distinctive transition. It is a common misconception within the leaky wave community that the poles and branch points shift from one quadrant in the complex plane to another at this point in frequency. This is not the case, as seen in the figure.

The two curves continue moving to the left along the same path, with the imaginary component of each point being very close to zero. When the frequency

reaches the end of the radiation regime (8.2 GHz on the plot), the curves stop moving toward the origin and now turn upward and towards the imaginary ξ axis. Figure 44 shows a close-up view of this transition region (the end of the radiation regime and the start of the surface regime). By 8.25 GHz, both points are very close to lying on the imaginary ξ axis.

As the frequency continues to increase in the surface regime, all of the remaining poles and branch points lie just off of the imaginary axis. When they finally do reach the axis, this is the start of the bound regime (11.5 GHz in the Figure 43).

Figure 45 compares the poles and branch points obtained using the TRC, FDTD, and MoM methods for the baseline THW antenna. All three cases start at roughly the same location, follow the same trajectory and then turn upwards at the same location. Although all three curves are not exact to one another, they are similar. The main point of this analysis was to show that there were not any pronounced differences between the three sets of data when analyzed in the complex ξ plane.

Figure 46 compares the three modified THW antennas with the baseline THW antenna using the MoM data in Figures 39 to 41. For all cases, the permittivity of region 3 is 2.33. It can be seen that as the permittivity of the slab is lowered (the green and red curves), the pole and branch point move closer to the real ξ axis than does the baseline curve (the black curve). If the permittivity of the slab is increased (the blue curve), it is observed that the pole and branch point move slightly further away from the real ξ axis as compared to the baseline curve. A closer view of this data can be seen in Figure 47, with only the radiation regime data shown.

For comparison purposes, the FDTD and TRC data can be seen in Figures 48 and 49, respectively. From these figures, the same trends can be seen in the curves as were found in the MoM results. One item of note is the reason why the FDTD curves are not as smooth as the MoM and TRC plots. This is an artifact of the process by which the data is taken from the FDTD computations, namely, small errors in the propagation constants translates to large variations in the complex ξ plane data. If the FDTD data were to be smoothed out, this would translate to smoother curves in the complex ξ plane. Despite this, the same trends can be seen as those found in the MoM and TRC data.

Figures 50 – 53 show the case where the permittivity of region 3 is 1.33. These cases again use the data obtained from the previous section and serve as a second set of data to validate the results of the 2.33 analysis.

One item of concern can be seen in the data. The data in Figure 50 (and in the close-up view of the same data seen in Figure 51) shows where the increased permittivity case (blue curve) actually moved below the baseline case (black curve). This is only observed in the MoM data. The FDTD and TRC data (Figures 52 and 53 respectively) both follow the same trends seen in the 2.33 data. It is unknown as to why this specific case does not follow the same trends as seen in all of the other cases and methods, but is likely due to numerical integration sensitivity.

From the figures, several trends can be observed:

1. For all of the cases, the pole and branch point locations are extremely close to one another. The branch point is located just to the left of the pole for all frequencies

within the reactive and radiation regimes. The pole and branch point, for a given frequency, will be further apart depending on the permittivity of the slab.

2. As frequency increases within the radiation regime, both the pole and branch point migrate to the left, towards the imaginary ξ axis.

3. Once the antenna enters into the surface regime, the pole and branch point split apart, with the branch point being the closer of the two to the imaginary ξ axis. Neither point will lie directly on the imaginary axis, but will move closer and closer as frequency increases within the regime. Only for a small fraction of the surface regime does the pole and branch point not lie close to the imaginary axis. This occurs at the point where the antenna goes from the radiation regime into the surface regime. After this point, the pole and branch point are virtually located on the imaginary axis.

4. As the antenna moves into the bound regime, both the pole and branch point lie directly on the imaginary ξ axis. This is a direct result of the propagation constant being strictly a real value (i.e., no attenuation).

5. In the bound regime, the pole and branch point will continue to move further up the imaginary ξ axis as frequency continues to increase.

6. As the permittivity of the sheet decreases (and region 3 stays fixed), both the pole and branch point move closer to the real ξ axis.

7. As the permittivity of the sheet increases (and region 3 stays fixed), both the pole and branch point move further from the real ξ axis.

8. Regardless of the permittivity of the sheet, the pole and branch point are very close to one another for the entire radiation regime. It is only when the antenna enters the

surface regime (and the subsequent bound regime) that the pole and branch point separate in the complex ξ plane. This is also material dependent (background).

9. For all of the cases shown, the materials used were lossless. Because of this, all pole and branch point singularities stayed within quadrants I and III (not shown) as the antenna transitioned from reactive to radiation to surface to bound regimes. Any loss in the materials would push the points closer to the real ξ axis or potentially into quadrants IV and II, respectively, for the radiation regime.

5.4.1 Constraint Equation Analysis

The previous section looked at the poles and branch points in the complex ξ plane as they moved with respect to changes in frequency. Tracking the location of these points is critical in determining a valid integration path for the integrals involving the Greens function components of (4.46). From this, combined with using the Newton's method, the propagation characteristics of the microstrip structure can be computed.

Looking at the constraint equation of (1.28), there still exists one remaining variable that is critical in understanding the propagation characteristics of the structure: p_2 . The variable p_2 is tied to the y -directed propagation through the equations described back in Chapter 3, specifically as $e^{-p_2 y}$, where $p_2 = \sqrt{\xi^2 + \zeta_z^2 - k_0^2}$. Note, this crucial y -variation was not accommodated in the TRC analysis as previously discussed, and hence is an important contribution.

Using the values of ζ_z found previously, values for p_2 can be determined. Since p_2 is dependent on ξ (the variable of integration for the integrals involving the Green's

function components of (4.46)), there is not one value for p_2 for each frequency. The proper way to analyze p_2 is to look at the ξ integration path (previously described in Chapter 4) and highlight the regions during which the values of p_2 are imaginary. An imaginary value for p_2 will cause energy to propagate in y .

Figure 54 shows the values of p_2 as computed along the integration path used in this research (Figure 41 in Chapter 4) for three sample frequencies (6, 7, and 8 GHz shown). Note that the bulk of the values lie on, or extremely close to, the real axis. For these values, there is no contribution to propagation in the y -direction. However, a small collection of points reside close to the imaginary axis. These points are the ones that make up the radiation contribution for the antenna.

Figure 54 shows how these points move closer to the real p_2 axis as frequency increases. All of the other values for p_2 remain on, or extremely close to, the real axis. In order to simplify the analysis of p_2 across all values of ξ , only the small collection of points that contribute to the propagation (i.e., have a large imaginary component) will be tracked versus frequency. Figure 55 shows the results of doing this for the baseline THW antenna. For comparison purposes, the poles and branch points (in ξ) and propagation constant (ζ_z) are also shown. All values are normalized to k_0 .

The modified microstrip structure is shown in Figures 56 to 59. For all of these cases, $\epsilon_1 = 1.33$ and $\epsilon_3 = 2.33$. Figure 56 highlights which points correspond to 5 GHz (reactive regime); Figure 57 highlights the points at 6 GHz (cutoff of the radiation regime); Figure 58 highlights the points at 12.55 GHz (radiation-surface regime transition); and Figure 59 highlights the points at 32 GHz (bound regime).

From the figures, two interesting observations can be made:

1. While in the reactive *and* radiation regimes, there are values for p_2 that contribute to the propagation of energy in the y -direction. However, in the reactive regime, the corresponding values for ζ_z have a large imaginary component. Because of this, energy will not propagate in the longitudinal z -direction; thus, propagating waves are not supported in this structure and the antenna is considered reactive in nature. In the radiation regime, the corresponding values for ζ_z have an equal or smaller imaginary component (compared to the real component of ζ_z). Because of this, longitudinally propagating waves can be supported in the structure.

2. As frequency is increased, the values for p_2 that contribute to radiation get smaller. This continues until the points lie on the real axis, at which time there is no propagation in the y -direction. The frequency that this takes place at corresponds to the same frequency at which the real component of ζ_z equals 1. As described in Section 1.3.4, this is the end of the radiation regime. Since all energy is now bound within the substrate slab and only propagates in the x -direction, having no p_2 values with any imaginary component makes sense.

This section has shown how the y -directed radiation of the microstrip antenna structure is driven by a few values of p_2 along the path of integration. For these values, there exists a large imaginary component. This component, when tied with $e^{-p_2 y}$ provides the necessary propagation in the y -direction to radiate in the normal direction away from the surface. These values are directly tied to the material characteristics of the structure.

5.4.2 Conclusions from Complex Plane Analysis

Performing a complex ξ plane analysis of the propagation constants for the modified antenna has given several insights into how radiation may be promoted and bandwidth increased for the radiation regime of the structure. Lowering the permittivity of the background environment (i.e., the dielectric slab) showed the greatest impact for increasing bandwidth. The cut-off frequency of the antenna is still closely tied to the height and width of the metal strip and the permittivity of region 3; but the overall propagation characteristics of the structure are very much tied to the material that makes up the background environment of the leaky-wave antenna.

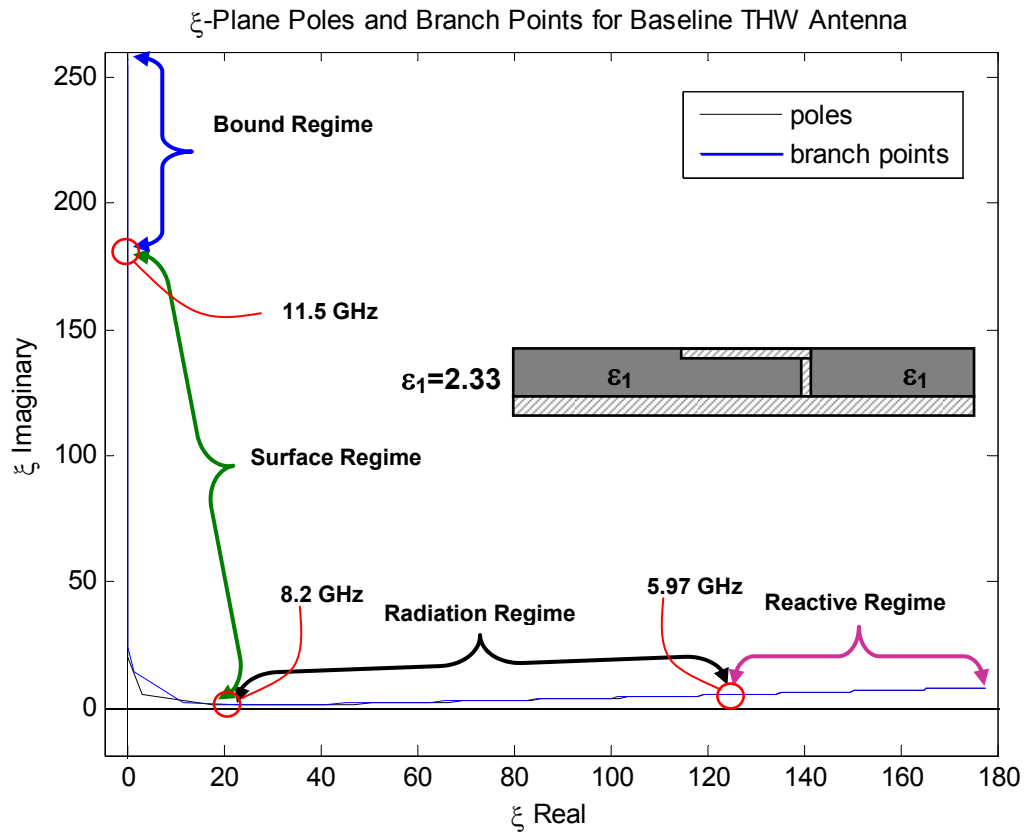


Figure 43: ξ plane poles and branch points for baseline THW antenna over reactive, radiation, surface, and bound regimes.

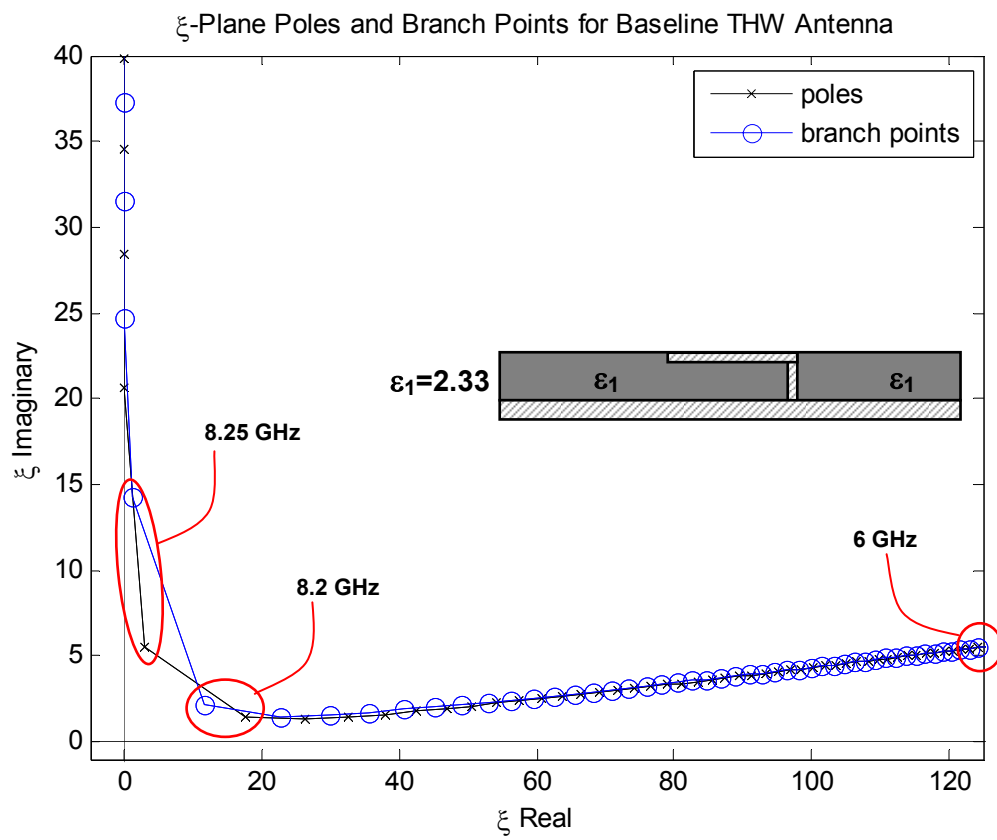


Figure 44: ξ plane poles and branch points for baseline THW antenna over radiation and surface regimes.

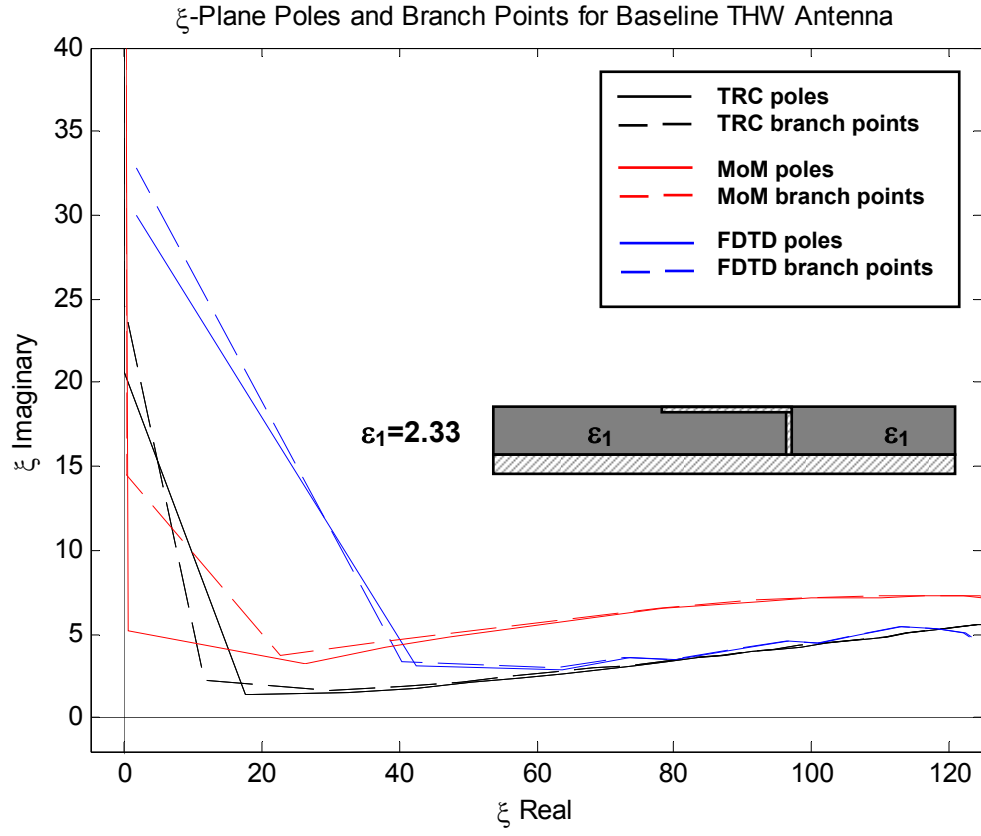


Figure 45: ξ plane poles and branch points for baseline THW antenna over radiation and surface regimes using TRC, MoM, and FDTD for $\epsilon_3 = 2.33$.

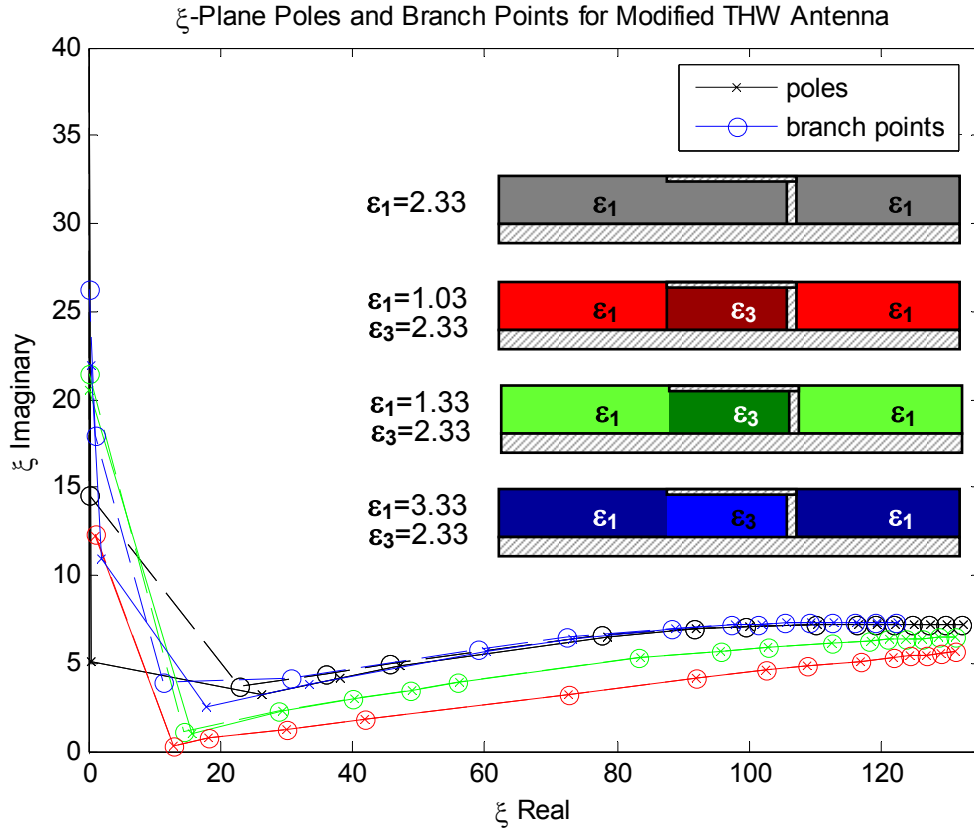


Figure 46: ξ plane poles and branch points for modified THW antenna over radiation and surface regimes using MoM for $\epsilon_3=2.33$.

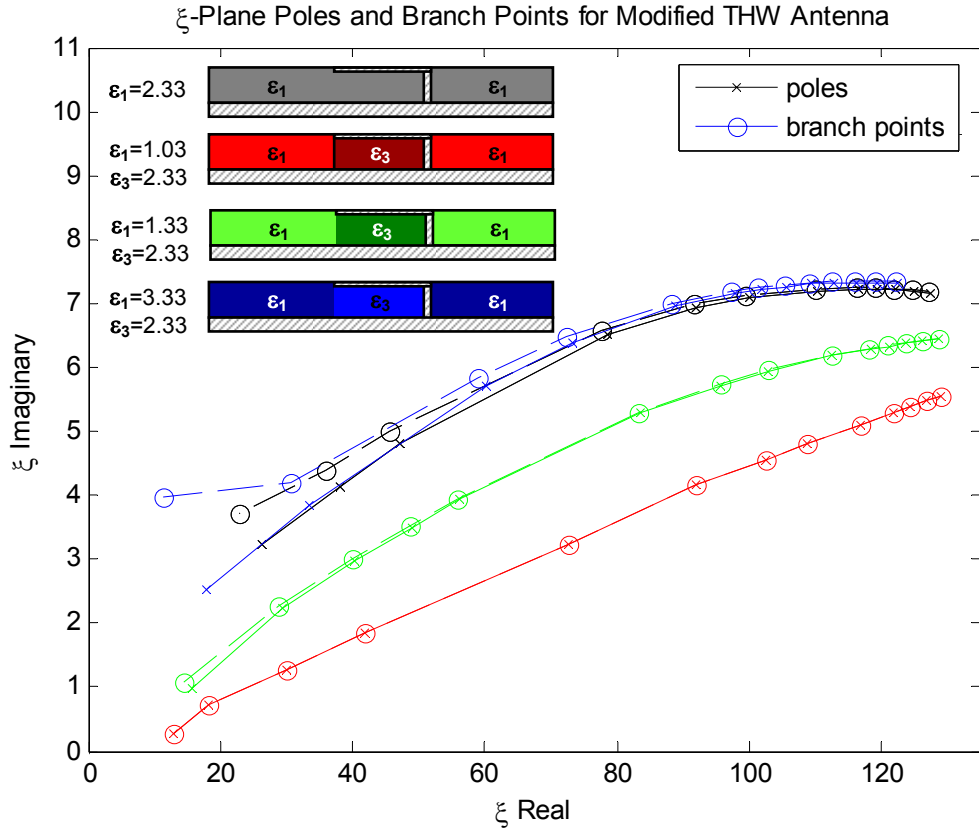


Figure 47: Close-up view of ξ plane poles and branch points for modified THW antenna over radiation regime using MoM for $\epsilon_3=2.33$.

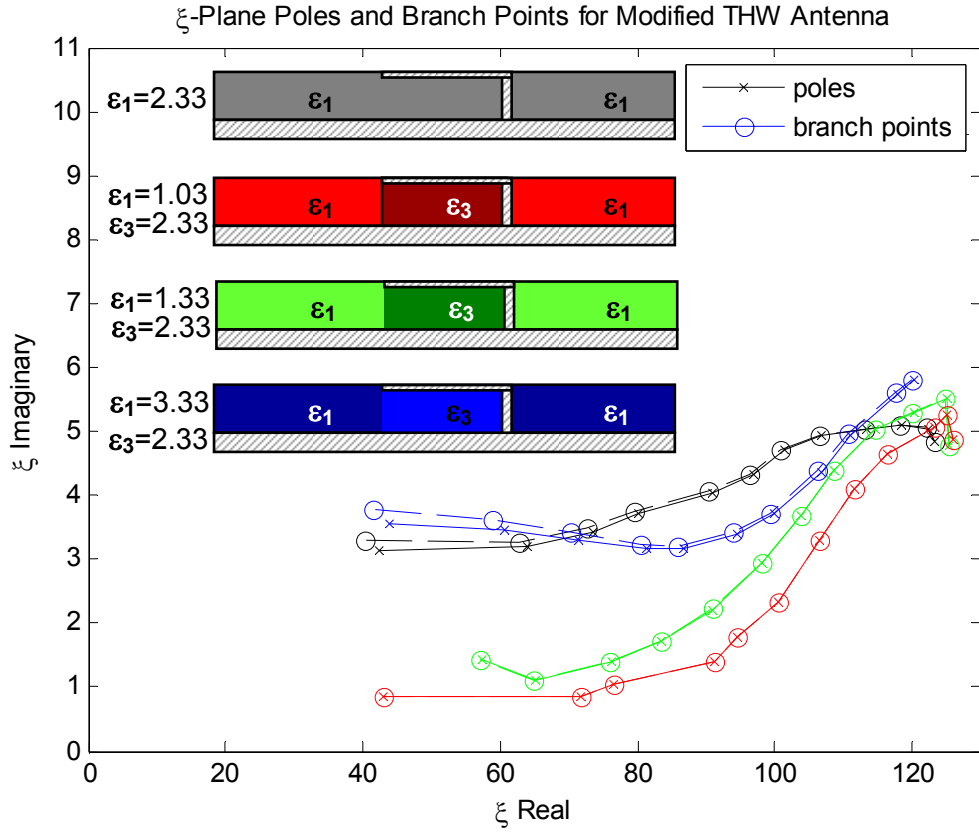


Figure 48: Close-up view of ξ plane poles and branch points for modified THW antenna over radiation regime using FDTD for $\epsilon_3 = 2.33$.

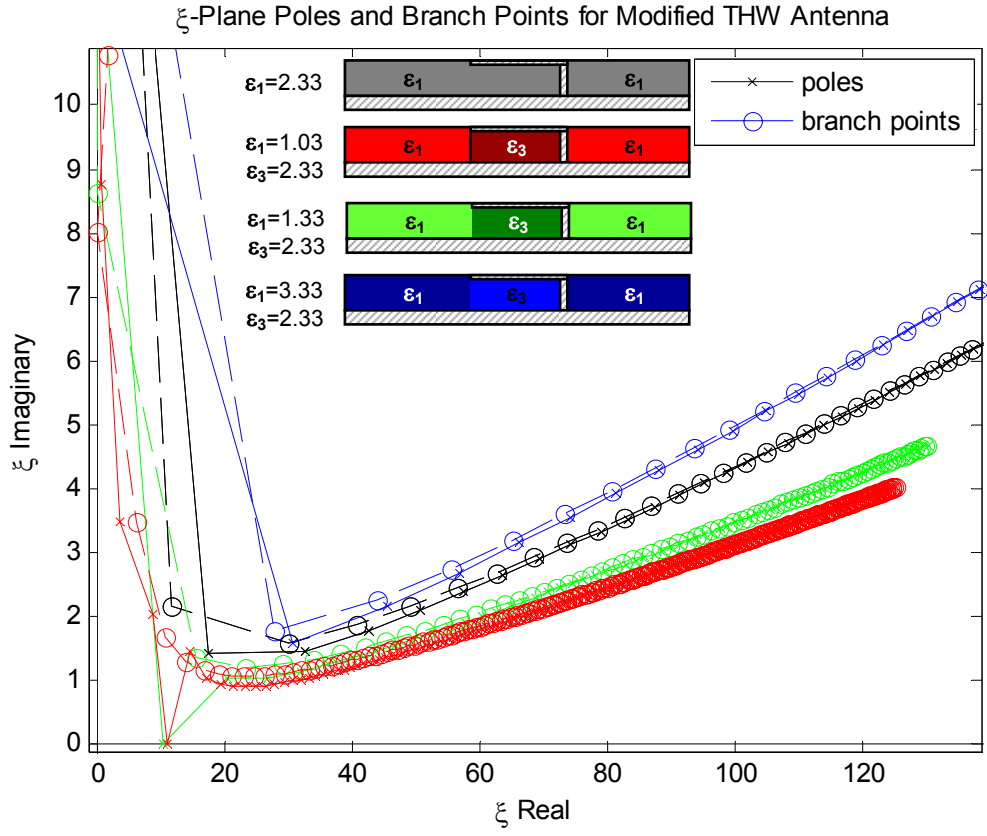


Figure 49: ξ plane poles and branch points for modified THW antenna over radiation and surface regimes using TRC for $\epsilon_3=2.33$.

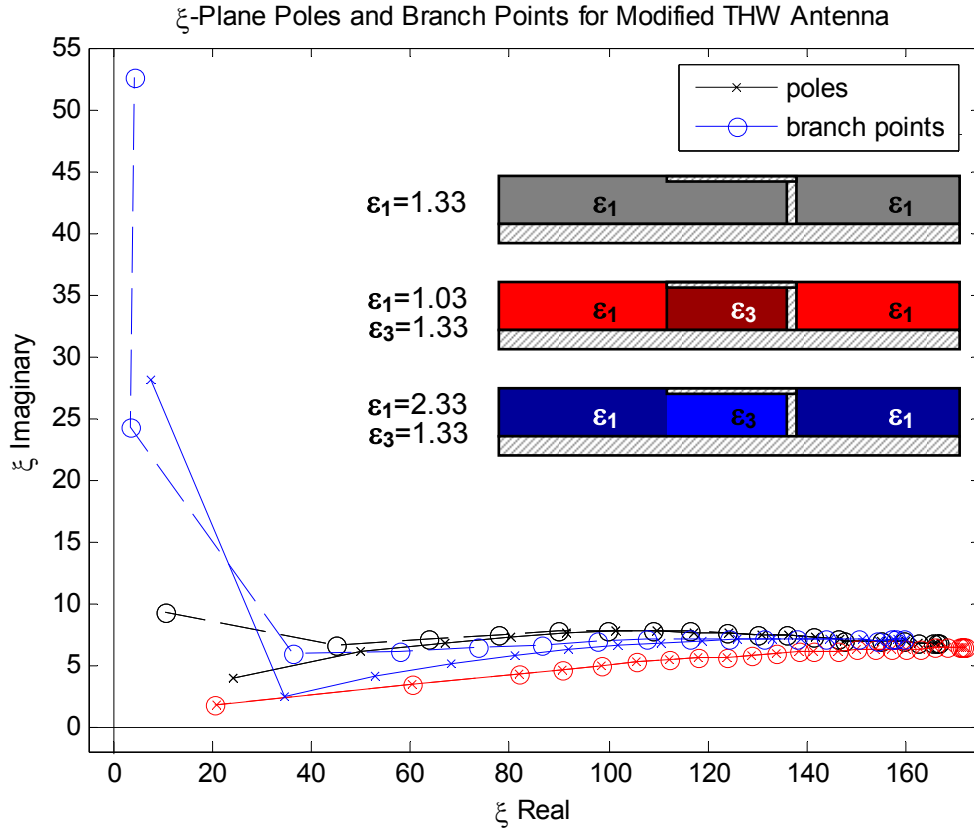


Figure 50: ξ plane poles and branch points for modified THW antenna over radiation and surface regimes using MoM for $\epsilon_3=1.33$.

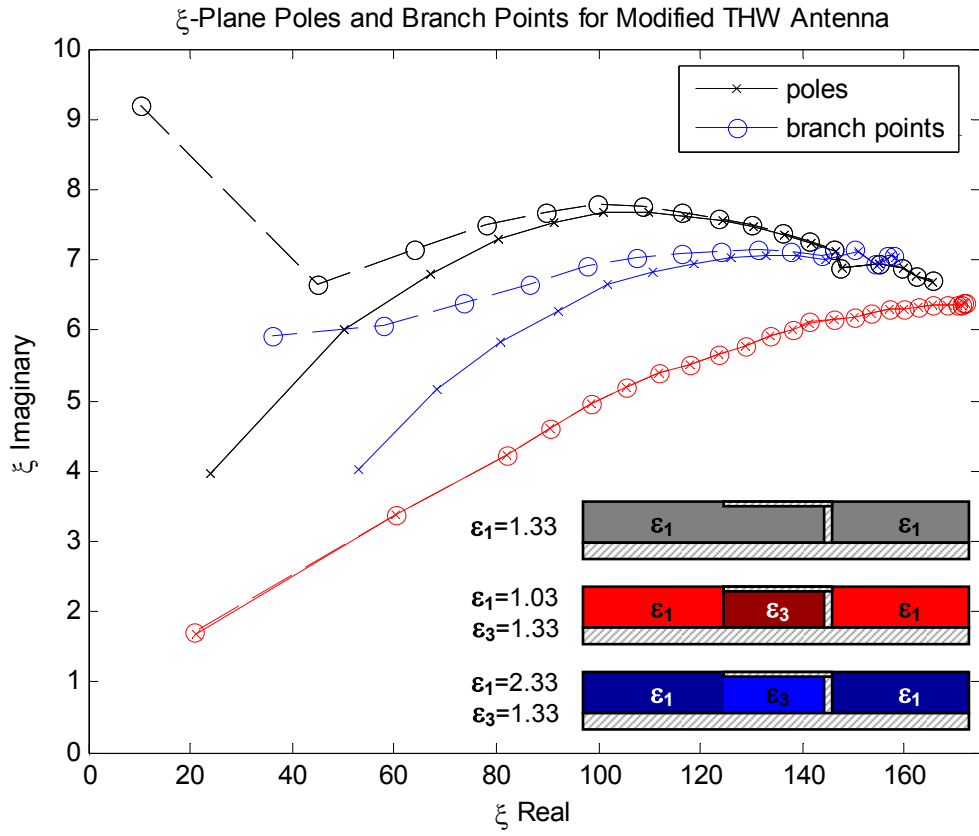


Figure 51: Close-up view of ξ plane poles and branch points for modified THW antenna over radiation regime using MoM for $\epsilon_3 = 1.33$.

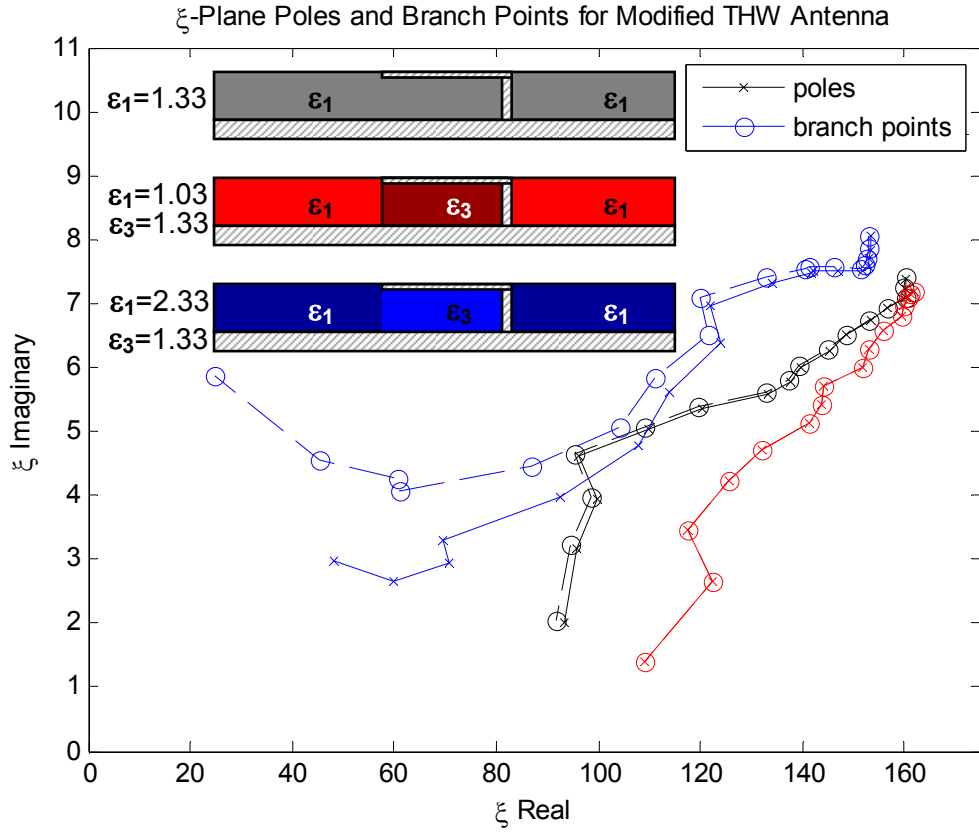


Figure 52: Close-up view of ξ plane poles and branch points for modified THW antenna over radiation regime using FDTD for $\epsilon_3=1.33$.

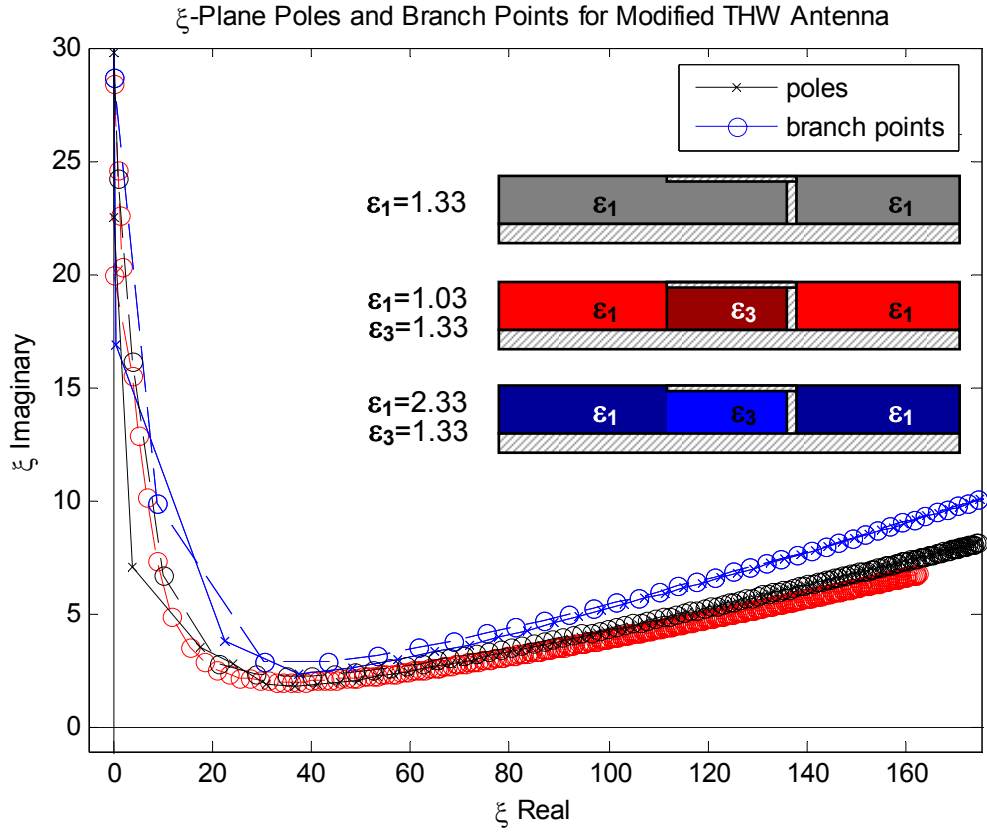


Figure 53: ξ plane poles and branch points for modified THW antenna over radiation and surface regimes using TRC for $\epsilon_3=1.33$.

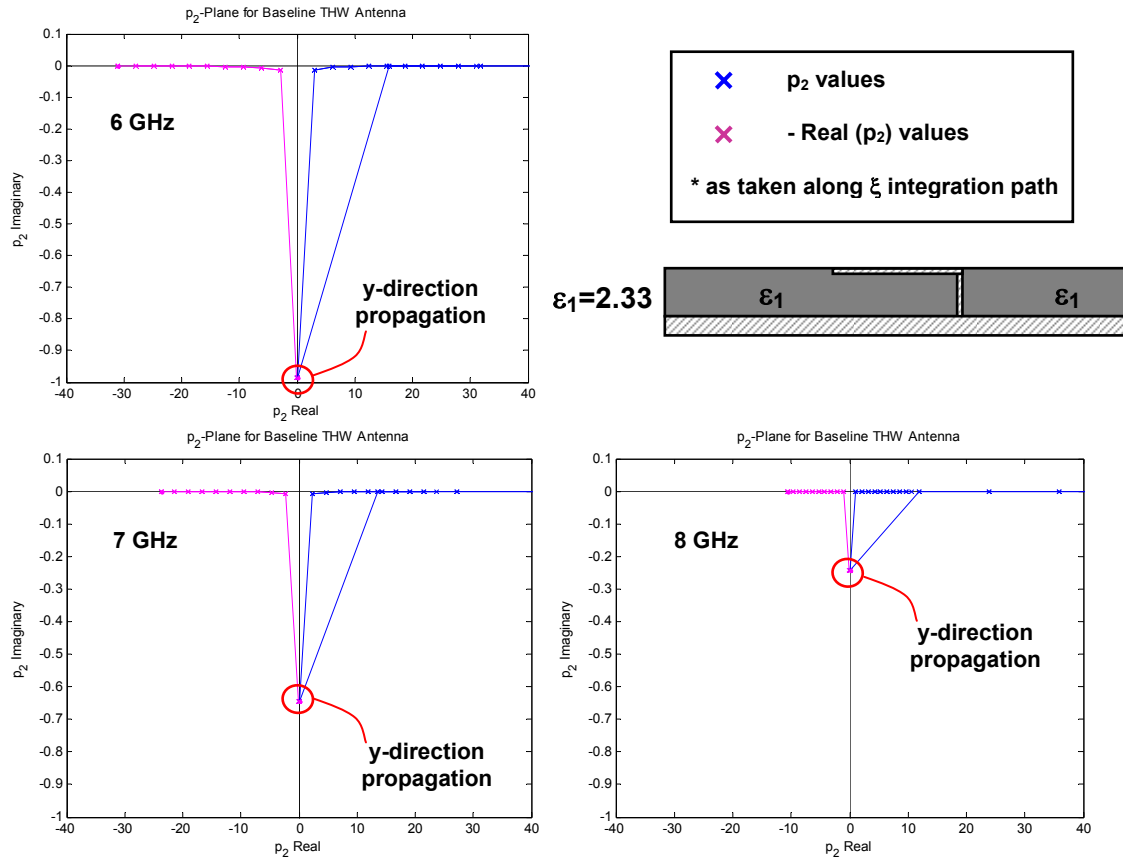


Figure 54: Complex p_2 -plane values over ξ integration path for baseline THW antenna, $\epsilon_l = 2.33$.

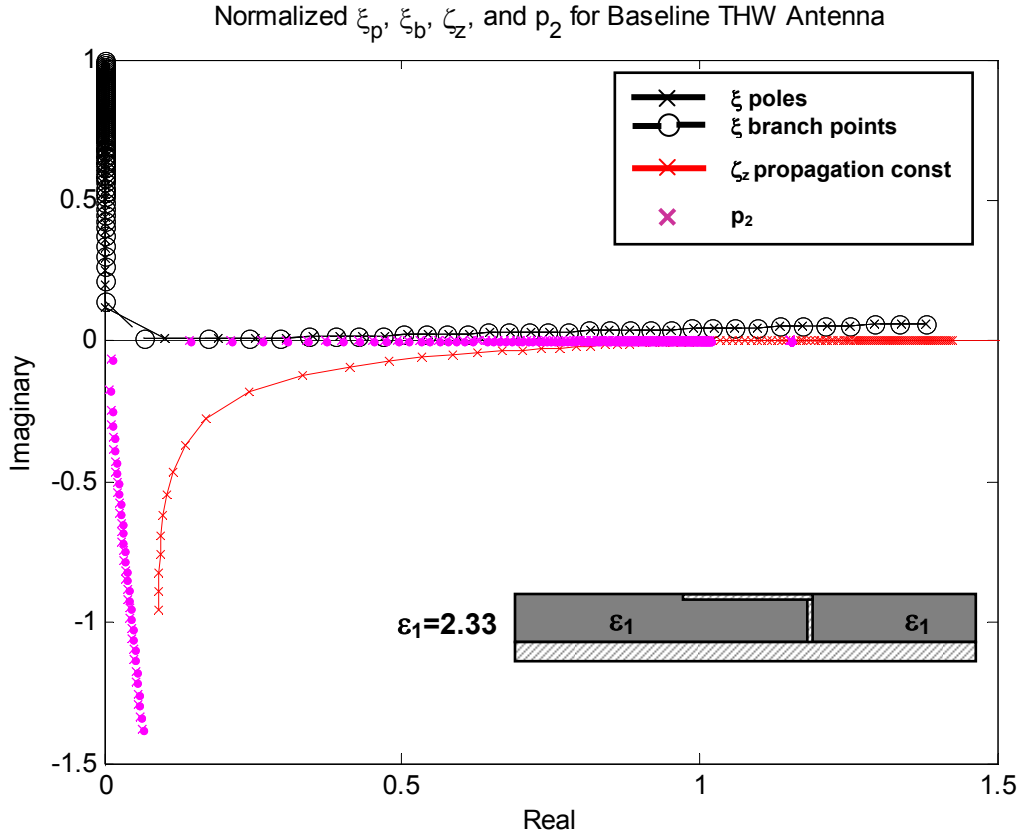


Figure 55: Complex ξ_p , ξ_b , ζ_z , and p_2 values for baseline THW antenna over reactive, radiation, surface, and bound regimes.

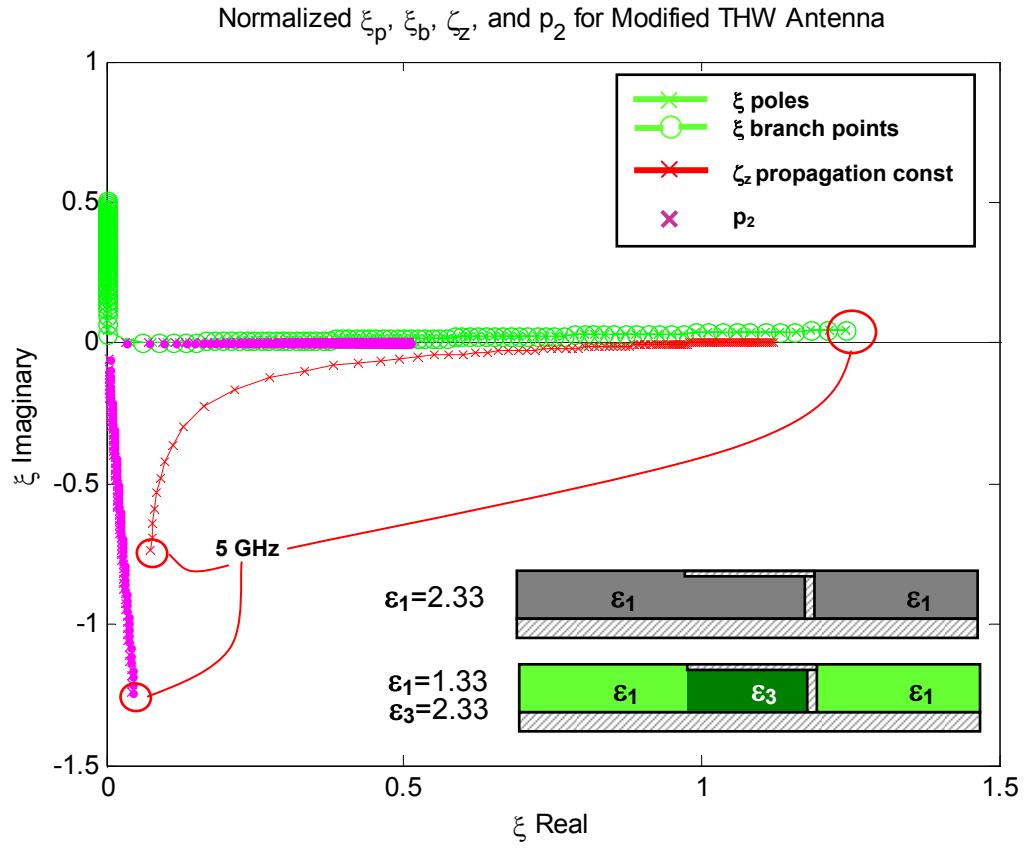


Figure 56: Complex ξ_p , ξ_b , ζ_z , and p_2 values for modified THW antenna ($\epsilon_l=1.33$ and $\epsilon_3=2.33$) over reactive, radiation, surface, and bound regimes with values at 5 GHz highlighted.

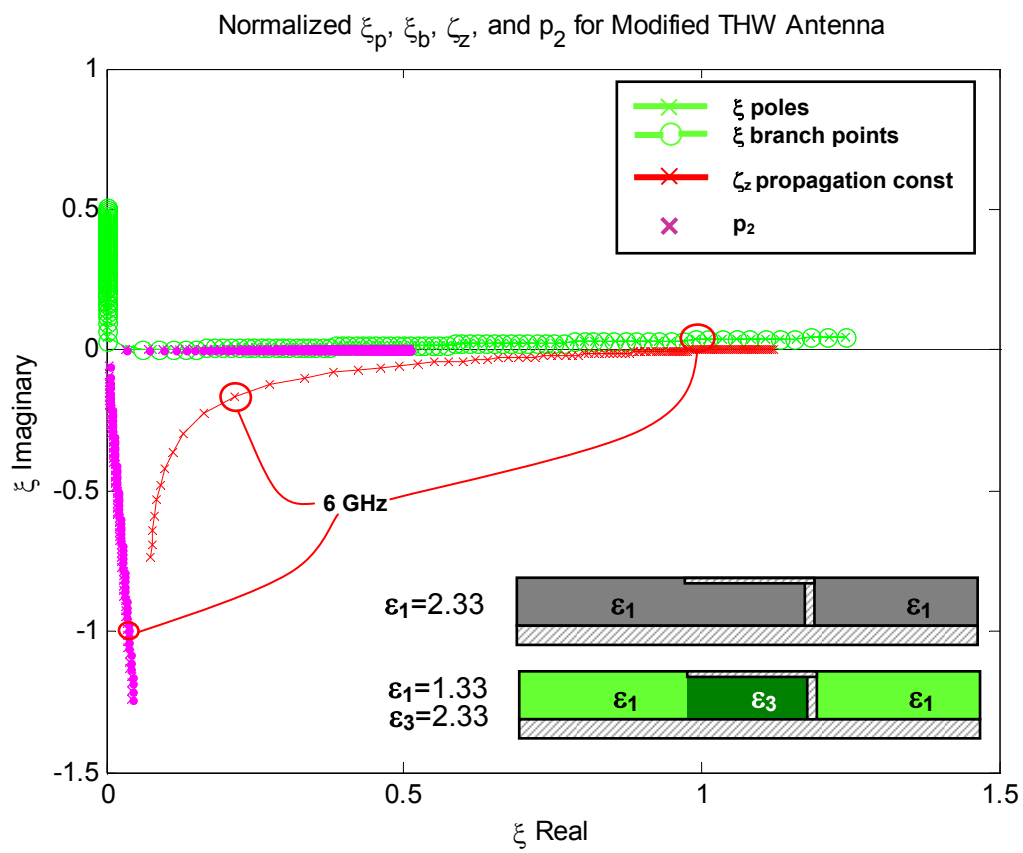


Figure 57: Complex ξ_p , ξ_b , ζ_z , and p_2 values for modified THW antenna ($\epsilon_l = 1.33$ and $\epsilon_3 = 2.33$) over reactive, radiation, surface, and bound regimes with values at 6 GHz highlighted.

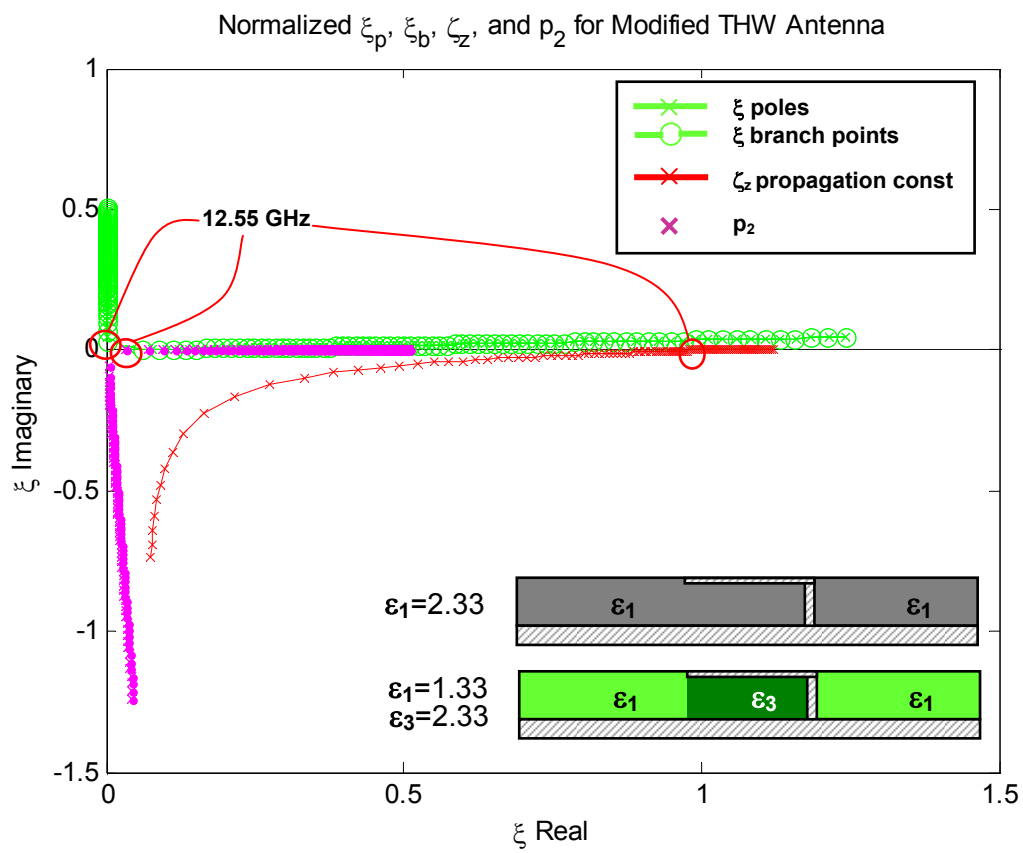


Figure 58: Complex ξ_p , ξ_b , ζ_z , and p_2 values for modified THW antenna ($\epsilon_l=1.33$ and $\epsilon_3=2.33$) over reactive, radiation, surface, and bound regimes with values at 12.55 GHz highlighted.

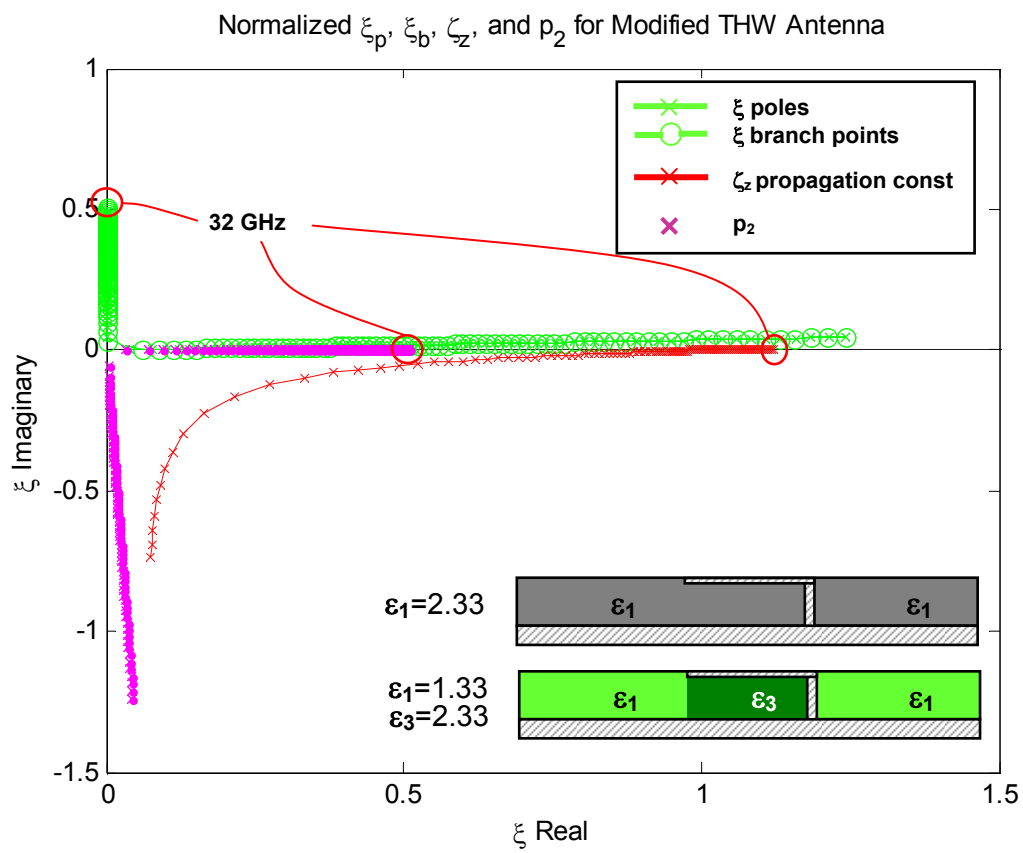


Figure 59: Complex ξ_p , ξ_b , ζ_z , and p_2 values for modified THW antenna ($\epsilon_l = 1.33$ and $\epsilon_3 = 2.33$) over reactive, radiation, surface, and bound regimes with values at 32 GHz highlighted.

Chapter 6

CONCLUSIONS

6.1 Introduction

Microstrip traveling-wave antennas radiate when the dominant mode is suppressed and the first higher-order mode is excited. One such microstrip is the Thiele Half-Width (THW) antenna, which operates from 5.95 - 8.2 GHz in this research. Increasing the bandwidth over which the THW antenna operates is desired, as is an increase in the attenuation constant, α_z , over this region. This dissertation sought to vary the material and physical properties of the THW antenna, including strip-width variations and modifications of the substrate layer, to achieve these improvements.

6.2 Overview of Research Effort

The microstrip traveling-wave antenna operating in the first higher order mode has been studied extensively within the research community over the last 30 years. This research effort looked to investigate a novel change to this antenna structure by varying the permittivity of the material under the strip conductor. The goal of modifying the antenna structure in this manner was to achieve increased bandwidth over the radiation regime.

In order to measure the effect of modifying the antenna in this manner, three different methods were implemented to extract the resultant propagation constants and, ultimately, the bandwidth. The first method used was the transverse resonance (TR)

method which represented the microstrip structure as a transmission line (incorporating strip width and material properties) in order to compute the transverse propagation characteristics. From these, the longitudinal propagation constants could be determined, along with the bandwidth of the radiation regime. This method was shown to accurately compute these values for the baseline THW antenna, but not for the modified cases studied.

The second method used was the finite difference time domain (FDTD) method. FDTD is a computational method for solving the time-domain differential form of Maxwell's equations directly and discretely using a space-time grid. By placing the microstrip structure into a rectilinear grid-space and discretizing it into a set number of finite elements that account for material and dielectric properties, the electric and magnetic fields for each element can be computed for a single time step. FDTD allowed for easy modifications to the microstrip structure and was able to compute the propagation constants and bandwidth easily and fairly accurately for these cases, as well as the baseline antenna. The major drawback to the FDTD method is the time required to compute the desired results, as well as its inability to accurately compute the propagation constants near the cutoff of the radiation regime.

In order to gain a greater understanding of the antenna and its four operating regimes, a full-wave analysis and Method of Moments (MoM) solution was implemented as the third method used in this research. The full-wave analysis used the background environment of the antenna as a basis to build the Green's function that define the principal and reflected waves within the structure. From these, insight into how the

various elements (electric fields and currents) interact with each other in order to influence the operation of the antenna was gained. The Green's function components were then used in a Method of Moments analysis that sought to drive the determinant of the MoM matrix to zero, thus revealing its eigenvalues (the longitudinal natural-mode propagation constants of interest). These constants were then mapped over the entire range of operating frequencies for the baseline and modified antennas, showing the effective increase or decrease in bandwidth.

Next, the propagation constants derived from all three methods used in this research were used to find the poles and branch points for those cases in the complex ξ plane. It was shown how these values changed their location in the complex plane based on variations to the permittivity in the region under the conducting strip.

Lastly, the propagation constants, poles, and branch points were used to find the complex values of p_2 that had an impact on the radiation of the structure. These points were shown to vary based on location within the radiation regime, as well as with material changes in the structure.

In the end, the results seen from modifying the THW antenna were approximately a 10% improvement in bandwidth for the test cases studied. Physical insight was gained as to what characteristics of the microstrip antenna drive propagation and radiation within the structure. By translating these results into the complex ξ and p_2 planes, it was shown how the materials within the microstrip structure shifted the location of the poles and branch points and promoted the radiation of energy.

In summary, the contributions of this work to the research community include:

(a) demonstrated bandwidth improvement of the microstrip traveling-wave antenna through material variations in the region under the metallic strip.

(b) clarified the common misconception that poles and branch points change quadrants within the complex ξ plane with frequency – they do not. The only time that these points will migrate from one quadrant to another is through a change of the material properties from the extremely lossy case to the lossless case. Determining how these points migrate when the materials go from a lossy case to a lossless case will determine the integration path required to meet the Sommerfeld radiation condition. Bagby wrote about this in his paper, but it is still commonly seen in the community the other way where points shift quadrants with changes in frequency [13].

(c) demonstrated how material variations move the poles and branch points in the complex ξ plane.

(d) demonstrated how material variations move the p_2 values that contribute to the radiation of the antenna structure.

(e) mapped out locations of ξ_p , ξ_b , ζ_z , and p_2 in their corresponding complex planes. Plotting all four of these sets of complex variables onto one complex plane plot has not been demonstrated in prior work – especially the identification of the elements of p_2 that contribute to the radiation of the structure and how they shift location with frequency.

(f) modified the TR method to look at the modified microstrip traveling-wave antenna.

(g) modified the FDTD method to look at the modified microstrip traveling-wave antenna.

(h) used the complex plane data to gain a better understanding of the reactive regime and what happens at the cut-off frequency to the radiation regime. There is no distinctive change in the poles, branch points, or radiation-contributing p_2 values when the antenna transitions from radiation to reactive regimes. The structure is reactive in this region based on the high attenuation in the z -direction (large α_z). This is not well documented in the community.

(i) combined a volume equivalence current with a surface current in order to determine the propagation characteristics of a microstrip traveling wave antenna.

6.3 Recommendations for Future Research

The results of modifying the materials under the top conductor of a microstrip antenna led to some bandwidth improvement of the radiation regime. Several suggestions can be made for future research that can potentially uncover greater levels of bandwidth improvement for the traveling-wave microstrip antenna.

Suggestions include:

- permeability variations in regions 1 and 3
- lossy materials to further drive complex ξ plane singularities closer to the real ξ axis
- tapered material inside or just outside of region 3
- tapered strip conductor along with material variations underneath in region 3

- include effects of non-perfect electric conductors ($\sigma < \infty$) for the ground plane, strip and shunt
- add a cover layer on top of microstrip
- perforated ground plane
- examine the characteristics of the EH2, EH3, EH4,... higher order modes
- develop TR method for a modified LW antenna based on a Weiner-Hopf technique (further investigating the TR method)

6.4 Conclusions

The impact of varying the material under the top conductor of a traveling-wave microstrip antenna was shown to be on the order of 10% bandwidth improvement. In addition, a greater understanding of the antenna and its transitions between regimes was gained from this research. MoM was shown to be an effective method for analyzing a structure such as the one used in this effort for the higher order modes of operation. The shortfalls of using FDTD and TRC to analyze such structures was also shown, as well as the benefits of using these methods.

In the complex ξ plane, the movement of the pole and branch point as the operating frequency varied from reactive to radiation to surface to bound regimes were depicted. For these lossless cases, the points were shown to remain within the same quadrants of the complex plane across all operating regimes. However, as the permittivity of region 3 was lowered (compared to that of the slab), the pole and branch

point were shown to shift closer to the real ξ axis. For these cases, this resulted in increased bandwidth for the antenna structure over the baseline case.

In the complex p_2 plane, the elements of p_2 (as ξ is integrated from $-\infty$ to ∞) that contribute to the radiation of the structure were plotted. It was shown how these points contain large imaginary and small real components in the radiation regime near cut-off. It was also shown how the location of these points move closer to the real axis (smaller imaginary component) as the frequency is increased. Upon transition into the surface regime, the points no longer contain any significant imaginary component. This corresponds directly to the antenna no longer having any radiation in the y -direction.

Future research is recommended in this area to find additional ways to increase the bandwidth of the radiation regime. Several suggestions were listed, most of which involved combining varying the permittivity of region 3 with other methods used within the research community to increase bandwidth.

Appendix A

TRANSVERSE RESONANCE METHOD

A.1 Introduction

This appendix is aimed at giving a more in-depth review of the Transverse Resonance Method used in Chapter 2 of the dissertation. The TRM is the basis for the Transverse Resonance Code used as one method to find the propagation characteristics of the traveling-wave microstrip antenna.

A.2 Transverse Resonance Method

The propagation constants of the THW microstrip leaky wave antenna have been found using the Transverse Resonance Method [5]. This method involves taking a cross-section (in the transverse plane) of the microstrip structure and representing it as a transmission line. The fields of this transmission line must satisfy the transverse wave equation

$$\nabla_t^2 \vec{e} + (k^2 - k_z^2) \vec{e} = 0 \quad (\text{A.1})$$

where $\nabla_t^2 = \frac{\partial^2}{\partial x^2} + \frac{\partial^2}{\partial y^2}$, $k^2 = k_t^2 + k_z^2 = \omega^2 \mu \epsilon$, and $k_t^2 = k_x^2 + k_y^2$. The factor k_t is called the *transverse* wave number and $k_z = \beta_z - j\alpha_z$ is the longitudinal (i.e., guiding-axis) wave number. This factor is also represented as ζ_z throughout this dissertation and are interchangeable with each other. The factor \vec{e} represents the electric field.

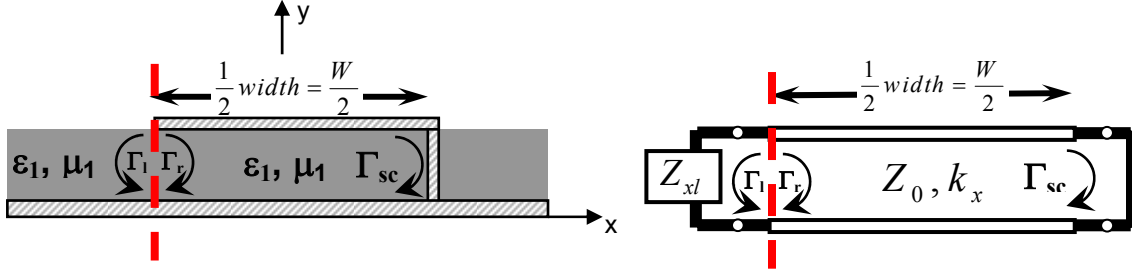


Figure 60: Representative transverse transmission line system for the baseline THW antenna

In general, solution of (A.1) subject to appropriate boundary conditions lead to an expression for k_t , thus the desired guided propagation constant k_z may be found using the constraint equation relation $k_z = \sqrt{k^2 - k_t^2}$. Alternatively, one may arrive at an expression for k_t by using impedances (ratio of tangential electric field to tangential magnetic field) and is referred to as the TR method. A specific example of the TR method is given next for the THW antenna.

Given any point within a transmission line of constant characteristic impedance (Z_0), the input impedance looking in the $+x$ direction must be equal in magnitude and opposite in phase of the input impedance looking in the $-x$ direction [9]. Knowing this, we can pick any point along our representative transmission line system and develop a relationship for the input impedances in order to solve for our propagation constants. Figure 60 shows the representative transmission line system.

Chang solved for the reflection coefficient at the junction of a parallel plate waveguide with an extended dielectric sheet using a Wiener-Hopf method. This point is represented as the red dashed-line in Figure 60. It was found that at this junction

$$\Gamma_l = e^{jX(\zeta_z)} \quad (\text{A.2})$$

where

$$X(\zeta_z) = X\left(\frac{k_z}{k_0}\right) = 2 \tan^{-1} \left(\frac{k_z}{k_x} \tanh \Delta \right) - f_e \left(-\frac{k_x}{k_0} \right) \quad (\text{A.3})$$

$$\Delta \cong \frac{k_z d}{\pi} \left\{ \left(\frac{1}{\varepsilon_1} - 1 \right) \left[\ell n \left(\sqrt{k_z^2 - k_0^2} d \right) + \gamma - 1 \right] + 2Q_0(-\delta_e) \right\} \quad (\text{A.4})$$

$$f_e \left(-\frac{k_x}{k_0} \right) \cong -\frac{2k_x d}{\pi} \left\{ \frac{1}{\varepsilon_1} \left[\ell n \left(\sqrt{k_z^2 - k_0^2} d \right) + \gamma - 1 \right] + 2Q_0(-\delta_e) - \ell n(2\pi) \right\} \quad (\text{A.5})$$

$$\delta_e = \frac{\varepsilon_1 - 1}{\varepsilon_1 + 1} \quad (\text{A.6})$$

$$Q_0(-\delta_e) = \sum_{m=1}^{\infty} (-\delta_e)^m \ell n(m) \quad (\text{A.7})$$

Additionally, the reflection coefficient can also be used to determine the admittance of the dielectric sheet as seen from under the parallel plate waveguide (Z_{xl}^{-1} in Figure 60).

This is given by the well known result

$$Y_a(\zeta_z) = Y_c \frac{1 - \Gamma_l}{1 + \Gamma_l} = -jY_c \tan[X(\zeta_z)/2] \quad (\text{A.8})$$

where $Y_c(\zeta_z) = (\varepsilon_1 / \mu_1)^{1/2} \eta_0^{-1}$ mho is the characteristic wave admittance within the transmission line and Y_a is the admittance looking out into the dielectric sheet [10] at the junction point.

Given the expression from Chang for the reflection coefficient of the microstrip structure at the edge of the top conductor looking out into the dielectric sheet [9], the input impedance can be written with respect to its reflection coefficient

$$Z_{xl} = Z_0 \frac{1 + \Gamma_l}{1 - \Gamma_l} \quad (\text{A.9})$$

Similarly, the input impedance at the right of the transmission line can be written as

$$Z_{xr} = Z_0 \frac{1 + \Gamma_r}{1 - \Gamma_r} \quad (\text{A.10})$$

At any point along the transmission line, the impedance looking to the right must be equal in magnitude, but opposite in phase of the impedance looking to the left. This is based on the need to keep continuity of the tangential fields within the line.

In order to simplify the computation, set the width to zero ($W = 0$). Using the transmission line theory stated above, the input impedances must now be equal in magnitude and opposite in phase at this junction [9], thus

$$Z_{xl} = -Z_{xr} \quad (\text{A.11})$$

Combining (A.9) and (A.10) with (A.11), results in

$$\frac{1 + \Gamma_l}{1 - \Gamma_l} = -\frac{1 + \Gamma_r}{1 - \Gamma_r} \quad (\text{A.12})$$

or

$$(1 + \Gamma_l)(1 - \Gamma_r) = -(1 + \Gamma_r)(1 - \Gamma_l) \quad (\text{A.13})$$

$$1 - \Gamma_l \cdot \Gamma_r - \Gamma_r + \Gamma_l = -1 - \Gamma_r + \Gamma_l + \Gamma_l \cdot \Gamma_r \quad (\text{A.14})$$

$$2 = 2\Gamma_l \cdot \Gamma_r \quad (\text{A.15})$$

$$\Gamma_l \cdot \Gamma_r = 1 \quad (\text{A.16})$$

The next step in the analysis is to allow for a finite W value. Equation (A.16) will still hold true at any point along the transmission line. If we choose to look at the far left

side of the transmission line (the red dashed line in Figure 60), we will have to translate the reflection coefficient on the right side of the transmission line (the short circuit Γ_{sc}) the length of the line to this location in order to determine the value for Γ_r . This resultant reflection coefficient is found using the well-known result

$$\Gamma_r = e^{-j2k_x \frac{W}{2}} \cdot \Gamma_{sc} = -e^{-jk_x W} \cdot 1 = -e^{-jk_x W} \quad (\text{A.17})$$

Conversely, Γ_{xl} does not have to be translated since it is located at the point of interest (at the location of the dashed line), leaving

$$\Gamma_l = e^{jX(\zeta_z)} \quad (\text{A.18})$$

Substituting the values for Γ_r and Γ_l into (A.16) and solving gives

$$e^{-jk_x W} \cdot e^{jX(\zeta_z)} = -1 = e^{j\pi} = e^{j3\pi} = e^{j5\pi} = \dots \quad (\text{A.19})$$

thus

$$X(\zeta_z) - k_x W = \pi, 3\pi, 5\pi \dots \quad (\text{A.20})$$

$$X(\zeta_z) - k_x W = \pm n\pi \quad n = 1, 3, 5, \dots \quad (\text{A.21})$$

where n represents the mode number. For the first higher-order mode, $n = 1$ is used since we are interested in the EH_1 mode. Thus, the expression: $X - k_x W = \pm \pi$ will be the basis for the Transverse Resonance Code (TRC) used to investigate the microstrip structures in this effort. By driving this equation to zero, the TRC will compute the corresponding transverse propagation constant (k_x) and, thus, the corresponding propagation constant for the microstrip structure ($k_z = \sqrt{\epsilon_{r1} \cdot k_0^2 - k_x^2}$). Note that the code does not require any vertical component of the propagation constant (k_y) as discussed next.

Given the relatively small thickness of the structure (0.787mm), the k_y contribution is assumed to be negligible. The thin plate spacing between strip conductor and PEC ground plane, acting approximately like a parallel plate capacitor in which the y -variation is essentially constant, the structure, in the spirit of the approximation, is essentially y -invariant. Hence, the k_y wavenumber is zero. Thus, we only need

$$k^2 = k_x^2 + k_y^2 + k_z^2, k_y \cong 0 \Rightarrow k_z = \sqrt{k^2 - k_x^2} \quad (\text{A.22})$$

A.3 Summary

This appendix has given an brief overview of the Transverse Resonance (TR) method and how it can be used to determine the propagation characteristics of a microstrip traveling wave antenna operating in the first higher order mode.

Appendix B

MICROSTRIP ANTENNA CHARACTERISTICS USING TRC

B.1 Introduction

This appendix is aimed at giving a more in-depth look into the baseline microstrip structure and how the propagation characteristics can be influenced by the width of the strip conductor and the permittivity of the substrate sheet. The modified microstrip structures found in Chapter 2 of this work are not investigated in this section.

B.2 Transverse Resonance Code

A copy of the TRC was obtained from its author, Dr Gary Thiele. As discussed earlier, the transverse resonance code (TRC) uses the expression for the reflection coefficient derived by Chang to compute the appropriate wave impedances at the junction of a parallel-plate waveguide with an extended dielectric slab. From these, the code is able to compute the propagation characteristics of the microstrip structure.

Upon obtaining the TRC, the first step was to validate the code with known results. To do this, the baseline THW antenna was used ($d = .787\text{mm}$, $W/2=7.5\text{mm}$, $\epsilon_r = 2.33$) and the results were compared with the known frequency range of the radiation regime (from 5.95 to 8.2 GHz) [5]. Figure 61 shows the results of the baseline TRC code for validity. The values in Figure 61 are identical to those found by Zelinski [5], who compared his values to those validated by Lee [91].

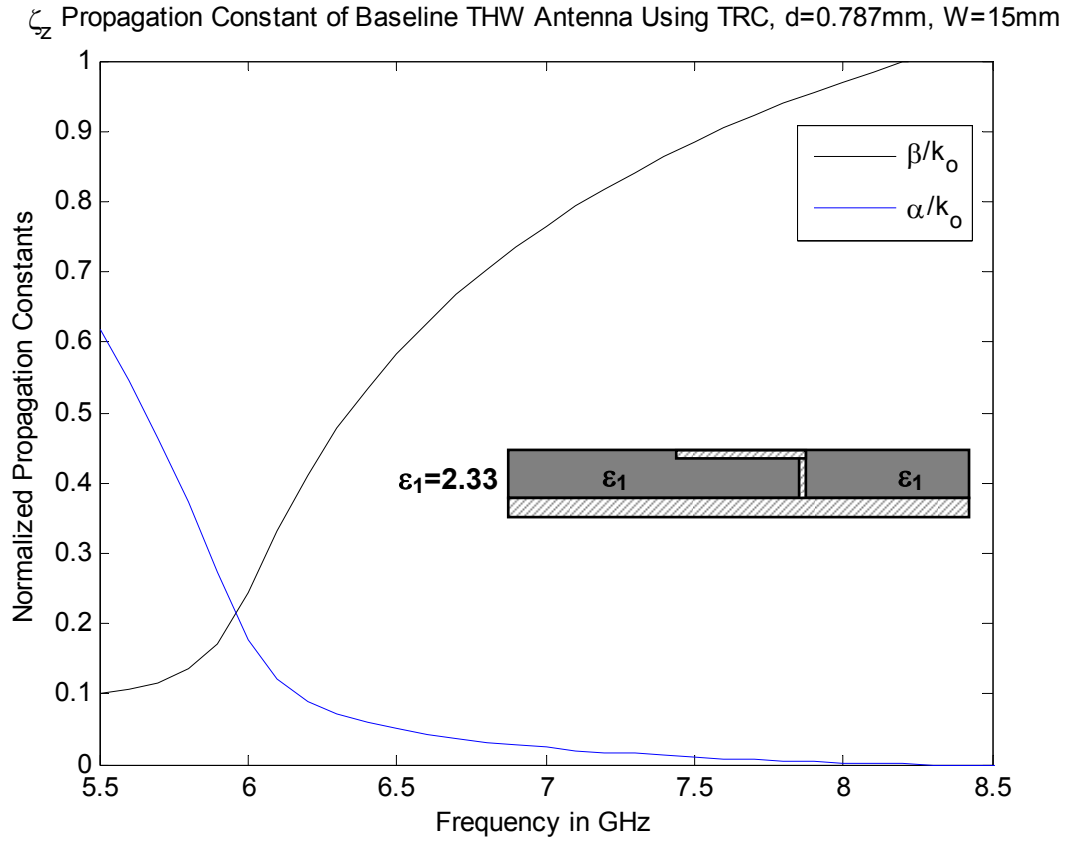


Figure 61: TRC approximation of leaky-wave propagation constants for baseline THW antenna.

In order to gain a better understanding as to how the width of the top conductor and the permittivity of the slab affect the cutoff frequency and bandwidth of the radiation regime, several microstrip structures were investigated. Table 8 shows the test matrix used to show the impact of varying the permittivity of the sheet. The permittivity values chosen represent a lower and a higher permittivity from the baseline case, as well as one that is essentially air (1.03). These results are shown in Figure 62. The widths listed for the microstrip antennas are for Thiele Half-Width antennas, thus their equivalent full-width values are double the widths listed.

Table 9: Microstrip Antenna Widths and Permittivities

Top Conductor Width (in mm)	ϵ_1
7.5	3.33
7.5	2.33
7.5	1.33
7.5	1.03

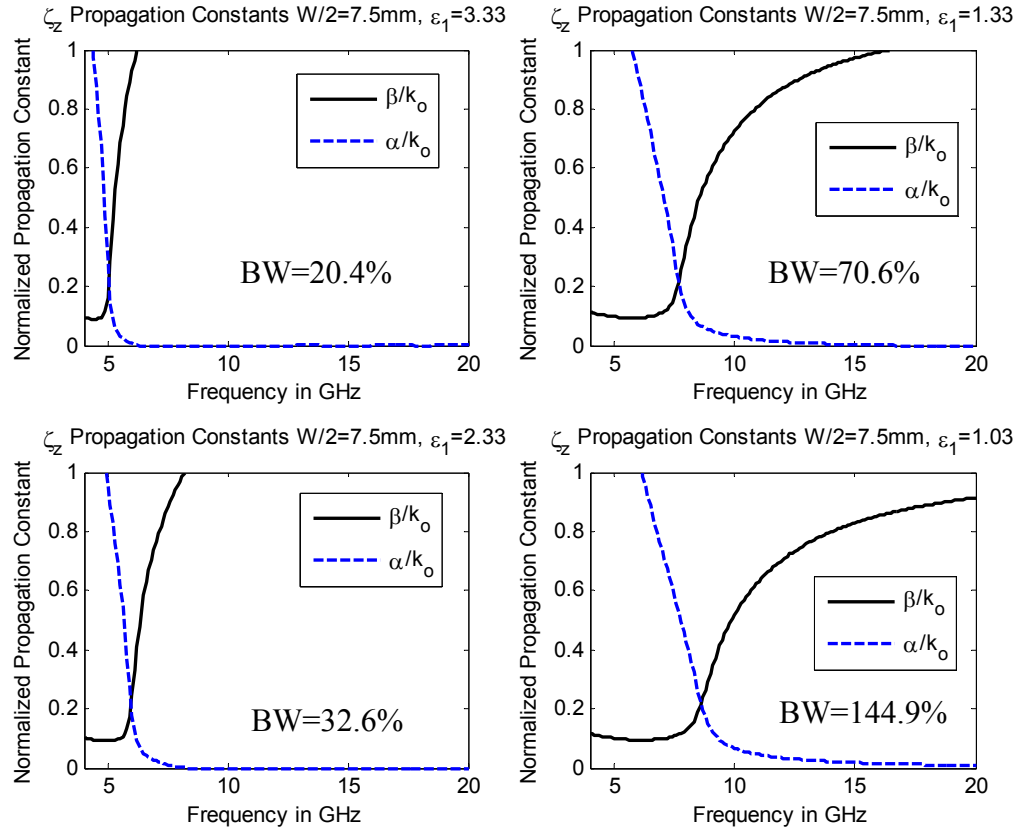


Figure 62: Multiple leaky-wave microstrip antennas

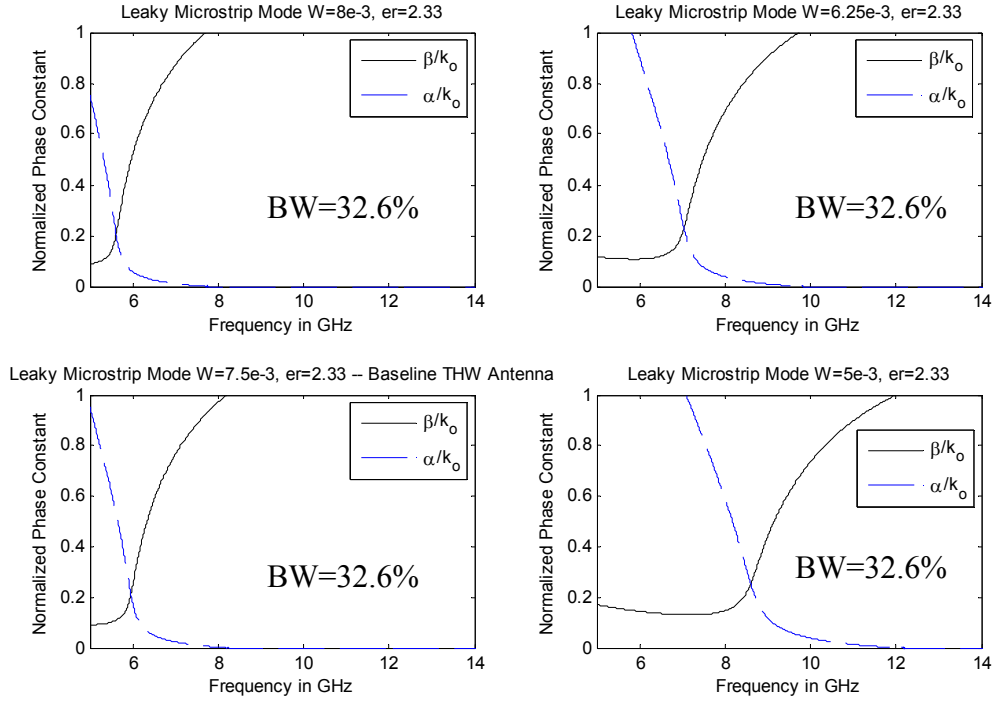


Figure 63: Leaky-wave antennas with varying conductor widths

In order to "normalize" the bandwidth measurements, it is common practice to use percentage bandwidth instead of absolute bandwidth when reporting this type of data [5]. Resultant bandwidth is given as: $BW\% = (f_{high} - f_{low}) / f_c$, where f_{high} is the frequency at which $\beta/k_0 = 1$, f_{low} is the frequency at which $\alpha = \beta$ and is also called the cutoff frequency for the radiation regime, and f_c is the center frequency of the radiation regime. It can be seen in Figure 62 that the resultant bandwidth increases as the permittivity decreases (and the opposite case holds true). For example, by lowering the relative permittivity from 2.33 to 1.33, the bandwidth increases from 32.6% to 70.6% - a 120% increase. The

fringe fields are more easily established for lower ϵ_l values since they aren't as tightly bound in the dielectric, thus increased $BW\%$ (i.e., enhanced radiation and leakage).

Given that the permittivity was varied for the cases in Figure 62, it was necessary to run another set of cases where the strip width was varied. Doing so would serve to isolate the impact of the strip width on $BW\%$. Figure 63 shows the results of this analysis. Changing the width of the top conductor has no effect on the $BW\%$, but serves to shift the cutoff frequency of the radiation regime. Increasing the width of the top conductor (while keeping permittivity constant) shifts the cutoff frequency downward, whereas decreasing the width increases the cutoff frequency. These effects are similar to changing the size of a rectangular waveguide or a parallel plate waveguide. As one increases the size of a waveguide, the cutoff frequency will be lowered. The larger opening allows for fields with larger and larger wavelengths to be set-up within the structure. If the opening of the waveguide is decreased, the cutoff frequency is increased. Only fields with smaller wavelengths can “fit” within the opening of the waveguide, thus ones with higher frequencies.

B.3 Summary

This appendix has given an overview of microstrip antennas operating in the radiation regime and showed the impact of changing the physical characteristics (width of strip conductor, permittivity of dielectric slab) of the structure. It showed how the bandwidth of the radiation regime would vary based on the permittivity of the slab. It also showed that the percentage bandwidth ($BW\%$) was not affected by changes in the

width of the strip conductor for a thin microstrip structure, but the cutoff frequency did move based on these changes.

Hopefully, from the analysis presented in this appendix, a better understanding of the microstrip structure and how the radiation regime can be influenced by the physical characteristics of the structure was gained by the reader.

Appendix C

MoM MATRIX ELEMENT EXTRACTION FROM EFIEs

C.1 Introduction

This appendix is aimed at explaining how the elements of the MoM matrix (4.46) are derived from (4.41) through (4.45). The MoM elements (4.47) through (4.71) are critical for showing the interaction between the various electric fields and surface currents in the structure. By understanding how these elements are extracted from the EFIEs of interest, it can easily be seen what fields and currents are driving the propagation characteristics of the antenna structure after each are numerically integrated.

C.2 MoM Implementation

Section 4.4 built the MoM matrix (4.46) that was used to find the propagation characteristics of the modified THW antenna structures. The matrix was made up of 25 elements (4.47) to (4.71), but it was not explained in detail how these elements were extracted from the EFIEs found in (4.41) through (4.45). This section will discuss one example (for (4.47)) in detail and leave the reader to extract the other 24 elements in similar fashion.

Looking at (4.47), it is seen that this represents the A_{mn} term in (4.46). Looking at Figure 32, it can be seen that this term represents the x -directed electric field source as observed by the x -directed electric field observer component within Region 3. The corresponding expanded EFIE equation from which (4.46) is extracted is (4.42). Note

that (4.42) is only the expansion of the x -directed EFIE and does not yet contain the test functions needed to complete the Galerkin's method (which show up as $e_{xm}(x, y)$ in (4.47)).

Closer inspection of (4.42) reveals that it contains the five expansion coefficients (a_n to e_n), each of length N , that form the unknown vector $[u]$ in (4.46). Before A_{mn} can be inserted into the MoM matrix (4.46), it is necessary to extract these coefficients from (4.41) to (4.45). Thus, when these elements (4.47) to (4.71) are multiplied by the expansion coefficients, the results are the homogeneous EFIEs of interest. Thus, A_{mn} will contain *only* the x -directed terms within Region 3 that are multiplied by a_n , B_{mn} by b_n , C_{mn} by c_n , D_{mn} by d_n , and E_{mn} by e_n .

Applying the Galerkin's Method will multiply all of these elements by the x -directed test function $e_{xm}(x, y)$ to represent their contribution and interaction with an x -directed observer within Region 3. By extracting only the terms associated with a_n in (4.42), multiplying these by the x -directed test function $e_{xm}(x, y)$, and integrating with respect to x and y , this results in the representation of A_{mn} given in (4.47). The summation notation in (4.42) is no longer needed in (4.47) since this will be taken into account when (4.47) is multiplied by the unknown vector $[u]$.

Note that A_{mn} also contains the total electric field, represented as the expansion coefficient a_n multiplied by the expansion function $e_{xm}(x, y)$. When the test function is applied to this term and integrated with respect to x and y , orthogonality of the basis functions is such that the resultant integral will only be non-zero when $n = m$.

For ease of reference, (4.42) and (4.47) are given here as first shown in Chapter 4.

$$\begin{aligned}
& \sum_{n=1}^N \int_{-\infty}^{\infty} \int_{-W/2}^{W/2} \left[(k^2 - \xi^2) \tilde{G}_{xx} d_n j_{xn} + j\xi \frac{\partial}{\partial y} \left(\tilde{G}_{yx} d_n j_{xn} + \tilde{G}_{yz} e_n j_{zn} \right) - \xi \zeta \tilde{G}_{zz} e_n j_{zn} \right] \frac{e^{j\xi(x-x')}}{2\pi j \omega \epsilon_1} dx' \\
& + \int_0^d \int_{-W/2}^{W/2} \frac{(\epsilon_3 - \epsilon_1)}{2\pi \epsilon_1} \left[(k^2 - \xi^2) \tilde{G}_{xx} a_n e_{xn} + j\xi \frac{\partial}{\partial y} \left(\tilde{G}_{yx} a_n e_{xn} + \tilde{G}_{yy} b_n e_{yn} + \tilde{G}_{yz} c_n e_{zn} \right) - \xi \zeta \tilde{G}_{zz} c_n e_{zn} \right] \\
& \cdot e^{j\xi(x-x')} dx' dy'] d\xi - \sum_{n=1}^N a_n e_{xn}(x, y, \zeta) = 0
\end{aligned} \tag{4.42}$$

$$\begin{aligned}
A_{mn} = & \int_{-\infty}^{\infty} \int_0^d \int_{-W/2}^{W/2} \frac{(\epsilon_3 - \epsilon_1)}{2\pi \epsilon_1} \left[(k^2 - \xi^2) \tilde{G}_{xx} + j\xi \frac{\partial}{\partial y} \tilde{G}_{yx} \right] e_{xn}(x', y') e_{xm}(x, y) e^{j\xi(x-x')} dx' dy' dx dy d\xi \\
& - \int_0^d \int_{-W/2}^{W/2} e_{xn}(x, y) e_{xm}(x, y) dx dy
\end{aligned} \tag{4.47}$$

C.3 Summary

This appendix explained how the elements (4.47) to (4.71) of the MoM matrix (4.46) are derived from (4.41) through (4.45) by walking through one such example. It was shown how (4.47) was extracted from (4.42) after the appropriate test function $e_{xm}(x, y)$ was applied and integrated with respect to x and y . The remaining 24 other elements of (4.46) can be found in similar fashion.

Appendix D

MATLAB CODE IMPLEMENTATION

D.1 Introduction

This appendix is aimed at explaining the basic set-up and implementation of the Matlab code used to implement the Newton's Method and solve for the eigenvalue ζ_z of the MoM matrix.

D.2 Overview

The main Matlab code (NewtonSinSin.m) is set up in two steps: variable set-up and Newton's Method. Within the Newton's Method, it starts off with an initial guess ζ_{guess} for the eigenvalue ζ_z (helpful to use a priori knowledge to aid in convergence of the root search); computes the pole, branch point, and branch cut location based off of this ζ_z value; and then calls the integration subroutine (NumIntSinSin.m) for the ζ_{guess} and a ζ_{delta} (slightly different than the ζ_{guess} value and necessary for the Newton's Method).

Under the integration subroutine, the Matlab code sets up the empty MoM matrix using the number of n_x and n_y (expansion) and m_x and m_y (test) basis functions that are being used to represent the volume in Region 3 and n_s (expansion) and m_s (test) basis functions for the surface contribution. A vector containing all of variables that will be passed to the Green's functions as they are integrated is then established. The MoM matrix is then filled using several iterative loops that address the volume-volume,

volume-surface, surface-volume, or surface-surface regions of interest. Within each of these loops, each Green's function (A_{mn} , B_{mn} , C_{mn} , etc.) is numerically integrated along the integration path of interest using the *quadl* function within Matlab. The path starts off at $-Ulimit$, which has been determined far enough out to ensure convergence of each MoM matrix subelement at that point. The path then goes above and beyond the pole location by integration factors *fac* and *fac2*, respectively. Note that the integration path steps over the branch cut, where it now calls the Green's function .m files that take into account being on the lower Riemann sheet by setting p_2 negative. After the path crosses back over the second branch cut, the original Green's function components are again used to complete the numerical integration out to *Ulimit*.

The last part of the integration subroutine fills the full MoM matrix with these integration values from each subelement and uses the Matlab function *det* to find the determinant of the subsequent matrix. This value is what is passed back to the main Matlab code.

The main code then calls the integration subroutine again, this time to find the determinant using ζ_{delta} . The Newton's Method is then applied using these two determinant values to compute whether we are within the tolerance level (typically 1e-10). If not, a new ζ_{guess} value is computed and the process is repeated. If the tolerance level is met, then $\zeta_{guess} = \zeta_z$ (the propagation constant we are looking for).

Figure 64 shows a diagram of the code and how it is implemented.

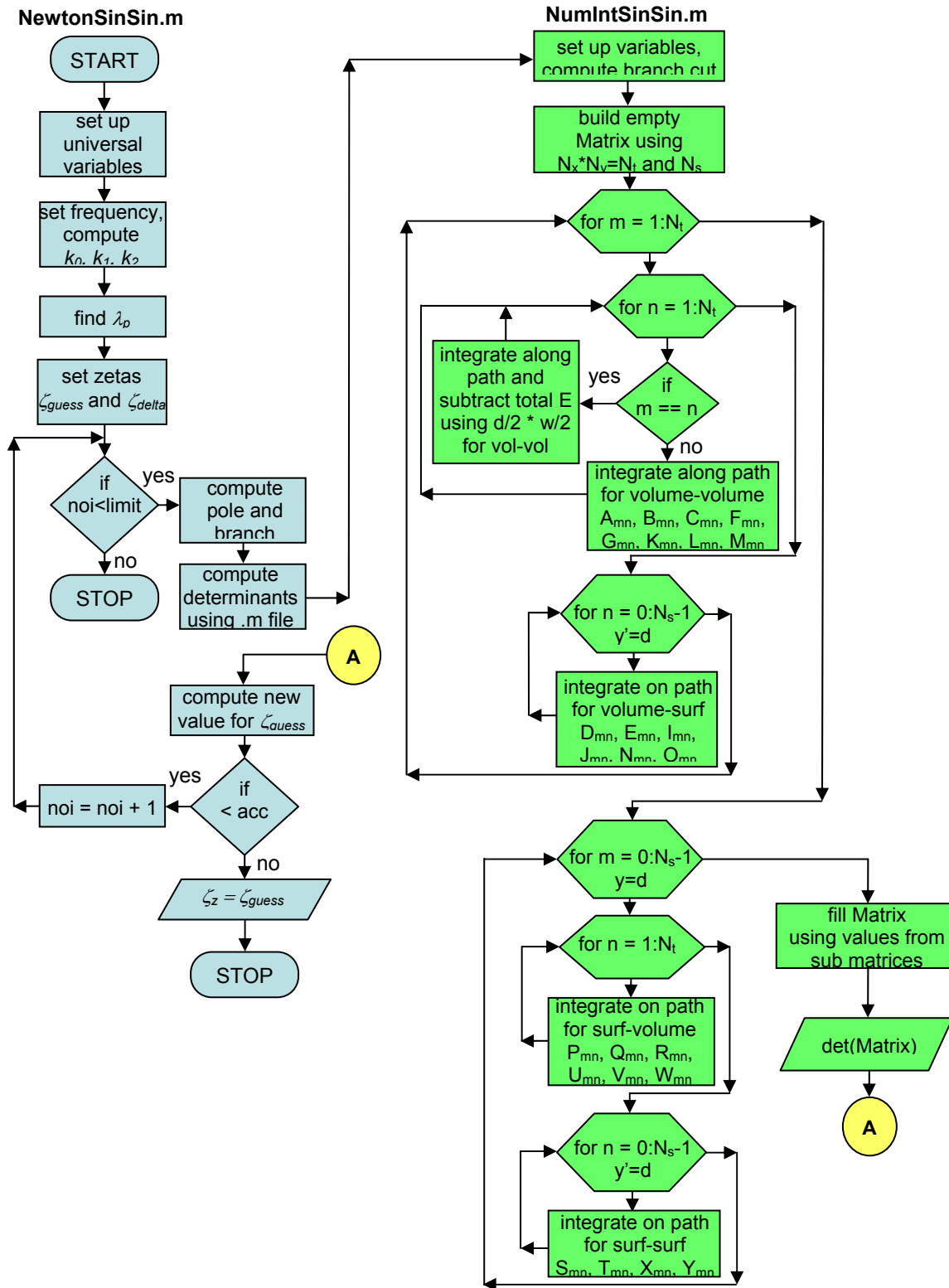


Figure 64: Matlab Method of Moments code implementation flowchart.

Bibliography

1. H. Ermert, "Guided modes and radiation characteristic of covered microstrip lines," *AEU*, pp. 65-70, 1976.
2. G. Kumar and K.P. Ray, *Broadband Microstrip Antennas*. Boston: Artech House, 2003.
3. W. Menzel, "A new traveling-wave antenna in microstrip," *AEU*, vol. 33, no. 4, pp. 137-140, 1979.
4. J. Radcliffe, G.A. Thiele, G.M. Zelinski, "A microstrip leaky wave antenna and its properties," *26th Antenna Measurement Techniques Association Symposium Proceedings*, St. Mountain, GA, Oct 2004.
5. G.M. Zelinski, "Finite difference time domain analysis of a leaky traveling wave microstrip antenna," Master's thesis, Air Force Institute of Technology, 2005.
6. W. Hong, T.L. Chen, C.-Y. Chang, J.-W. Sheen, and Y.-D. Lin, "Broadband tapered microstrip leaky-wave antenna," *IEEE Transactions on Antennas and Propagation*, vol. 51, no. 8, pp. 1922-1928, Aug 2003.
7. V. Nalbandian and C.S. Lee, "Bandwidth enhancement of microstrip antenna with leaky-wave excitation," *IEEE Antennas and Propagation Society International Symposium*, pp. 1224-1227, 1999.
8. C. Luxey and J.-M. Laheurte, "Effect of reactive loading in microstrip leaky wave antennas," *Electronics Letters*, vol. 36, no. 15, pp. 1259-1260, Jul 2000.
9. J.D. Kraus, *Electromagnetics*, New York: McGraw-Hill, 1991.
10. D.C. Chang and E.F. Kuester, "Total and partial reflection from the end of a parallel-plate waveguide with an extended dielectric slab," *Radio Science*, vol. 16, no. 1, pp. 1-13, Feb 1981.
11. A.F. Peterson, S.L. Ray, and R. Mittra, *Computational Methods for Electromagnetics*, Oxford: Oxford University Press, 1997.
12. M.J. Havrilla, "Analytical and experimental techniques for the electromagnetic characterization of materials," Ph.D. dissertation, Michigan State University, East Lansing MI, 2001.
13. J.S. Bagby, C.H. Lee, D.P. Nyquist, and Y. Yuan, "Identification of Propagation Regimes on Integrated Microstrip Transmission Lines," *IEEE Transactions on Microwave Theory and Techniques*, vol. 41, no. 11, pp. 1887-1894, Nov 1993.

14. D.P. Nyquist, J.M. Grimm, D.J. Infante, and H. Braunisch, "Classification of the Proper Propagation-Mode Spectrum and Leaky-Wave Modes on Open Planar Waveguides," *Electromagnetics*, pp. 105-130, 1997.
15. L.O. McMillan, N.V. Shuley, and P.W. Davis, "Leaky Fields on Microstrip," *Progress In Electromagnetics Research*, pp. 323-337, 1997.
16. D.P. Nyquist and D.J. Infante, "Discrete Higher-Order Leaky-Wave Modes and the Continuous Spectrum of Stripline," *IEICE Transactions*, vol. E78-C, no. 10, pp. 1331-1338, Oct 1995.
17. J.S. Bagby, C.H. Lee, Y. Yuan, and D.P. Nyquist, "Entire-domain basis MOM analysis of coupled microstrip transmission lines," *IEEE Transactions on Microwave Theory and Techniques*, vol. 40, issue 1, pp. 49-57, Jan 1992.
18. J.S. Bagby and D.P. Nyquist, "Dyadic Green's functions for integrated electronic and optical circuits," *IEEE Transactions on Microwave Theory and Techniques*, vol. MTT-35, no. 2, pp. 206-210, Feb 1987.
19. M.C. Bailey and M.D. Deshpande, "Integral equation formulation of microstrip antennas," *IEEE Transactions on Antennas and Propagation*, vol. AP-30, no. 4, pp. 651-656, Jul 1982.
20. J. Song, S. Ohnuki, D.P. Nyquist, K.M. Chen, and E.J. Rothwell, "Scattering of TE-polarized EM wave by discontinuity in grounded dielectric layer," *IEEE Transactions on Microwave Theory and Techniques*, vol. 42, no. 3, pp. 481-488, Mar 1994.
21. J.M. Grimm and D.P. Nyquist, "Spectral analysis considerations relevant to radiation and leaky modes of open-boundary microstrip transmission line," *IEEE Transactions on Microwave Theory and Techniques*, vol. 41, no. 1, pp. 150-153, Jan 1993.
22. Y. Yuan and D.P. Nyquist, "Full-wave perturbation theory based upon electric field integral equations for coupled microstrip transmission lines," *IEEE Transactions on Microwave Theory and Techniques*, vol. 38, no. 11, pp. 1576-1584, Nov 1990.
23. G.W. Hanson, A.B. Yakovlev, and J. Hao, "Leaky-wave analysis of transient fields due to sources in planarly layered media," *IEEE Transactions on Antennas and Propagation*, vol. 51, no. 2, pp. 146-158, Feb 2003.
24. F. Mesa, C.D. Nallo, and D.R. Jackson, "The theory of surface-wave and space-wave leaky-mode excitation on microstrip lines," *IEEE Transactions on Microwave Theory and Techniques*, vol. 47, no. 2, pp. 207-215, Feb 1999.

25. K.C. Chen, C.C. Tzuang, Y. Qian, and T. Itoh, "Leaky properties of microstrip above a perforated ground plane," *IEEE MTT-S International Microwave Symposium Digest*, vol. 1, pp. 69-72, Jun 1999.
26. A. Ip and D.R. Jackson, "Radiation from cylindrical leaky waves," *IEEE Transactions on Antennas and Propagation*, vol. 38, no. 4, pp. 482-488, Apr 1990.
27. D.R. Jackson and A.A. Oliner, "A leaky-wave analysis of the high-gain printed antenna configuration," *IEEE Transactions on Antennas and Propagation*, vol. 36, no. 7, pp. 905-910, Jul 1988.
28. Y. Li, H. Jiang, and Y. Long, "Analysis of microstrip leaky wave antenna with FDTD," *IEEE Antennas and Propagation Society International Symposium*, vol. 1A, pp. 271-274, Jul 2005.
29. M. Manteghi, A. Shooshtari, and S. Safavi-Naeini, "A leaky transmission line method for the analysis of the microstrip line traveling wave antennas," *IEEE Antennas and Propagation Society International Symposium*, vol. 2, pp. 1138-1141, Jul 1997.
30. K.S. Huang and C.C. Tzuang, "Characteristics and design of broadside-coupled transmission line at a higher order leaky mode," *IEEE Transactions on Microwave Theory and Techniques*, vol. 51, no. 2, pp. 440-447, Feb 2003.
31. G.W. Hanson and D.P. Nyquist, "Coupling of impressed radiation to resonant microstrip dipole currents deduced from a Hallen-type integral equation," *Antennas and Propagation Society International Symposium*, vol. 2, pp. 652-655, May 1990.
32. J.M. Grimm, D.P. Nyquist, M. Thorland, and D. Infante, "Broadband material characterization using microstrip/stripline field applicator," *Antennas and Propagation Society International Symposium*, vol. 2, pp. 1202-1205, Jul 1992.
33. G.W. Hanson and D.P. Nyquist, "Full-wave perturbation theory for the analysis of coupled microstrip resonant structures," *IEEE Transactions on Microwave Theory and Techniques*, vol. 40, no. 9, pp. 1774-1779, Sep 1992.
34. E. Semouchnikina, G. Semouchkin, W. Cao, and R. Mittra, "FDTD study of dispersion characteristics of leaky modes in microstrip leaky wave antennas," *IEEE Antennas and Propagation Society International Symposium*, vol. 1, pp. 486-489, Jun 2002.
35. W. Hong and Y.D. Lin, "Single-conductor strip leaky-wave antenna," *IEEE Transactions on Antennas and Propagation*, vol. 52, no. 7, pp. 1783-1789, Jul 2004.

36. D. Yau, N.V. Shuley, and L.O. McMillan, "Characteristics of microstrip leaky wave antenna using the method of moments," *IEE Proceedings – Microwaves, Antennas, and Propagation*, vol. 146, no. 5, pp. 324-328, Oct 1999.
37. G. Lovat, P. Burghignoli, F. Capolino, D.R. Jackson, and D.R. Wilton, "Analysis of directive radiation from a line source in a metamaterial slab with low permittivity," *IEEE Transactions on Antennas and Propagation*, vol. 54, no. 3, pp. 1017-1030, Mar 2006.
38. A. Polemi and M. Stefano, "On the polarization properties of a dielectric leaky wave antenna," *IEEE Antennas and Wireless Propagation Letters*, vol. 5, pp. 306-310, 2006.
39. J.R. Mosig, "Arbitrarily shaped microstrip structures and their analysis with a mixed potential integral equation," *IEEE Transactions on Microwave Theory and Techniques*, vol. 36, no. 2, pp. 314-323, Feb 1988.
40. E.F. Kuester, R.T. Johnk, and D.C. Chang, "The thin-substrate approximation for reflection from the end of a slab-loaded parallel-plate waveguide with application to microstrip patch antennas," *IEEE Transactions on Antennas and Propagation*, vol. AP-30, no. 5, pp. 910-917, Sep 1982.
41. K.A. Michalski and D. Zheng, "Rigorous analysis of open microstrip lines of arbitrary cross-section in bound and leaky regimes," *IEEE Microwave Symposium Digest*, vol. 2, pp. 787-790, Jun 1989.
42. A.A. Oliner, "Leakage from higher modes on microstrip line with application to antennas," *Radio Science*, vol. 22, no. 6, pp. 907-912, Nov 1987.
43. D.M. Pozar, "Input impedance and mutual coupling of rectangular microstrip antennas," *IEEE Transactions on Antennas and Propagation*, vol. AP-30, no. 6, pp. 1191-1196, Nov 1982.
44. W. Hong, G.Y. Chang, and Y.D. Lin, "Single-conductor strip higher order mode broadband leaky-wave antenna," *IEEE Antennas and Propagation Society International Symposium*, vol. 1, pp. 763-766, Jun 2004.
45. M.J. Freire, R. Marques, and F. Medina, "Full-wave analysis of the excitation of magnetostatic-surface waves by a semi-infinite microstrip transducer – theory and experiment," *IEEE Transactions on Microwave Theory and Techniques*, vol. 51, no. 3, pp. 903-907, Mar 2003.
46. T.L. Chen, Y.D. Lin, and J.W. Sheen, "Microstrip-fed microstrip second higher order leaky-mode antenna," *IEEE Transactions on Antennas and Propagation*, vol. 49, no. 6, pp. 855-857, Jun 2001.

47. J.L. Cina and L. Carin, "Mode conversion and leaky-wave excitation at open-end coupled-microstrip discontinuities," *IEEE Transactions on Microwave Theory and Techniques*, vol. 43, no. 9, pp. 2066-2072, Sep 1995.
48. C.L. Holloway and E.F. Kuester, "Net and partial inductance of a microstrip ground plane," *IEEE Transactions on Electromagnetic Compatibility*, vol. 40, no. 1, pp. 33-46, Feb 1998.
49. L. Carin and N.K. Das, "Leaky waves on broadside-coupled microstrip," *IEEE Transactions on Microwave Theory and Techniques*, vol. 40, no. 1, pp. 58-66, Jan 1992.
50. Y.L. Chow and W.C. Tang, "3-D Green's functions of microstrip separated into simpler terms – behavior, mutual interaction, and formulas of the terms," *IEEE Transactions on Microwave Theory and Techniques*, vol. 49, no. 8, pp. 1483-1491, Aug 2001.
51. S.D. Chen and C.C. Tzuang, "Characteristic impedance and propagation of the first higher order microstrip mode in frequency and time domain," *IEEE Transactions on Microwave Theory and Techniques*, vol. 50, no. 5, pp. 1370-1379, May 2002.
52. E.F. Kuester and D.C. Chang, "An appraisal of methods for computation of the dispersion characteristics of open microstrip," *IEEE Transactions on Microwave Theory and Techniques*, vol. MTT-27, no. 7, pp. 691-694, Jul 1979.
53. M.S. Viola and D.P. Nyquist, "An observation on the Sommerfeld-integral representation of the electric dyadic Green's function for layered media," *IEEE Transactions on Microwave Theory and Techniques*, vol. 36, no. 8, pp. 1289-1292, Aug 1988.
54. J.R. Mosig and A.A. Melcon, "Green's functions in lossy layered media: integration along the imaginary axis and asymptotic behavior," *IEEE Transactions on Antennas and Propagation*, vol. 51, no. 12, pp. 3200-3208, Dec 2003.
55. E.F. Kuester and D.C. Chang, "Theory of dispersion in microstrip of arbitrary width," *IEEE Transactions on Microwave Theory and Techniques*, vol. MTT-28, no. 3, pp. 259-265, Mar 1980.
56. E.F. Kuester and D.C. Chang, "Closed-form expressions for the current or charge distribution on parallel strips or microstrip," *IEEE Transactions on Microwave Theory and Techniques*, vol. MTT-28, no. 3, pp. 254-258, Mar 1980.

57. G.S. Wallinga, E.J. Rothwell, K.M. Chen, and D.P. Nyquist, "Efficient computation of the two-dimensional periodic Green's function," *IEEE Transactions on Antennas and Propagation*, vol. 47, no. 5, pp. 895-897, May 1999.
58. J.S. Zhao, W.C. Chew, C.C. Lu, E. Michielssen, and J. Song, "Thin-stratified medium fast-multipole algorithm for solving microstrip structures," *IEEE Transactions on Microwave Theory and Techniques*, vol. 46, no. 4, pp. 395-403, Apr 1998.
59. C.L. Holloway and E.F. Kuester, "Closed-form expressions for the current density on the ground plane of a microstrip line, with application to ground plane loss," *IEEE Transactions on Microwave Theory and Techniques*, vol. 43, no. 5, pp. 1204-1207, May 1995.
60. D.P. Nyquist and B. Kzadri, "Construction of dyadic Green's functions for the EM field in planar layered media using wave matrices for the electric Hertz potential," *European Microwave Conference Proceedings*, vol. 1, pp. 848-853, Sep 1991.
61. T.L. Chen and Y.D. Lin, "Aperture-coupled microstrip line leaky wave antenna with broadside mainbeam," *Electronics Letters*, vol. 34, no. 14, pp. 1366-1367, Jul 1998.
62. C.C. Chen and C.C. Tzuang, "Phase-shifterless beam-steering micro-slotted antenna," *Electronics Letters*, vol. 38, no. 8, pp. 354-355, Apr 2002.
63. P. Baccarelli, P. Burghignoli, F. Frezza, A. Galli, P. Lampariello, G. Lovat, and S. Paulotto, "Modal properties of surface and leaky waves propagating at arbitrary angles along a metal strip grating on a grounded slab," *IEEE Transactions on Antennas and Propagation*, vol. 53, no. 1, pp. 36-46, Jan 2005.
64. E. Semouchkina, W. Cao, R. Mittra, G. Semouchkin, N. Popenko, and I. Ivanchenko, "Numerical modeling and experimental study of a novel leaky wave antenna," *IEEE Antennas and Propagation Society International Symposium*, vol. 4, pp. 234-237, Jul 2001.
65. W.O. Coburn, "Radiation pattern of a leaky dual-ridged waveguide as a function of dielectric loading," *IEEE Antennas and Propagation Society International Symposium*, vol. 3B, pp. 67-70, Jul 2005.
66. J.I. Lee and Y.K. Cho, "Electromagnetic scattering by finite periodic strip grating on a grounded dielectric slab," *IEEE Antennas and Propagation Society International Symposium*, vol. 1, pp. 298-301, Jul 1997.
67. B.C.C. Chang, Y. Qian, and T. Itoh, "A reconfigurable leaky mode/patch antenna controlled by PIN diode switches," *IEEE Antennas and Propagation Society International Symposium*, vol. 4, pp. 2694-2697, Jul 1999.

68. K.C. Chen, Y. Qian, C.C. Tzuang, and T. Itoh, "A periodic microstrip radial antenna array with a conical beam," *IEEE Transactions on Antennas and Propagation*, vol. 51, no. 4, pp. 756-765, Apr 2003.
69. W. Hong, G.Y. Chang, and Y.D. Lin, "Annular ring microstrip leaky-wave antenna," *IEEE Antennas and Propagation Society International Symposium*, vol. 2B, pp. 234-237, Jul 2005.
70. E. Nishiyama, M. Aikawa, and S. Egashira, "Stacked microstrip antenna for wideband and high gain," *IEE Proceedings – Microwaves, Antennas, and Propagation*, vol. 151, no. 2, pp. 143-148, Apr 2004.
71. J. Radcliffe, G. Thiele, R. Penno, S. Schneider, and L. Kempel, "Microstrip leaky wave antenna performance on a curved surface," *IEEE Antennas and Propagation Society International Symposium*, pp. 4247-4250, 2006.
72. A. Neto, and N. Llombart, "Wideband localization of the dominant leaky wave poles in dielectric covered antennas," *IEEE Antennas and Wireless Propagation Letters*, vol. 5, pp. 549-551, 2006.
73. V. Nalbandian and C.S. Lee, "Tapered leaky-wave ultrawide-band microstrip antenna," *IEEE Antennas and Propagation Society International Symposium*, pp. 1236-1239, 1999.
74. H. Jiang, K.M. Pasala, L.M. Kempel, and S.M. Schneider, "A novel broadband microstrip leaky wave antenna with inhomogeneous substrate," *IEEE Antennas and Propagation Society International Symposium*, pp. 4243-4246, 2006.
75. E. Zhou and S. Xu, "Leaky characteristics of the first higher order mode in microstrip line with DNG/DPS substrates," *IEEE Antennas and Propagation Society International Symposium*, pp. 1181-1184, Jul 2006.
76. J. Zehentner, J. Machac, P. Lorenz, and J. Mrkvica, "Leaky wave radiation of a printed slotted antenna," *Asia-Pacific Microwave Conference*, vol. 3, pp. 1175-1178, Dec 2001.
77. Y.C. Chen, C.K. Wu, and C.C. Tzuang, "Dual-frequency electric-magnetic-electric microstrip leaky-mode antenna of a single fan beam," *IEEE Transactions on Microwave Theory and Techniques*, vol. 50, no. 12, pp. 2713-2718, Dec 2002.
78. J.L. Gomez-Tornero, A.T. Martinez, D.C. Rebenaque, M. Gugliemi, and A. Alvarez-Melcon, "Design of tapered leaky-wave antennas in hybrid waveguide planar technology for millimeter waveband applications," *IEEE Transactions on Antennas and Propagation*, vol. 53, no. 8, pp. 2563-2575, Aug 2005.

79. O. Losito, "A new design of broadband microstrip leaky-wave antenna," *23rd Annual Review of Progress in Applied Computational Electromagnetics*, pp. 1823-1827, Mar 2007.
80. C.N. Hu and C.C. Tzuang, "Microstrip leaky-mode antenna array", *IEEE Transactions on Antennas and Propagation*, vol. 45, no. 11, pp. 1698-1699, Nov 1997.
81. H. Rogier and D. DeZutter, "Berenger and leaky modes in microstrip substrates terminated by a perfectly matched layer," *IEEE Transactions on Microwave Theory and Techniques*, vol. 49, no. 4, pp. 712-715, Apr 2001.
82. E.L. Barsotti, E.F. Kuester, and J.M. Dunn, "A simple method to account for edge shape in the conductor loss in microstrip," *IEEE Transactions on Microwave Theory and Techniques*, vol. 39, no. 1, pp. 98-106, Jan 1991.
83. K.F. Fuh and C.C. Tzuang, "Magnetically scannable microstrip antenna employing a leaky gyromagnetic microstrip line," *Electronics Letters*, vol. 31, no. 16, pp. 1309-1310, Aug 1995.
84. D. Nghiem, J.T. Williams, D.R. Jackson, and A.A. Oliner, "Existence of a leaky dominant mode on microstrip line with an isotropic substrate: theory and measurements," *IEEE Transactions on Microwave Theory and Techniques*, vol. 44, no. 10, pp. 1710-1715, Oct 1996.
85. J.L. Gomez-Tornero, G. Goussetis, A.P. Feresidis, and A. Alvarez-Melcon, "Control of leaky-mode propagation and radiation properties in hybrid dielectric-waveguide printed-circuit technology: experimental results," *IEEE Transactions on Antennas and Propagation*, vol. 54, no. 11, pp. 3383-3389, Nov 2006.
86. T.M. Grzegorzcyk and J.R. Mosig, "Full-wave analysis of antennas containing horizontal and vertical metallizations embedded in planar multilayered media," *IEEE Transactions on Antennas and Propagation*, vol. 51, no. 11, pp. 3047-3054, Nov 2003.
87. R. Rodriguez-Berral, F. Mesa, and F. Medina, "Two-dimensional study of leaky modes in microstrip line with a semi-infinite layer," *Radio Science*, vol. 39, pp. 1-11, 2004.
88. P.W. Chen, C.S. Lee, and V. Nalbandian, "Planar double-layer leaky-wave microstrip antenna," *IEEE Transactions on Antennas and Propagation*, vol. 50, no. 6, pp. 832-835, Jun 2002.

89. F. Mesa, A.A. Oliner, D.R. Jackson, and M.J. Freire, "The influence of a top cover on the leakage from microstrip line," *IEEE Transactions on Microwave Theory and Techniques*, vol. 48, no. 12, pp. 2240-2248, Dec 2000.
90. T.S. Lind and M.F. Iskander, "On the coupling characteristics of coplanar waveguides and microstrip lines to multilayer dielectric media," *IEEE Transactions on Electromagnetic Compatibility*, vol. 34, no. 2, pp. 117-123, May 1992.
91. K.S. Lee, "Microstrip line leaky wave antenna," Ph.D. Dissertation, Polytechnic University of New York, 1986.
92. A. Taflov and S. Hagness, *Computational Electrodynamics: The Finite Difference Time Domain Method*, Boston: Artech House, 2000.
93. D.T. Prescott and N.V. Shuley, "Reflection analysis of the FDTD boundary condition – part II: Berringer's PML absorbing layers," *IEEE Transactions on Microwave Theory and Techniques*, vol. 45, no. 8, pp. 1171-1178, Aug 1997.

REPORT DOCUMENTATION PAGE				Form Approved OMB No. 074-0188	
<p>The public reporting burden for this collection of information is estimated to average 1 hour per response, including the time for reviewing instructions, searching existing data sources, gathering and maintaining the data needed, and completing and reviewing the collection of information. Send comments regarding this burden estimate or any other aspect of the collection of information, including suggestions for reducing this burden to Department of Defense, Washington Headquarters Services, Directorate for Information Operations and Reports (0704-0188), 1215 Jefferson Davis Highway, Suite 1204, Arlington, VA 22202-4302. Respondents should be aware that notwithstanding any other provision of law, no person shall be subject to a penalty for failing to comply with a collection of information if it does not display a currently valid OMB control number.</p> <p>PLEASE DO NOT RETURN YOUR FORM TO THE ABOVE ADDRESS.</p>					
1. REPORT DATE (DD-MM-YYYY) 19-06-2008		2. REPORT TYPE Doctoral Dissertation		3. DATES COVERED (From – To) Sep 2005 – May 2008	
4. TITLE AND SUBTITLE Material Perturbations to Enhance Performance of the Thiele Half-Width Leaky Mode Antenna				5a. CONTRACT NUMBER	
				5b. GRANT NUMBER	
				5c. PROGRAM ELEMENT NUMBER	
6. AUTHOR(S) Girard, Jason A., Major, USAF				5d. PROJECT NUMBER JON# 07-294	
				5e. TASK NUMBER	
				5f. WORK UNIT NUMBER	
7. PERFORMING ORGANIZATION NAMES(S) AND ADDRESS(S) Air Force Institute of Technology Graduate School of Engineering and Management (AFIT/EN) 2950 Hobson Way, Building 640 WPAFB OH 45433-8865				8. PERFORMING ORGANIZATION REPORT NUMBER AFIT/DEE/ENG/08-04	
9. SPONSORING/MONITORING AGENCY NAME(S) AND ADDRESS(ES) AFRL/RYDR DSN: 785-3802 x3475 2241 Avionics Circle WPAFB, OH 45433 POC: Bob Simpson, george.simpson@wpafb.af.mil				10. SPONSOR/MONITOR'S ACRONYM(S)	
				11. SPONSOR/MONITOR'S REPORT NUMBER(S)	
12. DISTRIBUTION/AVAILABILITY STATEMENT Approved For Public Release; Distribution Unlimited.					
13. SUPPLEMENTARY NOTES					
14. ABSTRACT Microstrip traveling-wave antennas, often referred to as leaky-wave antennas, have been shown to radiate when the dominant or fundamental mode is suppressed and the first higher-order mode is excited. One such microstrip variation is the Thiele Half-Width (THW) antenna, which operates from 5.9 - 8.2 GHz for this research. Increasing the bandwidth over which the THW antenna radiates is desired, as is a fundamental understanding of the propagation characteristics over this region. This dissertation seeks to vary or perturb the material and physical properties of the THW antenna, including strip-width variations and modifications of the substrate layer, to achieve these results.					
15. SUBJECT TERMS Leaky-wave; antennas; microstrip; traveling-wave; bandwidth.					
16. SECURITY CLASSIFICATION OF:			17. LIMITATION OF ABSTRACT UU	18. NUMBER OF PAGES 194	19a. NAME OF RESPONSIBLE PERSON Dr. Michael J. Havrilla (ENG)
a. REPORT U	b. ABSTRACT U	c. THIS PAGE U			19b. TELEPHONE NUMBER (Include area code) (937) 255-3636, ext 4582 (Michael.havrilla@afit.edu)

Standard Form 298 (Rev. 8-98)
Prescribed by ANSI Std. Z39-18